Probing the extreme planetary atmosphere of WASP-12b

Mark Swain, Jet Propulsion Laboratory, California Institute of Technology, 4800 Oak Grove Drive, Pasadena, CA 91109, USA

Pieter Deroo, Jet Propulsion Laboratory, California Institute of Technology, 4800 Oak Grove Drive, Pasadena, CA 91109, USA

Giovanna Tinetti, University College London, Department of Physics and Astronomy, Gower Street, London WC1E 6BT, UK

Morgan Hollis , University College London, Department of Physics and Astronomy, Gower Street, London WC1E 6BT, UK

Marcell Tessenyi, University College London, Department of Physics and Astronomy, Gower Street, London WC1E 6BT, UK

Michael Line, California Institute of Technology, Pasadena, CA 91106, USA

Hajime Kawahara, Department of Physics, Tokyo Metropolitan University, Hachioji, Tokyo 192-0397, Japan

Yuka Fujii, Department of Physics, The University of Tokyo, Tokyo 113-0033, Japan

Adam P. Showman, Department of Planetary Sciences and Lunar and Planetary Laboratory, The University of Arizona, 1629 University Blvd., Tucson, AZ 85721, USA

Sergey N. Yurchenko, University College London, Department of Physics and Astronomy, Gower Street, London WC1E 6BT, UK

Abstract

We report near-infrared measurements of the terminator region transmission spectrum and dayside emission spectrum of the exoplanet WASP-12b obtained using the HST WFC3 instrument. The disk-average dayside brightness temperature averages about 2900 K, peaking to 3200 K around 1.46 μm. Both the dayside and terminator region spectra can be explained in terms of opacity due to the metal hydrides CrH and TiH together with a dayside temperature inversion with a deep tropopause. Although our measurements do not constrain the C/O ratio, the combination of TiH and high temperatures could imply the atmosphere of WASP-12b may be significantly metal poor. The dayside flux distribution reconstructed from the ingress light-curve shape shows indications of a hotspot. If located along the equatorial plane, the possible hot spot is near the sub-stellar point, indicating the radiative time scale may be shorter than the advection time scale. We also find the near-infrared primary eclipse light curve is consistent with small amounts of prolate distortion. The likely picture of WASP-12b that emerges is that this gas giant is powerfully influenced by the parent star to the extent that the planet's dayside atmosphere is star-like in terms of temperature, opacity, and the relative importance of radiation over advection. As part of the calibration effort for these data, we conducted a detailed study of instrument systematics using 65 orbits of WFC3-IR grims observations. The instrument systematics are dominated by detector-related affects, which vary significantly depending on the detector readout mode. The 256×256 subarray observations of WASP-12 produced measurements within 15% of the photon-noise limit using a simple calibration approach. Residual systematics are estimated to be ≤70 parts per million.

1. Introduction

Among the more than 700 currently confirmed exoplanets, WASP-12b stands out as exceptional. This transiting gas giant, with a mass of 1.39 M_J and a radius of 1.83 R_J, orbits a 6300-K G star with a period of 1.09 days, resulting in an extraordinary level of insolation and, thus, extreme atmospheric heating (Hebb et al. 2009). Given the close proximity to the stellar primary, this system presents an opportunity to study a planetary atmosphere in a unique environment. The combination of the unusual nature of this system, the relatively bright stellar primary, and the system orientation, which provides both primary and secondary eclipse events, has made this target one of the more extensively observed exoplanet systems. Analysis of these observations has led to several noteworthy results that underscore the unique nature of this planet. For example, WASP-12b is inflated to an unusual degree that implies either significant internal heating or a large core mass (Ibgui et al. 2010). The atmosphere is likely extended, and the planet may be loosing substantial mass through Roche lobe overflow (Li et al. 2010); there is also evidence supporting the presence of a magnetospheric bow shock (Llama et al. 2011). The planet has been proposed to be carbon rich, with a C/O $\geq$1 (Madhusudhan et al. 2011a), a condition that may reduce TiO and VO abundances (Madhusadhan et al. 2011b). Recently, Spitzer measurements were reported that show a large-amplitude thermal phase curve with a significant phase offset at 3.6 μm (Cowan et al. 2012).

High-precision, near-infrared spectroscopy has the potential to provide additional constraints that complement the exiting measurements of WASP-12b. Previous near-infrared spectroscopic observations with Hubble Space Telescope (HST) have detected molecules such as H_2O, CO_2, CH_4, and CO in three hot-Jovian-type planets (Swain et al. 2008, 2009a, 2009b, Tinetti et al. 2010) and produced important constraints on the atmosphere of a hot-Neptune (Pont et al. 2009) and Super Earth (Berta et al. 2011). The need for near-infrared measurements of WASP-12b has been partially addressed with ground-based photometry (Croll et al. 2011, Zhao et al. 2012) and spectroscopy (Crossfield et al. 2012), although the fidelity of these observations was not sufficient to detect molecular features. Here we report high-precision, near-infrared spectroscopy measurements obtained with the HST.

2. Methods: Observations and Data Calibration

2.1 Observations

We observed the WASP-12b system using the WFC3 instrument with the G141 grism, which provides spectral coverage from 1.1 to 1.7 μm with a spectral resolution of R=300 at 1.38 μm. The observations reported here consist of two HST visits, each with five consecutive orbits, timed to measure a primary and secondary eclipse event (see **Figure 1**). For both events, the observations track the system light curve from pre-ingress to post-egress to provide a spectrophotometric baseline from which the eclipse depth can be measured. The primary eclipse, when the planet blocks some of the light from the stellar primary, probes the transmission spectrum of the planet's terminator region atmosphere. The secondary eclipse, when the planet passes behind the stellar primary, probes the emission spectrum of the planet's dayside atmosphere. For these observations, the primary and secondary eclipse measurements were timed to be separated by the minimum possible time feasible with HST with the objective of minimizing any effects

due to temporal changes in the exoplanet atmosphere or parent star. Detector-specific configuration information, such as integration time and subarray size, is contained in Table 1. Our choices for the detector readout mode maximized the instrument efficiency and avoided the WFC3 overheads that can reduce significantly the instrument efficiency when observing relatively bright objects, such as transiting exoplanet systems.

The near-infrared spectral signatures of transiting exoplanets, for both transmission and emission measurements, require precision measurements; consequently, the potential impact of instrument systematic errors must be considered. Past experience with exoplanet spectroscopy using HST/NICMOS showed that the instrument systematic effects were typically comparable to the absorption/emission features in the exoplanet spectrum. Under such conditions, even with careful analysis, details of the method used for removal of instrument systemic effects can impact the science measurement. An example of this was an analysis by Gibson et al. (2011) challenging the detection of methane originally reported by Swain et al. (2008). Subsequent analysis by Gibson et al. (2012) is consistent with the original 2008 result and indicates that consensus is emerging about the spectral shape (see **Figure 2**). This conclusion is reinforced by another independent analysis (Waldmann et al. 2012) that is also consistent with the original 2008 result. However, the measurement uncertainties remain a subject of contention because of different methods in how the underlying instrument state parameters are estimated; larger uncertainties in instrument state parameters generate larger uncertainties in the decorrelation results. Thus, the way an instrument model is constructed, in terms of both parameter values and the uncertainty in those values, can affect the final result. A purpose-built instrument, which would eliminate many of these problems, does not yet exist, and the field has to make the best of the instruments available. While healthy debate is beneficial for the field, these events underscore the need for careful investigation and a thorough understanding of instrument characteristics. This is best done by a systematic analysis of a large amount of data so that characteristic instrument behavior patterns can be identified. WFC3 is relatively new and an investigation of the instrument is especially timely.

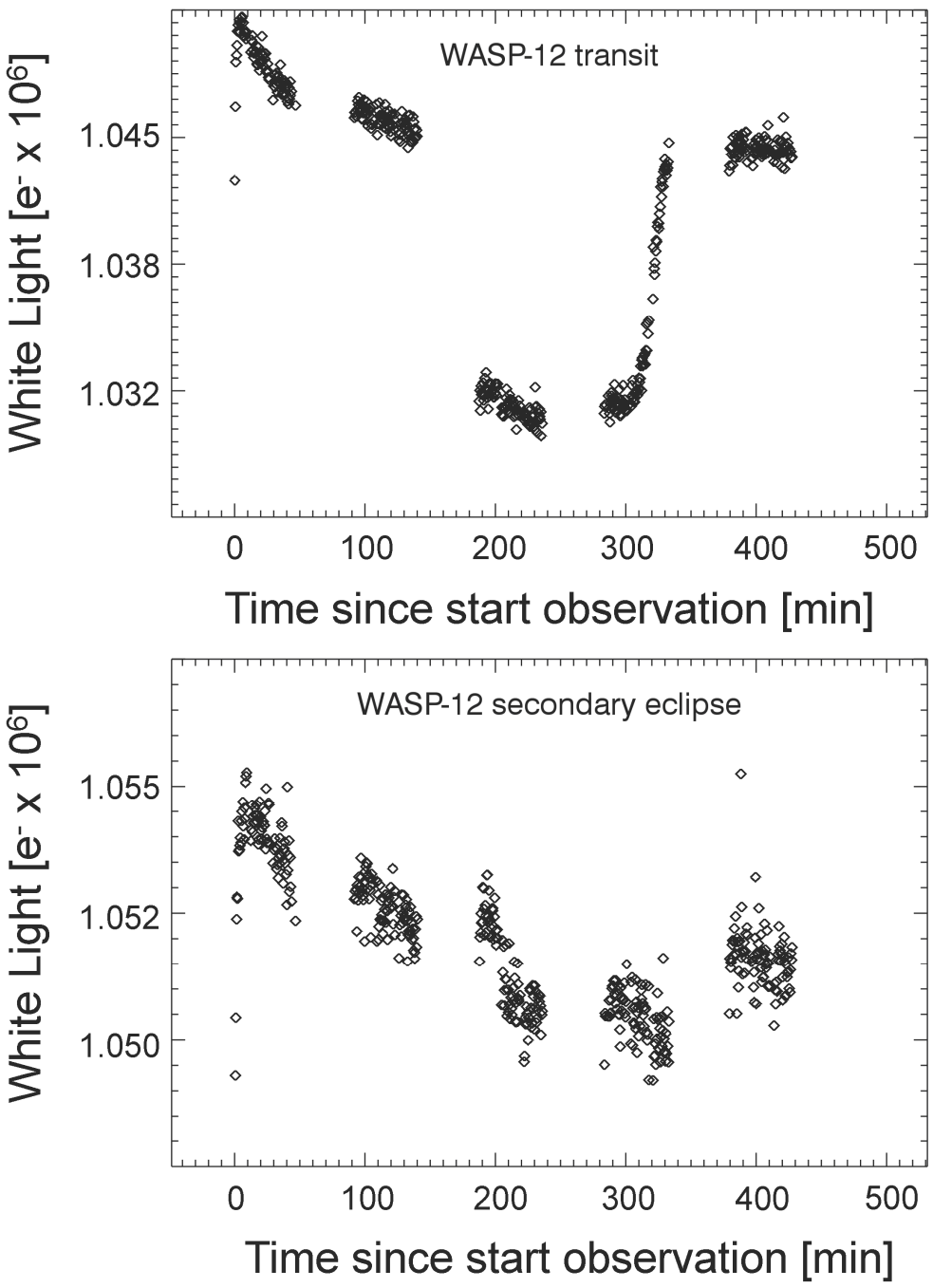

Figure 1: *The WFC3 observation of the WASP-12b primary eclipse (top) and secondary eclipse (bottom) showing the broad-band light curve, as a function of frame number on the x axis, based on data from the standard instrument pipeline. No data filtering or decorrelation has been applied. The dashed vertical lines show the boundaries due to earth occultations.*

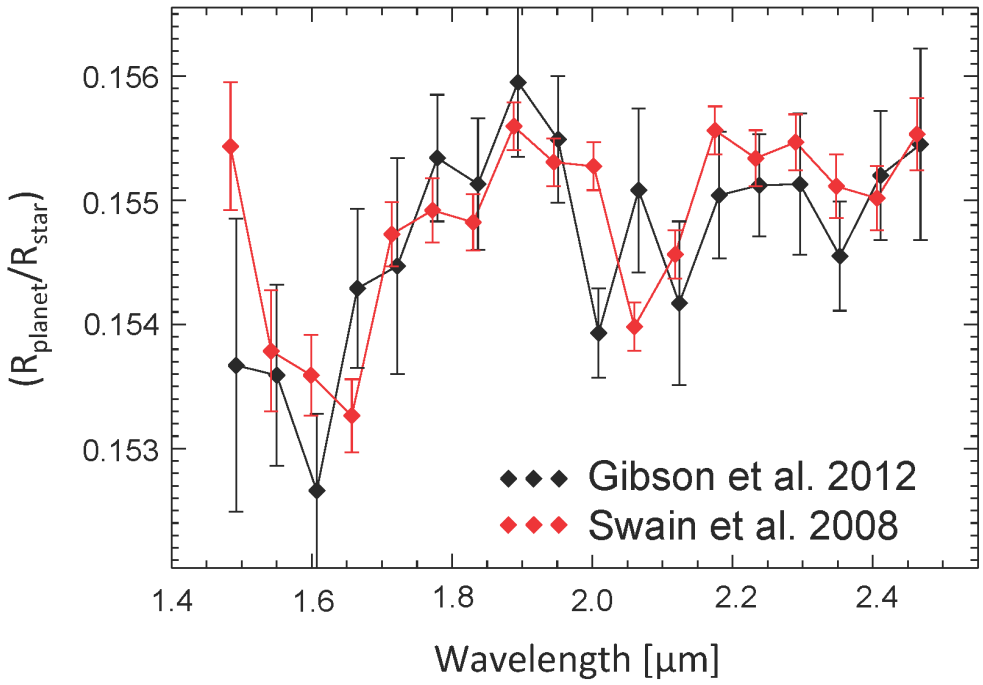

Figure 2: *Independent analysis showing the emerging consensus for the transmission spectrum of the hot-Jupiter HD 189733b. While there is now agreement about the spectral shape, which constitutes significant progress, differences in the uncertainty estimates are still being resolved.*

2.2 WFC3 Systematics

Here we report on a detailed investigation of WFC3 instrument systematic errors using a large amount of archival data. Readers primarily interested in the science results can skip to Section 2.3.

To characterize the instrument, we analyzed 65 orbits of archive data covering 10 objects. We probed the detector system by analysis of both the standard pipeline output and lower level data products (both "_raw" and "_ima" archive file types). We searched for a measurement dependence on the instrument optical state by constructing estimates for focus, spectrum position, and spectrum rotation. The spectral extraction and determination of optical state parameters was performed as described in Swain et al. 2009b. In contrast to NICMOS, in which optical state parameters such as focus and spectral position produced large instrument systematics, we find that the WFC3 instrument optical state changes, while measureable, produce negligible systematic changes in the measured spectroscopic flux density. In this regard, we confirm previous findings (Berta et al. 2011). We attribute this independence of the measured flux density on instrument optical state parameters as likely due to a high level of uniformity in the instrument focal plane array. Thus, small changes in the illumination function do not produce significant changes in the measured flux density. Another area where we see a marked improvement over NICMOS is that, with WFC3, there is no need for an additional "spacecraft settling" orbit at the beginning of the observations.

Analysis of the 65 orbits, using a consistent approach, reveals the way in which the WFC3 detector system responds to light changes with time in the 512×512 and 128×128

subarray modes; these changes can occur on intra-orbit, inter-orbit, or visit-to-visit time scales (see **Figures 3, 4**, and Supplementary Information for details). Importantly, these changes are only clearly detectable by analyzing the individual non-destructive reads as the detector is sampled up the ramp during an integration time. There are also significant, systematic changes in the average detector linearity relation due to over-exposure of the array (see **Figure 5**). If not correctly accounted for, these detector-system-related instrument systematics have the potential to compromise measurement of an exoplanet spectrum. The 256×256 subarray data we analyzed do not suffer from most of these problems, which implies the root cause may be connected to the array readout process and not to fundamental detector physics. However, until the root cause of changes in the detector response to light are understood, we caution that any exoplanet spectroscopy observations need to be analyzed at the level of individual non-destructive reads. Our findings summarizing the readout mode and type/extent of detector system systematic are summarized in **Table 1**.

Table 1: *The WFC3 IR-grism exoplanet spectroscopy program objects and data sets analyzed for systematic errors by our team. Significant changes in the way the detector responds to light exist for time scales ranging from seconds to days. This variation in the detector function depends on the readout mode. The severity of detector systematics as a function of time scale for each data set is coded with type-1, indicating nonexistent or minimal systematics, type-2, indicating potentially problematic systematics, type-3, indicating significant systematics that, if uncorrected, could bias estimates of the eclipse depth.*

WFC3 IR-grism data analyzed for instrument systematics										
Observational Parameters							Detector Systematics			
source	**yy-mm-dd**	**Orbits**	**H mag.**	**Spectral Type**	**ND reads**	**Subarray**	**ramp**	**Intra orbit**	**Inter orbit**	**Visit to visit**
WASP-12	11-04-11	5	10.23	G0	3	256	Type-1	Type-1	Type-1	Type-1
WASP-12	11-04-11	5	10.23	G0	3	256	Type-1l	Type-1	Type-1	Type-1
WASP-12	11-04-11	2	10.23	G0	3	256	Type-1	Type-1	Type-1	Type-1
HD 258439	11-04-11	2	9.11	A0V	9	256	Type-1	Type-1	Type-1	Type-1
HD 258439	11-04-11	2	9.11	A0V	9	256	Type-1	Type-1	Type-1	Type-1
HD 258439	11-04-11	2	9.11	A0V	9	256	Type-1	Type-1	Type-1	Type-1
COROT-2	10-10-18	4	10.44	G7V	4	128	Type-1	Type-1	Type-1	Type-3
WASP-4	10-11-25	5	10.84	G8	7	128	Type-1	Type-3	Type-3	Type-3
WASP-4	10-11-25	5	10.84	G8	7	128	Type-1	Type-1	Type-1	Type-3
GJ1214	10-10-08	4	9.09	M4	7	512	Type-2	Type-3	Type-2	Type-3
HAT-P-7	10-09-29	5	9.34	F	9	512	Type-2	Type-3	Type-3	Type-3
HAT-13	10-09-08	5	9.06	G4	9	512	Type-2	Type-3	Type-2	Type-3
TRES-2	10-10-09	4	9.92	GOV	15	512	Type-2	Type-2	Type-2	Type-3
TRES-4	10-11-23	5	10.35	F	16	512	Type-2	Type-2	Type-2	Type-3
HD 189733	10-11-10	5	5.6	K1	2	128	saturated			
HD 189733	10-09-04	5	5.6	K1	2	128				

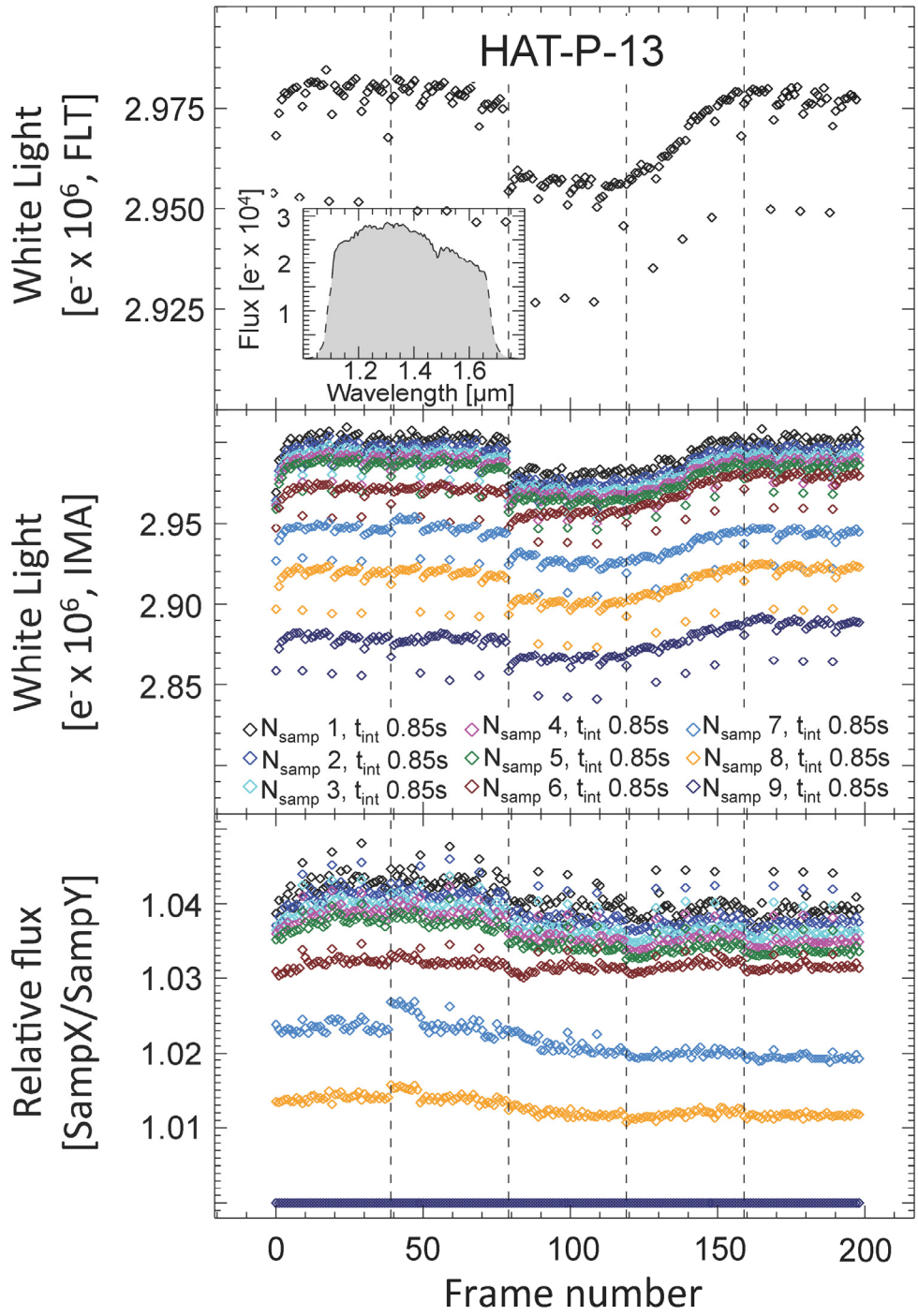

Figure 3: *An example of one of the standard diagnostics produced for each object in the 65 orbit data set used for assessing WFC3 systematics, with vertical dashed lines indicating a break between consecutive orbits. (Top) Broadband flux time series based on the standard pipeline data reduction. (Middle) Broadband flux time series based on individual non-destructive reads. The integration time for each non-destructive read is* T_{int} *in seconds. (Bottom) Normalized non-destructive read time series; these provide an easy way to visualize changes in detector functionality on all time scales.*

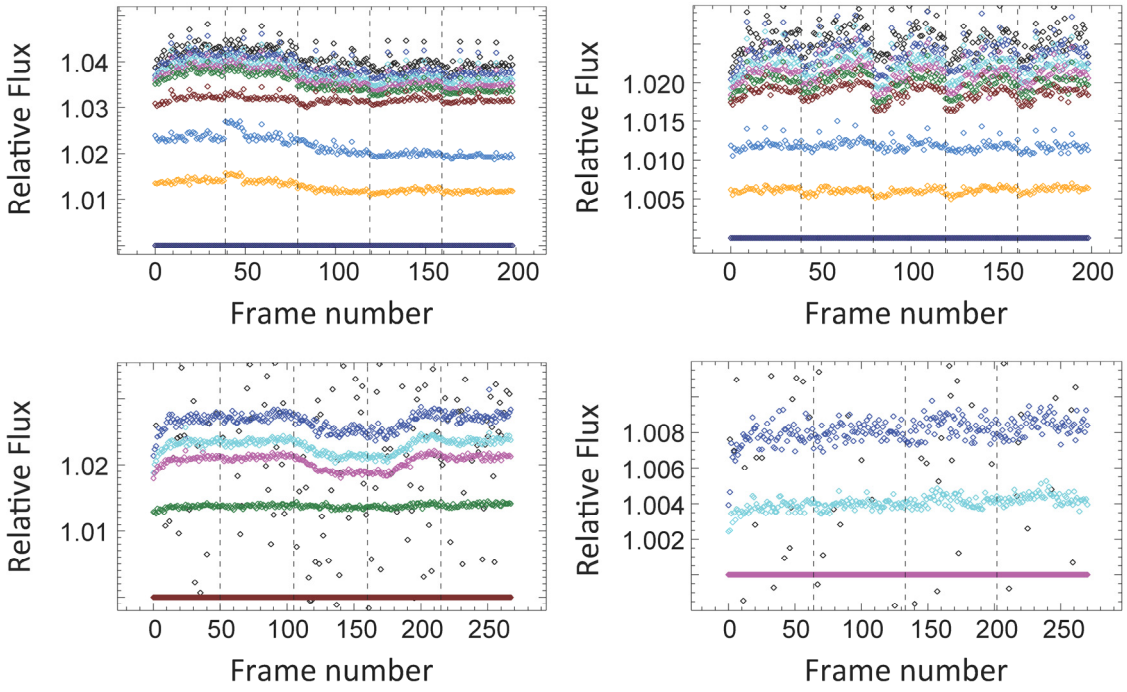

Figure 4: *Normalized Nsamp time series showing undesirable detector functionality changes (top and lower left) that could affect an exoplanet measurement. Each sample-up-the-ramp read is divided by the last read in the series. In the absence of detector-related systematics, the different time series should be constant. Instead, each of the above examples displays inter-orbit and/or intra-orbit systematics. The exoplanet systems in these examples (clockwise from top left) are HAT-P-13 (512×512 subarray), HAT-P-7 (512×512 subarray), Corot-1 (128×128 subarray), and WASP-4 (128×128 subarray).*

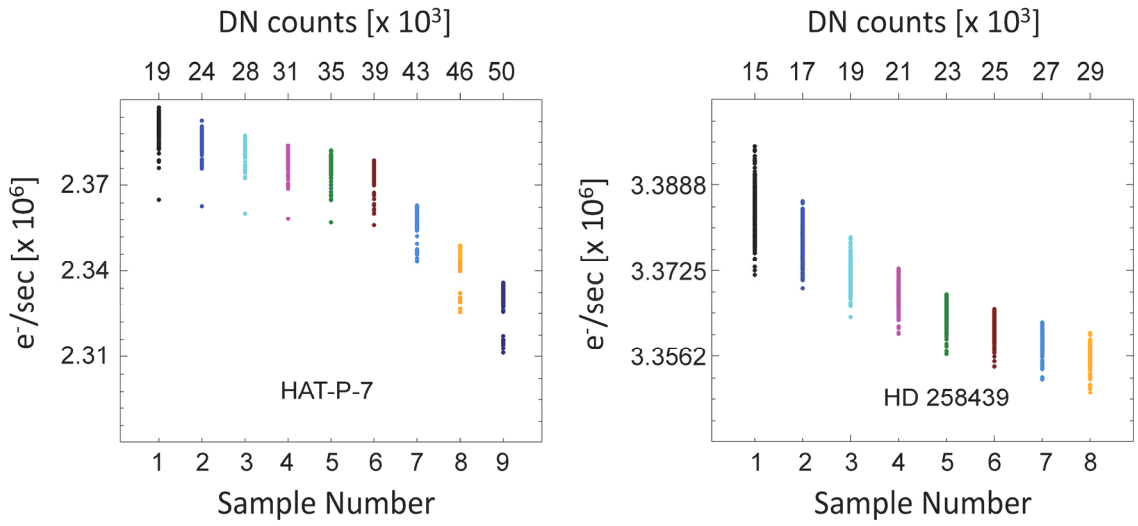

Figure 5: *The derivative of the detector linearity relation for two sources. We found a characteristic "knee" in this diagnostic when the detector well is filled beyond ~40,000 DN. A complete set of these figures is in the Supplementary information.*

In a recent analysis of WFC3-IR spectroscopy of the exoplanet GJ 1214b, observed in the 512×512 subarray mode, Berta et al. (2011) reported a "ramp" effect of increased flux measured in sequential integrations. Clarification is needed because the terminology in the literature is potentially confusing; the ramp in flux measured with sequential integrations reported by Berta et al. (2011) is undesirable and completely different from the ramp in flux measured by consecutive nondestructive reads occurring during an integration (frequently termed "sampling up the ramp"). We find that the extent of ramp effect seen by Berta et al. (2011) in the flux time series is strongly correlated to the length of time needed for a WFC3 buffer dump. The buffer dump operation lasts between 8 and 9 minutes in 512×512 subarray mode, about 3 minutes in 256×256 subarray mode, and 1 minute or less in 128×128 mode. In the case of the 128×128 and 256×256 subarray modes, the ramp effect is minimal and, in some cases, may not be present. In contrast, the 512×512 subarray mode ramp feature is larger and more persistent in that it establishes a trend that dominates the data for each block of measurements. During the camera buffer dump operation, the array is operated in a charge-flush mode. This charge flush mode interacts with the 512×512 subarray in a way that is qualitatively and quantitatively different from the 256×256 or 128×128 subarray modes. When Earth occultations prevent observing the source, the array is again operated in charge-flush mode. The effect of this is that there is a ramp present at the beginning of the measurements for each orbit. In the case of the 256×256 and 128×128 subarray modes, this ramp is very short, lasting only one or two samples; in the case of the 512×512 subarray modes, the ramp can continue until the next buffer dump and, for the 512×512 subarray, the effect of ~45 min. of charge flush array operation is similar to the effect of ~9 min of charge-flush operation.

For future observations of exoplanet systems with WFC3, we suggest the following guidelines.

1. Avoid the use of the 512×512 subarray mode.
2. Set the integration time so that the detector receives no more than ~40,000 DN before resetting.
3. Use a small number of samples up the ramp.
4. Work directly with the individual non-destructive read samples in the data reduction process.

Recommendation (1) avoids the intra/inter orbit variations in detector function that are seen in the 512×512 subarray mode, improves instrument overhead, and reduces the ramp effect. Recommendation (2) avoids the changes in detector function that can occur during an integration. Recommendation (3) maximizes the instrument throughput by delaying triggering a buffer dump due to the limit imposed by the file index counter. Recommendation number (4) provides a direct way to assess any changes in detector functionality.

2.3 Extracting the Spectra of WASP-12b

Due to operation in the 256×256 subarray mode, WASP-12 observations are of such high quality that a simple method can be used to determine the eclipse depth. In the case of both the primary and secondary eclipse, the eclipse depth in individual channels is estimated by a joint simultaneous fit to a model light curve and a linear trend in time that spans obits 2 to 5; the slope of the linear trend and the depth parameters are the free parameters adjusted by the fitting process. The primary eclipse light curve model was generated by a non-linear limb darkening model (Claret 2000) with a system ephemeris from (Maciejewski et al. 2011) and stellar parameters from Hebb et al. (2009). We find an offset of 4.7 ± 0.1 minutes with respect to the T_0 prediction (Maciejewski et al. 2011). The secondary eclipse light curve model was generated following Mandoll and Agol (2002). We estimated the eclipse depth uncertainty using (1) the uncertainty as estimated by the multi-parameter fitting process, (2) the MCMC method, (3) a prayer-bead style residual permutation analysis, (4) and the standard deviation in the mean of the residual time series and find all methods give results consistent results for these data. This simple inter-orbit detrending achieves about 160 ppm or ~1.15 times photon noise (see **Figure 6** and **Table 2**) and avoids the kinds of questions associated with complex decorrelation methods. The signal-to-noise of the final spectrum is increased by averaging together seven individual channels weighted by the uncertainties. Recently, WFC3-IR measurements of an exoplanet transmission spectrum have been reported by Berta et al. (2011) using an approach termed the OOT method to remove the large intra-orbit systematics found in 512×512 subarray data. As a consistency check, we applied the OOT method to our WASP-12 data and find virtually identical results.

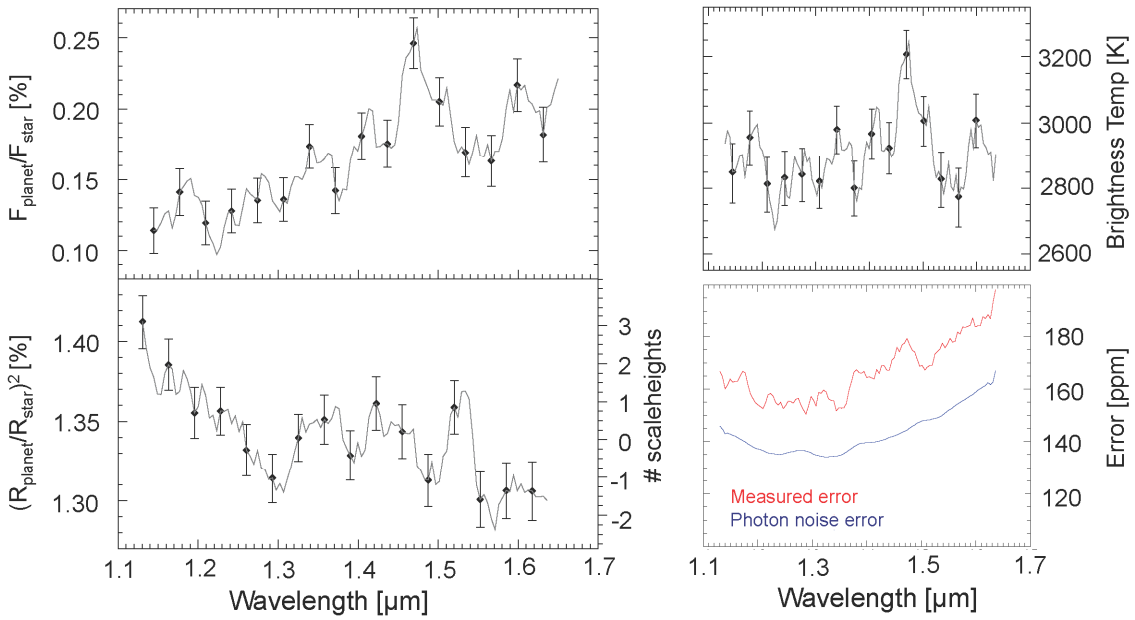

Figure 6: *(Left) Dayside region emission spectrum (top) and terminator region transmission spectrum (bottom). The data averaged in the spectral dimension and statistically independent measurements are shown as solid circles with plus/minus 1-σ errors. The grey line shows the spectrum value computed using a scrolling boxcar. (Right) The dayside emission spectrum in units of brightness temperature (top) and an uncertainty spectrum showing how each channel compares to the photon noise (bottom). These measurements approach the theoretical limit for what is achievable with WFC3 in the IR grism spectroscopy mode.*

For a measurement precision of ~160 ppm, corresponding to averaging 7 pixel-based spectral channels together in these observations, the 256×256 subarray mode delivers nearly ideal noise properties. However, if the entire passband is averaged together, the theoretical instrument precision becomes ~60 ppm for these measurements, which places a more demanding limit on instrument systematics. We explored this and two-instrument systematics that become detectable in the WASP-12b data when averaging the spectral passband. The first of these systematics is an intra-orbit, linear flux change that is easily detrended based on the out-of-eclipse data. The second of these systematics is a pattern in the data for each orbit associated with the third (and final) buffer dump; these data have a systematically lower flux value that becomes apparent when averaging the data together for the entire passband. Attempts to decorrelate using the optical state vectors did not work, but an OOT style of approach should prove effective. We did not pursue further correction of this particular systematic because it does not interact with the science related analysis for this paper. However, this investigation does show that even in the 256×256 subarray mode, there are WFC3 instrument systematics that lurk at the ~70 ppm level. Additional observations of both science targets and calibrator stars would benefit our understanding of the ultimate dynamic range capabilities of the instrument.

From the point of view of extracting a spectrum of WASP-12b with spectral resolution of $\Delta\lambda/\lambda = 42$, corresponding to averaging 7 pixel-based spectral channels, the measurement noise budget can be modeled as the root sum of squares of several components. Selecting 1.38 μm for the reference wavelength, we model the uncertainty

as 140 ppm due to photon shot noise, 15 ppm due to electronics noise, 69 ppm due to a systematic component that is wavelength independent, and 58 ppm due to a systematic that is wavelength dependent and affects the 1.38-1.48 μm channels (see **Figure 6**). This model is a worst case scenario and assumes the systematic errors have a covariance of zero; if this is not the case, the amplitude of the one or both of the systematic error terms is reduced to accommodate the covariance contribution. Given that (1) a calibration method based on a linear detrending of inter-orbit data results in a measurement error that is within 15% of the theoretical limit, (2) we wish to avoid the debate associated with more complex systematic error removal, and (3) our measurement uncertainties incorporate the affect of the small residual systematic errors, we proceed with the science analysis using the calibration based on the simple linear detrending of the inter-orbit data.

Table 2: *The transmission and emission spectrum data determined as described in Section 2.3. The values represent the average of seven pixel-based spectral channels; thus, every seventh wavelength is a statistically independent sample, and there are seven equally valid wavelength grids. Data for the wavelength grid we use for plotting the spectra in Figures 6 and 9 begins with 1.1306 μm and is every seventh row thereafter.*

Transmission Spectrum			Emission Spectrum		
λ [μm]	$(R_p/R_s)^2$ [%]	1-σ error [%]	λ [μm]	F_p/F_s [ppm]	1-σ error [ppm]
1.1306	1.412	0.017	1.1306	1276	166
1.1353	1.396	0.017	1.1353	1357	164
1.1399	1.384	0.016	1.1399	1330	160
1.1445	1.378	0.016	1.1445	1139	161
1.1492	1.367	0.016	1.1492	1146	163
1.1538	1.367	0.015	1.1538	1195	162
1.1584	1.380	0.016	1.1584	1258	162
1.1631	1.385	0.016	1.1631	1277	163
1.1677	1.383	0.016	1.1677	1156	165
1.1723	1.367	0.017	1.1723	1254	166
1.1770	1.369	0.017	1.1770	1410	166
1.1816	1.382	0.017	1.1816	1449	161
1.1863	1.377	0.017	1.1863	1488	158
1.1909	1.368	0.016	1.1909	1506	156
1.1955	1.355	0.016	1.1955	1386	154
1.2002	1.359	0.016	1.2002	1374	154
1.2048	1.373	0.016	1.2048	1321	153
1.2094	1.366	0.016	1.2094	1192	152
1.2141	1.352	0.015	1.2141	1102	154
1.2187	1.354	0.015	1.2187	1048	157
1.2233	1.344	0.015	1.2233	970	158
1.2280	1.356	0.015	1.2280	1022	157
1.2326	1.356	0.015	1.2326	1163	154
1.2373	1.358	0.015	1.2373	1261	153
1.2419	1.349	0.015	1.2419	1277	155
1.2465	1.354	0.016	1.2465	1177	152
1.2512	1.344	0.016	1.2512	1175	153
1.2558	1.350	0.016	1.2558	1301	155

Table 2: *(continued)*

Transmission Spectrum			Emission Spectrum		
λ [μm]	$(R_p/R_s)^2$ [%]	1-σ error [%]	λ [μm]	F_p/F_s [ppm]	1-σ error [ppm]
1.2604	1.332	0.016	1.2604	1434	155
1.2651	1.328	0.016	1.2651	1398	154
1.2697	1.323	0.016	1.2697	1376	156
1.2743	1.332	0.016	1.2743	1351	156
1.2790	1.321	0.015	1.2790	1540	153
1.2836	1.319	0.016	1.2836	1520	152
1.2883	1.313	0.016	1.2883	1477	150
1.2929	1.314	0.015	1.2929	1348	153
1.2975	1.307	0.015	1.2975	1312	157
1.3022	1.311	0.015	1.3022	1272	155
1.3068	1.305	0.015	1.3068	1359	153
1.3114	1.314	0.015	1.3114	1332	158
1.3161	1.321	0.015	1.3161	1448	158
1.3207	1.331	0.015	1.3207	1519	159
1.3253	1.340	0.015	1.3253	1518	158
1.3300	1.352	0.015	1.3300	1499	156
1.3346	1.343	0.015	1.3346	1557	155
1.3393	1.348	0.015	1.3393	1735	155
1.3439	1.349	0.015	1.3439	1731	151
1.3485	1.351	0.015	1.3485	1616	152
1.3532	1.346	0.016	1.3532	1622	152
1.3578	1.351	0.015	1.3578	1645	152
1.3624	1.349	0.015	1.3624	1688	154
1.3671	1.352	0.015	1.3671	1674	159
1.3717	1.359	0.015	1.3717	1421	162
1.3763	1.358	0.015	1.3763	1348	166
1.3810	1.338	0.016	1.3810	1432	167
1.3856	1.333	0.016	1.3856	1425	166
1.3903	1.328	0.016	1.3903	1636	166
1.3949	1.324	0.016	1.3949	1736	166
1.3995	1.337	0.016	1.3995	1704	164
1.4042	1.328	0.016	1.4042	1806	164
1.4088	1.332	0.016	1.4088	1888	164
1.4134	1.352	0.016	1.4134	2002	163
1.4181	1.360	0.017	1.4181	1985	167
1.4227	1.361	0.017	1.4227	1732	165
1.4273	1.354	0.017	1.4273	1736	169
1.4320	1.341	0.017	1.4320	1758	168
1.4366	1.342	0.017	1.4366	1754	167
1.4412	1.350	0.017	1.4412	1724	167
1.4459	1.347	0.017	1.4459	1748	170
1.4505	1.348	0.017	1.4505	1910	172

Table 2: *(continued)*

Transmission Spectrum			Emission Spectrum		
λ [μm]	$(R_p/R_s)^2$ [%]	1-σ error [%]	λ [μm]	F_p/F_s [ppm]	1-σ error [ppm]
1.4552	1.344	0.017	1.4552	2235	175
1.4598	1.342	0.017	1.4598	2358	174
1.4644	1.342	0.017	1.4644	2394	176
1.4691	1.345	0.017	1.4691	2458	177
1.4737	1.322	0.017	1.4737	2567	179
1.4783	1.319	0.017	1.4783	2270	176
1.4830	1.313	0.016	1.4830	2204	174
1.4876	1.313	0.016	1.4876	2138	174
1.4922	1.325	0.017	1.4922	2064	171
1.4969	1.310	0.017	1.4969	2064	168
1.5015	1.312	0.016	1.5015	2050	169
1.5062	1.328	0.016	1.5062	2026	167
1.5108	1.331	0.016	1.5108	2147	168
1.5154	1.354	0.017	1.5154	1956	168
1.5201	1.359	0.017	1.5201	1767	169
1.5247	1.353	0.017	1.5247	1692	173
1.5293	1.369	0.017	1.5293	1733	174
1.5340	1.369	0.017	1.5340	1693	175
1.5386	1.364	0.017	1.5386	1606	177
1.5432	1.341	0.017	1.5432	1696	175
1.5479	1.310	0.017	1.5479	1814	177
1.5525	1.301	0.017	1.5525	1672	179
1.5572	1.304	0.017	1.5572	1660	177
1.5618	1.299	0.017	1.5618	1749	178
1.5664	1.289	0.017	1.5664	1632	181
1.5711	1.282	0.017	1.5711	1702	180
1.5757	1.298	0.017	1.5757	1700	183
1.5803	1.302	0.017	1.5803	1793	183
1.5850	1.306	0.017	1.5850	2004	183
1.5896	1.305	0.018	1.5896	2134	184
1.5942	1.316	0.018	1.5942	1980	187
1.5989	1.306	0.018	1.5989	2166	183
1.6035	1.311	0.018	1.6035	2133	184
1.6082	1.305	0.018	1.6082	2165	184
1.6128	1.307	0.019	1.6128	2057	187
1.6174	1.306	0.018	1.6174	2034	186
1.6221	1.302	0.019	1.6221	1974	188
1.6267	1.302	0.018	1.6267	1988	186
1.6313	1.303	0.018	1.6313	1817	193
1.6360	1.300	0.019	1.6360	2011	198

Determining the depth of the primary and secondary eclipse, as a function of wavelength, provides different physical insights into the planetary atmosphere. For the primary eclipse, the depth is a measurement of $(R_p/R_s)^2$ where R_p is the radius of the planet and R_s is the radius of the parent star. For the secondary eclipse measurement, the depth is the ratio of $F_p/(F_s + F_p) \sim F_p/F_s$ where F_p is the flux density of the primary and F_s is the flux density of the parent star. In addition to working with these parameters, we find it useful to represent the primary eclipse (transmission) spectrum in units of scale height and the secondary eclipse (emission) spectrum in units of brightness temperature (**Figure 6**). To provide context, we compare WASP-12b to the only two other hot-Jupiter class planets with near-infrared emission spectra measured with HST (see **Figure 7** and **Table 3**).

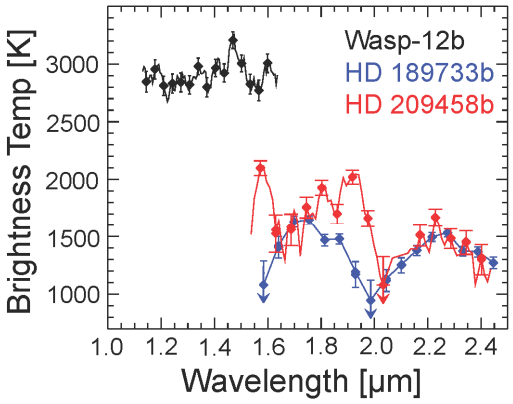

Table 3: *Assumptions for this calculation include Albedo = 0.00, Internal energy = 0.00, Molecular weight = 2, and perfect heat redistribution. Differences between the planet temperature estimate in this table and the measured brightness temperature are due to these assumptions.*

Parameter	WASP-12b	HD 209458b	HD 189733b
Planet Temperature	2628.20 K	1446.20 K	1182.83 K
Scale Height (Hs)	1128.68 km	591.97 km	249.25 km
1 Hs precision equivalent	238.24 ppm	182.24 ppm	141.17 ppm

Figure 7: *(Left) Brightness temperature spectra for the three hot-Jovians with emission spectra measured by HST. (Right) Placing WASP-12 in context.*

3. Atmospheric Modeling

We explored constraints provided by the spectral time series for the composition of the terminator region atmosphere, the composition and temperature structure of the dayside atmosphere, and the spatial distribution of dayside flux density. Interpreting exoplanet spectra via models is the norm in the field, and the approaches we used have been discussed in previous work. We modeled the transmission spectrum using an iterative forward model approach. The implementation has been described by Tinetti et al. (2007a) and subsequently refined in terms of linelists adopted (Tinetti et al. 2007, Tinetti et al. 2010). For modeling the dayside emission spectra, we used two approaches. The first approach was an adaption of the method of modeling the transmission spectrum, and the second was an optimal retrieval method previously described by Line et al. (2011).

For transiting exoplanets that experience a secondary eclipse event (when the planet appears to pass behind the stellar primary), the detailed shape of the ingress/egress light curve encodes information about the spatial distribution of the dayside flux. Under favorable conditions, an individual ingress (or egress) light curve shape can provide a one-dimensional constraint on the spatial distribution of emission (see **Figure 8**). The

technique has been used in our own solar system to determine the albedo distribution on Pluto (Young et al. 1999) and has recently been demonstrated for an exoplanet (Majeau et al. 2012; de Wit et al. 2012). For transiting exoplanets where the secondary eclipse impact parameter is an intermediate fraction of the stellar radius, the orientation of the occulting edge of the stellar disk changes orientation with respect to the planet; in these systems, measuring the combination of both the ingress and egress light curve segments provides a two-dimensional constraint for the dayside flux distribution of the exoplanet. For the inversion of a detailed light curve shape into a flux distribution, we used a tomographic method (Kawahara & Fuji 2010, 2011) employing Tikhonov regularization; essentially, this process selects the model that provides the best fit to the data. The constraint provided by the Tikhonov regularization helps establish the optimal spatial resolution supported by the data. Critical enabling aspects of this method are (1) adequate temporal resolution – achieved through measurement cadence, (2) good signal-to-noise (SNR) – achieved by observing bright targets, and (3) adequate control of instrument systematic errors – achieved through careful calibration.

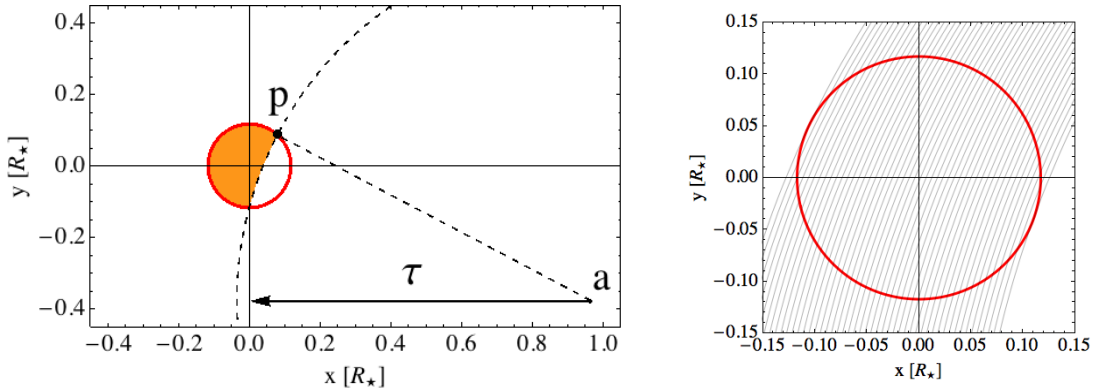

Figure 8: *(Left) Model geometry used to map the one-dimensional dayside emission distribution. The reconstruction process maps the flux density time series into a spatial distribution. (Right) Detail of the individual model "slices" that resolve the planet surface brightness distribution.*

4. Results

While the primary and secondary eclipse measurements probe separate atmospheric regions and were modeled individually, we were able to find a self-consistent description for atmospheric composition in the dayside and terminator regions. While this is satisfying, we stress that these results are indicational due to the limited spectral coverage of the observations and relatively low spectral resolution. Although longer wavelength measurements exist, they lack adequate spectral coverage and/or signal-to-noise to provide tight constraints. Also, there is always a risk in combining observations from different epochs and instruments; the astrophysical signal may change, and establishing the cross-calibration of different instruments can be a challenge. An improved understanding of the WASP-12b atmosphere requires spectroscopic observations over a larger range of wavelengths. We also note that inclusion of a model for the atmospheric response may be needed to connect the dayside and terminator regions conditions in a detailed way. Despite these limitations, our preliminary modeling is able to provide some

insight into the atmosphere of WASP-12b. What emerges is a picture of an exoplanet atmosphere that is like no other exoplanet characterized with infrared spectroscopy to date.

4.1 Terminator Region

The terminator region transmission spectrum of WASP-12b shows maximum opacity at short wavelengths, dropping to a local minimum at 1.3 μm. Additional opacity structure between 1.30 and 1.55 μm is adjacent to the region of minimal opacity between 1.56 and 1.64 μm. The opacity slope between 1.1 and 1.3 μm is especially noteworthy. This feature corresponds to about 3 atmospheric scale heights (see **Figure 6**). While the slope is suggestive of scattering due to dust or aerosols, the slope is too steep to explain in this manner alone. We find the spectrum can be modeled by a combination of the metal hydrides of titanium, TiH, and chromium, CrH, along with some H_2O (see **Figure 9**). We also find that models based on vanadium oxide, VO, and H_2O can partially explain the measured spectrum but fail to reproduce the local opacity peak at 1.53 μm. Our attempts to model spectral features based on TiO opacity were not successful.

4.2 Secondary Eclipse

What immediately stands out in the dayside emission spectrum of WASP-12b is the extremely high brightness temperature of this atmosphere. In the near-infrared, the typical brightness temperature is about 2900 K. The minimum brightness temperature is about 2700 K at 1.22 μm, and the maximum brightness temperature is 3200 K at 1.47 μm. The model proposed by Madhusudhan et al. (2011) does a good job of matching the slope of the dayside emission spectrum. We also confirmed this with our own models using CO_2/CO/CH_4/H_2O, and a combination of plausible temperature profiles, that it is possible to match the slope, but not the modulation, of the near-infrared spectra. However, we cannot provide a constraint on the C/O ratio for the near-infrared spectra. We also explored models based on VO and H_2O but were unable to find a good fit. However, a combination of chromium hydride, CrH, and titanium hydride, TiH, together with a temperature inversion provides a good fit to the near-infrared measurements (see **Figure 9** and **Table 4**). Including a temperature inversion corresponding to a tropopause at pressures of 10^{-1} to 10^{-2} bars improves the agreement between models and data in the 1.1- to 1.2-μm region. We find a mixing ratio for the metal hydrides in the range of 10^{-6} to 10^{-4}, with lower mixing ratios for H_2O.

Table 4: *A summary of the opacity sources used to model both the dayside emission and terminator region transmission spectra showing the comparison of the models with the data using the average reduced χ^2 for all seven statistically independent wavelength grids. Only the TiH/CrH opacity provides a self-consistent opacity source capable of providing a reasonably good model for both the dayside and terminator region spectra. This table is a companion to Figure 9 showing the model results for these cases.*

Opacity Sources Modeled	Dayside Emission Spectrum Modeled	Terminator Transmission Spectrum Modeled
CO/CH_4/H_2O C/O>1	2.9	3.8 (best model)
VO/H_2O	8.0	1.7
TiH/CrH/H_2O	1.4	1.5

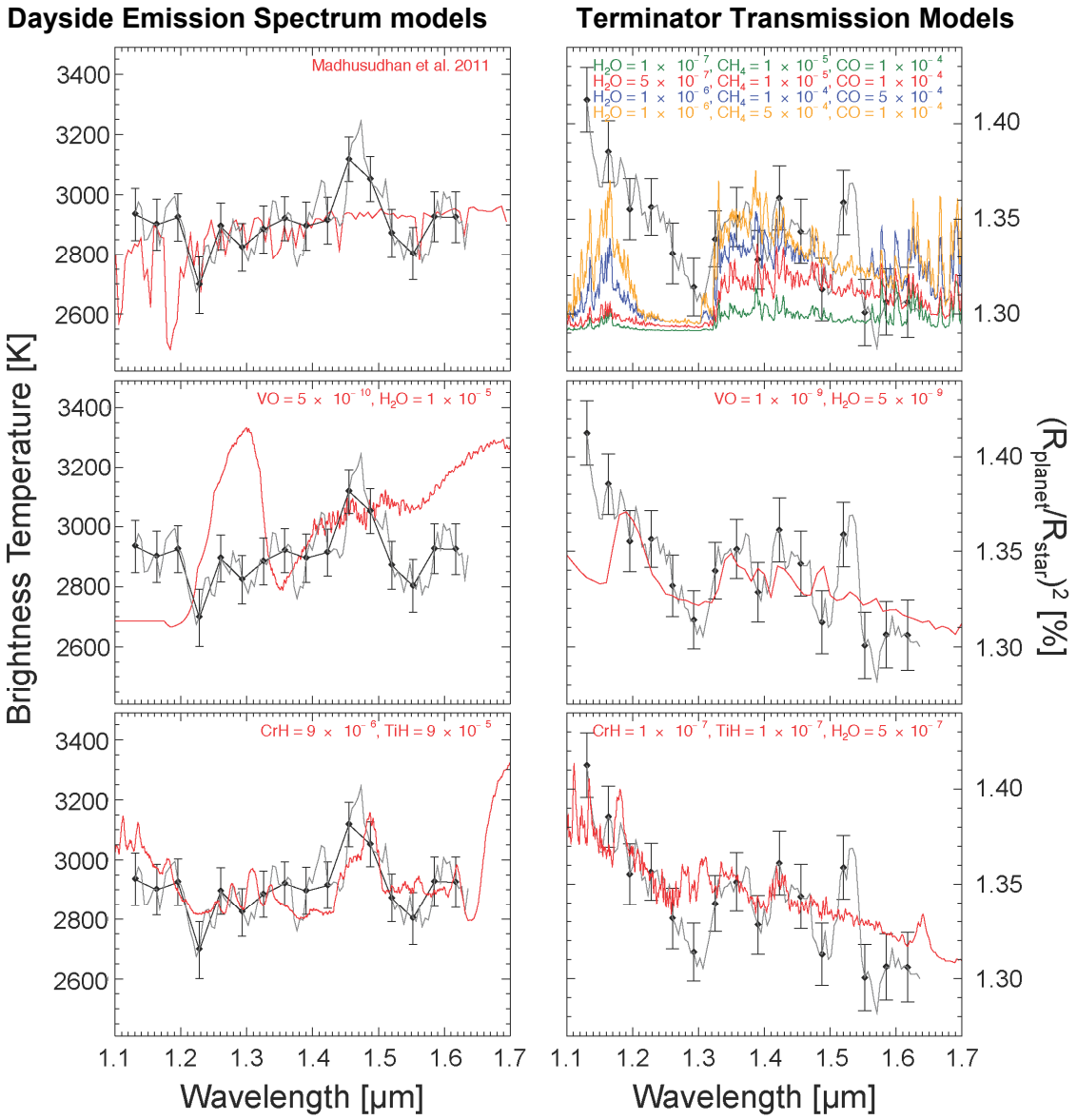

Figure 9: *Data and best fitting models for the dayside emission (left) and terminator region transmission (right). The spectra from both regions are explainable with an H_2 atmosphere containing trace amounts of TiH, CrH, and H_2O. The dayside pressure-temperature profile that provides the best fit to the data has a tropopause located around 10^{-2} bars with a temperature of ~2500 K.*

4.3 Spatial Constraints on Dayside Emission

Measuring the one-dimensional flux density distribution using the ingress event is possible with the secondary eclipse data set. Due to the temporal dependence of the light curve on the spatial flux density distribution, excellent control of instrument systematics is required. To increase signal-to-noise, the spatial flux distribution retrieval is performed

on the broadband 1.13-1.64 μm ingress light curve. As discussed in Section 2.3, a simple linear, inter-orbit detrending leaves two, orbit-based residual systematics identifiable in the broadband light curve. These are (1) an intra-orbit linear trend and (2) a lower flux measured in the third buffer dump. For purposes of flux reconstruction, we removed (1) with an intra-orbit linear detrending using the out-of-eclipse data to define the best fit slope and intercept values (see **Figure 10**). Since residual systematic (2) only affects data in the third buffer dump, and the ingress event is completed during the first two buffer dumps, no correction of residual systematic (2) is required and we proceeded with the estimate of the dayside flux spatial distribution.

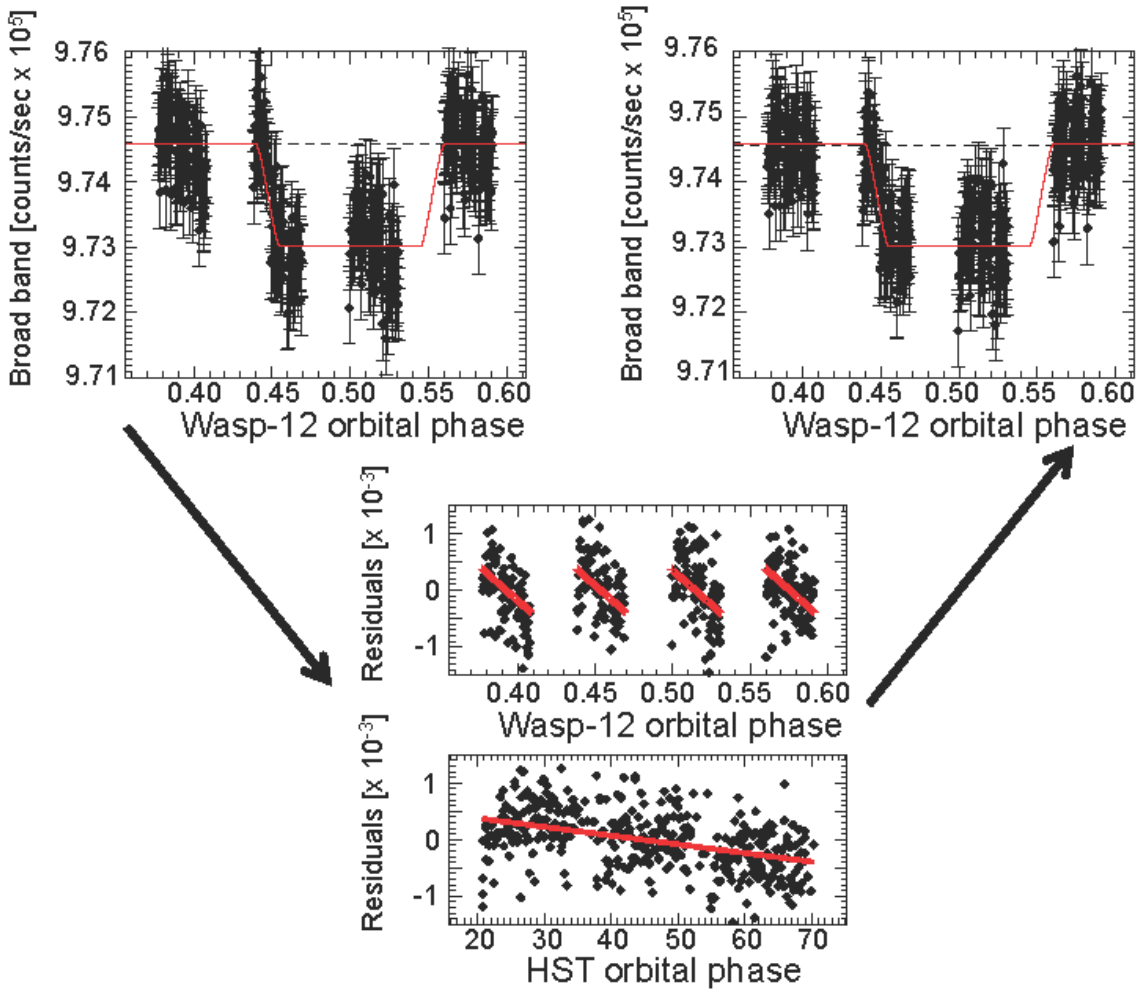

Figure 10. *Correction of a small residual systematic, which becomes detectable when the spectral data is average together to produce a broadband light curve. This systematic is removed through an intra-orbit linear detrending (a line of the same slope is removed from each orbit).*

Using the reconstruction method described in Section 3, we find an indication of non-uniform dayside emission localized in a broad central arc (see **Figure 11**). To test the significance of this result, we used a prayer-bead-type residual permutation analysis and find the surface brightness of the individual substeller slices in the central arc region have a 3-σ deviation from the brightness expected with uniform-disk model. The arc of enhanced emission has an east-west width of ~30 degrees and is ~10 percent brighter

than the surface brightness for a uniform-disk model. The arc also contains the sub stellar point, and it is possible the emission is localized to that region. While the 3-σ estimate of departures from a uniform disk model is encouraging, this indication of a bright region should be confirmed by additional observations, preferably timed to provide two-dimensional imaging and phased so that the instrument buffer dump does not occur in a critical portion of the ingress/egress light curve, as is presently the case. Given that we cannot definitively localize the emission further with the current observations, the implication for modeling the dayside emission spectrum is that a one-dimensional model is adequate for the analysis of these measurements.

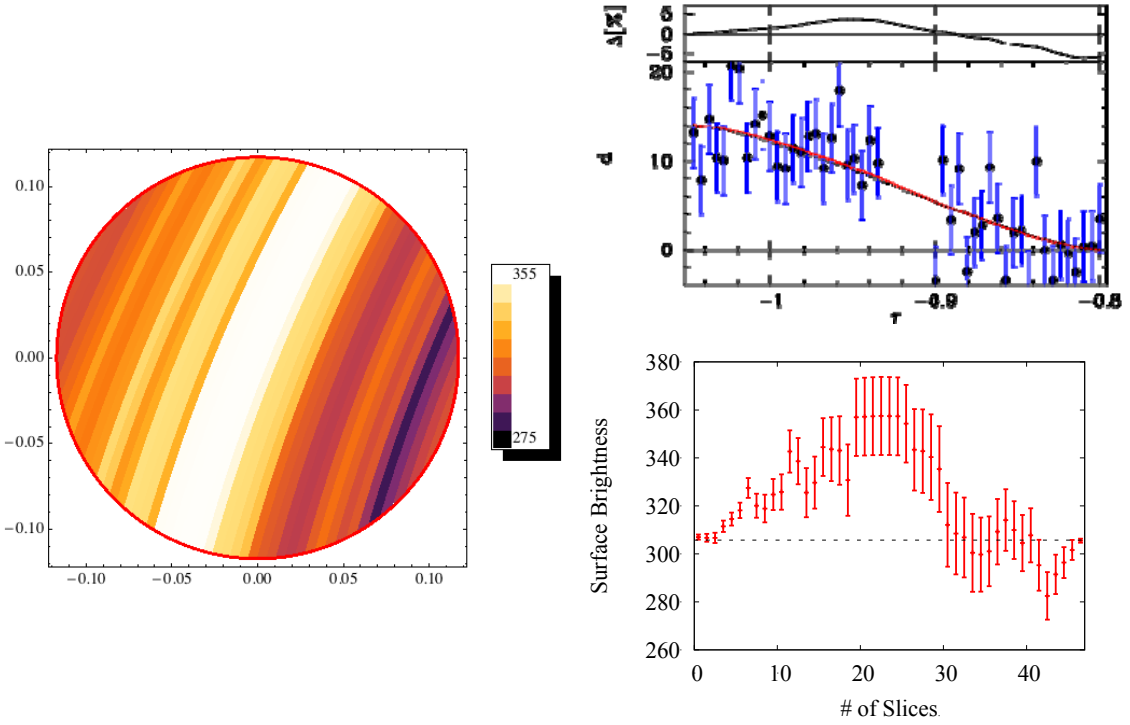

Figure 11: *Left – evidence for non-uniform emission potentially localized near the sub stellar point. Top right –detail of ingress data (blue) with uniform disk model (black) and best fit light curve (red). The upper panel shows deviation of the predicted curve from the uniform model (predicted/uniform - 1). Bottom right – the best fit model and the ± 1-σ uncertainty measured by the standard deviation of N-realizations based on prayer-bead type residual permutation, where N is the data number.*

Discussion:

This is the first time that high fidelity, space-based spectroscopy of a planet this hot has been obtained. The spectra of the terminator and dayside regions are separated by 28.4 hours and come as close to taking a spectral "snap-shot" of the planet's atmosphere as is observationally possible with HST. An advantage of temporally closely spaced observations is that they minimize the potential for stellar variations or climate variability

in the exoplanet. Although we treated these regions separately in our modeling effort, we were able to find a self-consistent physical picture where the main opacity sources between 1.3 and 1.6 μm are due to CrH, TiH, and H_2O (*H_2O is not needed in the dayside*) for both the terminator region transmission and dayside emission spectra. Our modeling suggests that the current observations probe pressure scales around one millibar at the terminator and between one bar and one millibar on the dayside. We find the slope of the dayside emission spectrum can be explained by models where the near-infrared opacity is due to carbon-based molecules $CO/CO_2/CH_4$ seen in other hot-Jovian atmospheres, and the slope in the dayside measurements agrees well with previous results (Madhusudhan et al. 2011a; see **Figure 9**). However, we find that neither the transmission spectrum, nor the detailed shape of the emission spectrum can be modeled using $CO/CO_2/CH_4$ opacity. The dayside brightness temperature of WASP-12b is sufficiently high that it is the same as the temperature of red dwarf stars of M4V to M5V class; when difficulties developed with modeling the transmission spectra of WASP-12b using the standard molecules, we explored incorporating metal hydrides seen in the atmospheres of cool stars. Only two other hot-Jovian type planets have had HST measurements of the near-infrared emission spectrum, and they have significantly lower near-IR brightness temperatures than WASP-12b (see **Figure 7**). Given the extreme nature of the WASP-12b atmosphere, perhaps it is not surprising that the standard exoplanet opacity sources do not provide a good fit to the data. We consider our models preliminary and they do not provide a complete view of the planet's atmosphere. The currently available data in the near-infrared and mid-infrared, are not sufficient to directly constrain the C/O ratio. Observations with improved spectral coverage, and higher spectral R and SNR, would likely provide the needed additional constraints to dramatically improve our ability to understand the WASP-12b atmosphere.

Our preference for attributing the dayside opacity to metal hydrides CrH and TiH is because this interpretation invokes a consistent opacity source for both dayside and terminator regions. Opacity due to TiO/VO has been proposed (Hubeny et al. 2003, Fortney et al. 2008) as a mechanism to produce temperature inversions in hot-Jovian type exoplanets. The identification of TiH rather than TiO is potentially significant and may imply an extremely low metallicity planetary atmosphere for WASP-12b. Theoretical work (Burrows et al. 2005; see Figure 3 therein) implies that the number fraction of TiH can exceed that of TO for temperatures above 2500 K if the solar metallicity is 0.01 × solar. A possible alternative explanation for finding TiH, and failing to find TiO, is that formation of TiO is suppressed due to a C/O ratio > 1 as proposed by Madhusudhan et al. (2011a). Additional work is needed to discriminate between the possible scenarios for TiO suppression in WASP-12b. Unfortunately, the use of TiO/TiH ratios as a potential metallicity diagnostic is limited to the very hot giant planets. Given the super solar metallicity of the parent star (Hebb et al. 2009), the indications of possible low atmospheric metallicity for WASP-12b need confirmation with additional observations.

The proposed prolate distortion of WASP-12b (Li et al. 2010) is, in principle, observable in the primary eclipse light curve. The presence of a prolate distortion causes the eclipse depth to be slightly deeper at the edges because the projected area of the planet is increased slightly for angular displacements away from the eclipse center. Using Spitzer primary eclipse measurements, Cown et al. (2012) found indications of a larger than predicted prolate distortion at measured 4.5 μm. Using our primary eclipse measurements, we searched for the degree of prolate distortion consistent with the data

(see **Figure 12**). Our measurements are consistent with the degree of the prolate distortion proposed by Li et al. (2010) and are inconsistent with the large values of prolate distortion found by Cowan et al. (2012). This difference with the Cowen et al. result could be due to probing different regions of the planetary atmosphere.

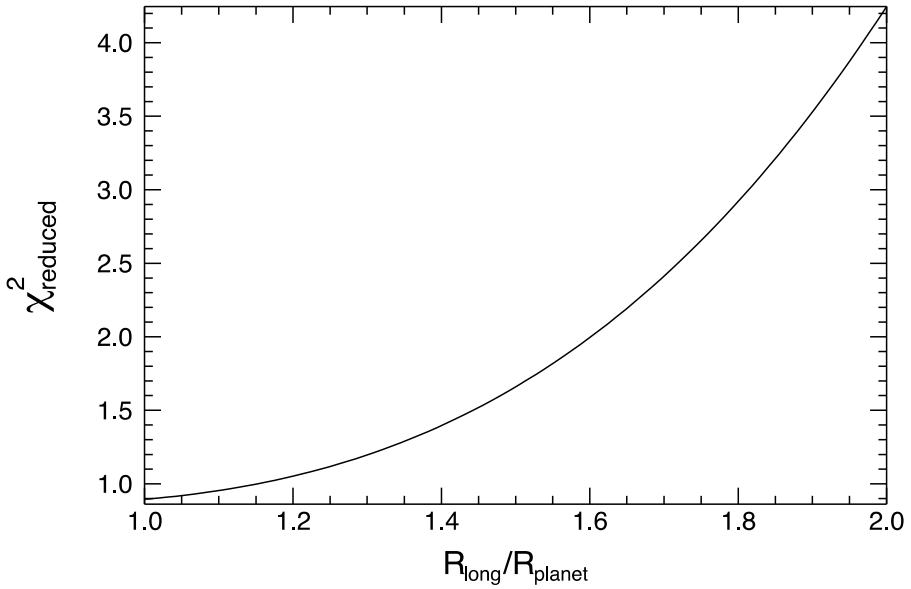

Figure 12: *Results of a χ^2 analysis of the degree of prolate distortion consistent with the WFC3 data. The data are consistent with either a small degree of prolate distortion (including zero) while large degrees of prolate distortion are inconsistent with our measurements. Here, the degree of prolate distortion is measured by the ratio of radii of the planet along the axis pointing to the star, R_{long}, and the radii of the planet perpendicular to the star, R_{planet}.*

The indication of possible brightening of the dayside disk in an arc-shaped region that includes the substellar point is interesting. If this candidate feature lies along the equatorial plane, it is located close to the sub stellar point. This is only a preliminary indication of a hot-spot-type feature, and it should be confirmed by additional observations phased for two-dimensional imaging. If the hot spot can be confirmed, the implications for modeling the dayside emission spectrum with a one-dimensional model will need to be examined. Ultimately, the question of size and location, and thus conditions and likely origin, of the hot spot requires two-dimensional spectral imaging, which is feasible with WFC3.

Although our inference of a hot spot near the substellar point remains tentative, it is interesting to consider the implications for the planet's atmosphere if this feature is real. Although hot-Jupiter-type planets like WASP-12b are probably synchronously rotating, atmospheric winds can in principle distort the temperature pattern and displace the hot spot from the substellar point. In particular, three-dimensional atmospheric circulation models of hot Jupiters typically exhibit a broad, eastward jet at the equator, which under some circumstances can cause an eastward displacement of the hottest regions from the substellar point (Showman & Guillot 2002; Cooper & Showman 2005; Showman et al. 2008, 2009; Menou & Rauscher 2009; Rauscher & Menou 2010, 2012; Perna et al. 2010; Dobbs-Dixon et al. 2010; Burrows et al. 2010; Thrastarson & Cho 2010; Heng et al. 2011a, 2011b). As has been discussed by previous authors, the offset of the hot spot

depends on a competition between the time for wind to advect air parcels from the dayside to the nightside, τ_{adv}, and the radiative time constant at the photosphere, τ_{rad} (e.g., Showman & Guillot 2002, Cooper & Showman 2005, Menou & Rauscher 2010, Heng et al. 2011a, Cowan & Agol 2011, Cowan et al. 2012). If the time scale for air parcels to relax into radiative equilibrium is shorter than the advection time ($\tau_{rad} << \tau_{adv}$), then the offset of the hot spot will be small; significant offset is expected only when $\tau_{rad} \sim \tau_{adv}$.

On WASP-12b, two main factors can conspire to ensure that $\tau_{rad} << \tau_{adv}$. First, hot atmospheres radiate more readily and have shorter radiative time constants than cooler atmospheres. Simple estimates suggest a scaling $\tau_{rad} \sim 1/T^3$ (Showman & Guillot 2002), where T is temperature; explicit computations of the temperature and pressure dependence of the radiative time constant under hot Jupiter conditions confirm a steep inverse temperature dependence at photospheric pressures (Showman et al. 2008). HD 189733b, where a hot spot offset has been observed (Knutson et al. 2007), is a relatively cool planet, and so thus may have a radiative time constant of $\sim 10^5$ sec at the photosphere, comparable to the day-night advection time in the presence of a multi-km sec^{-1} superrotating jet. However, because WASP-12b is ~2.5 times hotter, the above estimates suggest that the radiative time constant is shorter than plausible advection times at the photosphere.[1] This provides a natural explanation for our inferred lack of hot spot offset even if the wind speeds are fast (several km sec^{-1}). Consistent with these ideas, 3-dimensional circulation models including radiative transfer show that atmospheres receiving larger stellar flux tend to exhibit smaller hot spot offsets (Showman et al. 2009, Perna et al. 2012).

Second, recent work indicates that very hot Jupiters like WASP-12b may be subject to strong magnetic drag that limits the wind speeds (Perna et al. 2010; Menou 2012). At high temperatures, potassium, sodium, and other species partially ionize, leading to weak electrical conductivity that couples the atmospheric circulation to the planet's magnetic field. The resulting Lorenz forces can act to brake the zonal flows, with a characteristic drag time constant that, under plausible assumptions, decreases exponentially with increasing temperature (Perna et al. 2010). If the characteristic drag time constants are sufficiently short (perhaps less than a few x 10^5 sec), the friction will damp the superrotating equatorial jet, leading to longer day-night advection times (and smaller ratios of τ_{rad}/τ_{adv}) than would otherwise exist. Consistent with these ideas, three-dimensional hot-Jupiter circulation models including frictional drag explicitly show that, everything else being equal, stronger drag leads to smaller hot spot offsets (Rauscher and Menou 2012). Perna et al. (2010) and Menou (2012) suggest that, for hot Jupiters, this effect becomes important for planets hotter than ~1500 K, a breakpoint easily surpassed by WASP-12b.

[1] One could wonder if, in the absence of frictional drag in the upper atmosphere, not only the radiative time but also the advection time would be shorter on hotter planets than cooler planets, leaving the temperature dependence of the *ratio* τ_{rad}/τ_{adv} ambiguous. While hotter planets may indeed have faster wind speeds than cooler planets when drag near the photosphere is minimal, the effect is weak relative to the temperature dependence of τ_{rad} (Showman & Polvani 2011, Perna et al. 2012). This implies that τ_{rad}/τ_{adv} should indeed decrease with increasing temperature.

5. Conclusions

We present WFC3-IR grism spectroscopy measurements of the dayside and terminator regions of WASP-12b. Our measurements show this is the hottest exoplanet thus characterized to date with a brightness temperature maximum of 3200 K. We find that atmospheric models incorporating the metal hydrides CrH and TiH + possibly H_2O can explain both the transmission and emission spectra, and we find evidence for a dayside temperature inversion. The combination of high temperature and detection of TiH indicates this may be a low metallicity planetary atmosphere although TiO formation could also be inhibited by a C/O ratio >1. We also find indications of a hot spot, possibly located near the sub stellar point. From the standpoint of temperature and opacity sources, the atmosphere of WASP-12b appears more star like than planet like, confirming that this planet is truly an extreme world. These results, together with previous observational and theoretical work, support the conclusion that hot-Jupiter-type exoplanets are not a uniform class of objects and that these worlds exhibit a diversity that we are only beginning to understand.

From an instrumental point of view, this paper this paper reports the first exoplanet emission spectrum measured with the WFC3 instrument. We also conducted a systematic analysis of 65 orbits of WFC3-IR grism spectroscopy observation to characterize instrument systematics. To our knowledge, the scope and detailed level of this instrument analysis is unique in the area of exoplanet spectroscopy. We find that instrument systematics originating in the detector system can vary from minor to potentially science-compromising, depending on the detector subarray mode. The standard pipeline masks these problems, and we strongly encourage other researchers to analyze WFC3-IR measurements at the individual non-destructive read (Nsamp) level. Notwithstanding the problems with some detector modes, the WFC3 instrument is an excellent tool for exoplanet spectroscopic characterization; when operated in the optimal detector readout mode, WFC3-IR grism spectroscopy delivers nearly photon-noise-limited measurements with a dynamic range of ~6000:1 that do not require complex decorrelation to correct systematic errors.

Acknowledgements:

The research described in this publication was carried out in part at the Jet Propulsion Laboratory, California Institute of Technology, under a contract with the National Aeronautics and Space Administration. Y.F. and H.K are supported by JSPS (Japan Society for the Promotion of Science) Fellowship for Research, DC:23-6070 and PD:22-5467, respectively. We thank Nikku Madhusudhan for kindly providing the data for a previously published theoretical model for comparison with these observations. We are grateful to Rachel Akeson and Thomas Green for useful discussions and suggestions on improving the manuscript.

References:

Berta, Zachory K., et al., 2012. The Flat Transmission Spectrum of the Super-Earth GJ1214b from Wide Field Camera 3 on the Hubble Space Telescope. Astroph. J. 747, 35B.

Burrows A., Ram, R.S., Bernath, P.,Sharp, C.M., Milsom, J.A., 2002. New CrH Opacities for the Study of L and Brown Dwarf Atmospheres. Astroph J. 577,986.

Burrows, A., Dulick, M., Bauschlicher, C. W., Jr., Bernath, P. F., Ram, R. S., Sharp., C. M., Milsom, J. A.,2005. Spectroscopic Constants, Abundances, and Opacities of the TiH Molecule. Astroph. J. 624, 988B.

Burrows, A., Rauscher, E., Spiegel, D. S., Menou, K.,2010. Photometric and Spectral Signatures of 3D Models of Transiting Giant Exoplanets. Astroph. J. 719, 341B.

Cooper, C. S., Showman, A. P., 2005. Dynamic meteorology at the photosphere of HD 209458b. Astroph. J. 629L, 45C.

Cowan, N. B., Agol, E., 2011. A Model for Thermal Phase Variations of Circular and Eccentric Exoplanets. Astroph. J. 726, 82C.

Cowan, N. B., et al., 2012. Thermal Phase Variations of WASP-12b: Defying Predictions. Astroph. J. 747,82C.

Croll, B., Lafreniere, D., Albert, L., Jayawardhana, R., Fortney, J., Murray, N., 2011. Near-infrared Thermal Emission from WASP-12b: Detections of the Secondary Eclipse in Ks, H, and J. Astroph. J. 141, 30C.

Crossfield, I. J. M., Knutson, H., Fortney, J., Showman, A. P., Cowan, N. B., Deming, D., 2012. Spitzer/MIPS 24 micron Observations of HD 209458b: 3 eclipses, 2.5 transits, and a Phase Curve Corrupted by Instrumental Sensitivity Variations. arXiv: 1202, 1562C.

De Wit, J., Gillon, M., Demory, B., Seager, S., 2012. Secondary eclipse scanning of HD189733b: The perspectives of mapping distant worlds. arXiv. 1202,3829D.

Dobbs-Dixon, I., Cumming, A., Lin, D. N. C., 2010. Radiative Hydrodynamical Simulations of HD209458b: Temporal Variability. Astroph. J. 710, 1395D.

Fortney, J.J., Lodders, K., Marley, M.S., Freedman, R.S., 2008. A Unified Theory for the Atmospheres of the Hot and Very Hot Jupiters: Two Classes of Irradiated Atmospheres. Astroph. J. 678, 1419F.

Fujii, Y., Kawahara, H.,2012. Mapping Earth-analogs from Photometric Variability: Spin-Orbit Tomography for Planets in Inclined Orbits. arXiv 1204.3504F

Gibson, N., et al., 2012. A Gaussian process framework for modeling instrumental systematics: application to transmission spectroscopy. MNRAS. 419.2683G.

Gibson, N., Pont, F., Aigrain, S., 2011. A new look at NICMOS transmission spectroscopy: No conclusive evidence for molecular features. MNRAS. 276, 478G.

Hebb, L., et al., 2009. WASP-12b: The Hottest Transiting Extra-solar Planet Yet Discovered. Astroph. J. 693, 1920H.

Heng, K., Frierson, D. M. W., Phillipps, P.J., 2011. Atmospheric circulation of tidally locked exoplanets: II. Dual-band radiative transfer and convective adjustment. MNRAS. 418, 2669.

Heng, K., Menou, K., Phillips, P.J., 2011. Atmospheric circulation of tidally locked exoplanets: a suite of benchmark tests for dynamical solvers. MNRAS. 413, 2380.

Hubeny, I., Burrows, A., Sudarsky, D., 2003. A Possible Bifurcation in Atmospheres of Strongly Irradiated Stars and Planets. Astroph. J. 594, 1011H.

Ibgui, L., Burrows, A., Spiegel, D., 2010. Tidal Heating Models for the Radii of the Inflated Transiting Giant Planets WASP-4b, WASP-6b, WASP-12b, WASP-15b, and TrES-4. Astroph. J. 713, 751I.

Kawahara, H., Fujii, Y., 2011. Mapping Clouds and Terrain of Earth-like Planets from Photometric Variability: Demonstration with Planets in Face-on Orbits. Astroph. J. 739L, 62K.

Kawahara, H., Fujii, Y.,2010. Global Mapping of Earth-like Exoplanets From Scattered Light Curves. Astroph. J. 720, 1333K.

Knutson, H. A., 2007. Extrasolar planets: Water on distant worlds. Natur. 448, 143K.

Knutson, H. A., et al., 2007. A map of the day-night contrast of the extrasolar planet HD 189733b. Natur. 447, 183K.

Li, S., Miller, N., Lin, D. N. C., Fortney, J., 2010. WASP-12b as a prolate, inflated, and disrupting planet from tidal dissipation. Natur. 463.1054L.

Line, M. R.,Vasisht, G., Chen, P., Angerhausen, D., Yung, Y. L., 2011. Thermochemical and Photochemical Kinetics in Cooler Hydrogen-dominated Extrasolar Planets: A Methane-poor GJ436b? Astroph. J. 738, 32L.

Llama, J., Wood, K., Jardine, M., Vidotto, A. A., Helling, C., Fossati, L., Haswell, C., 2011. The shocking transit of WASP-12b: modeling the observed early ingress in the near-ultraviolet. 2011MNRAS. 416L, 41L.

Madhusudhan, N., et al., 2011. A high C/O ratio and weak thermal inversion in the atmosphere of exoplanet WASP-12b. Natur. 469, 64M.

Madhusudhan, N., Mousis, O., Johnson, T., Lunine, J., 2011. Carbon-rich Giant Planets: Atmospheric Chemistry, Thermal Inversions, Spectra, and Formation Conditions. Astroph. J. 743, 191M.

Majeau, C., Agol, E., Cowan, N., 2012. A Two-dimensional Infrared Map of the Extrasolar Planet HD 189733b. Astroph. J. 747L, 20M.

Mandel, K., Agol, E., 2002. Analytic Light Curves for Planetary Transit Searches. Astroph. J. 580L, 171M.

Menou, K., 2012. Magnetic Scaling Laws for the Atmospheres of Hot Giant Exoplanets. Astroph. J. 745, 138M.

Menou, K., Rauscher, E., 2009. Atmospheric Circulation of Hot Jupiters: A Shallow Three-Dimensional Model. Astroph. J. 700, 887M.

Perna, R., Heng, K.,Pont, F.,2012. The Effects of Irradiation on Hot Jovian Atmospheres: Heat Redistribution and Energy Dissipation. Astroph. J. 751, 59P.

Perna, R., Menou, K., Rauscher, E., 2010. Magnetic Drag on Hot Jupiter Atmospheric Winds. Astroph. J. 719,1421P.

Pont, F., Gilliland, R. L., Knutson, H., Holman, M., Charbonneau, D., 2009. Transit infrared spectroscopy of the hot Neptune around GJ 436 with the Hubble Space Telescope. MNRAS 393, 6P.

Rauscher, E., Menou, K., 2010. Three-dimensional Modeling of Hot Jupiter Atmospheric Flows. Astroph. J. 714, 1334R.

Rauscher, E., Menou, K., 2012. A General Circulation Model for Gaseous Exoplanets with Double-gray Radiative Transfer. Astroph. J. 750, 96R.

Showman, A. P., Cooper, C. S., Fortney, J. J., Marley, M. S., 2008. Atmospheric Circulation of Hot Jupiters: Three-dimensional Circulation Models of HD 209458b and HD 189733b with Simplified Forcing. Astroph. J. 282, 559S.

Showman, A. P., Fortney, J., Lian, Y., Marley, M. S., Freedman, R. S., Knutson,H. A., Charbonneau, D., 2009. Atmospheric Circulation of Hot Jupiters: Coupled Radiative-Dynamical General Circulation Model Simulations of HD 189733b and HD 209458b. Astroph. J. 699, 564S.

Showman, A. P., Guillot, T., 2002. Atmospheric circulation and tides of "51 Pegasus b-like" planets. A&A. 385,166S.

Showman, A. P., Polvani, L. M., 2011. Equatorial Superrotation on Tidally Locked Exoplanets. Astroph. J. 738, 71S.

Swain, et al., 2009. Water, Methane, and Carbon Dioxide Present in the Dayside Spectrum of the Exoplanet HD 209458b. Astroph. J. 704,1616S.

Swain, M. R., Vasisht, G., Tinetti, G., 2008. The presence of methane in the atmosphere of an extrasolar planet. Natur. 452, 329S.

Swain, M. R., et al., 2009. Molecular Signatures in the Near-Infrared Dayside Spectrum of HD 189733b. Astroph. J. 609L,114S.

Thrastarson, H. T., Cho, J. Y-K., 2010. Effects of Initial Flow on Close-in Planet Atmospheric Circulation. Astroph. J. 716, 144T.

Tinetti, G., et al., 2007. Water Vapour in the atmosphere of a transiting extrasolar planet. Natur. 448, 169T.

Tinetti, G., et al., 2010. Probing the Terminator Region Atmosphere of the Hot-Jupiter XO-1b with Transmission Spectroscopy. Astroph. J. 712L, 139T.

Tinetti, G., Liang, M-C., Vidal-Madjar, A., Ehrenreich, D., Lecavelier des Etangs, A., Yung, Y. L., 2007. Infrared Transmission Spectra for Extrasolar Giant Planets. Astroph. J. 654, 99T.

Waldman, I., Tinetti, G., Deroo, P., 2012. Blind extraction of an exoplanetary spectrum: Independent component analysis applied to HD189733b. Astroph J., submitted for publication.

Young, E. F., Galdamez, K., Buie, M. W., Binzel, R. P.,Tholen, D. J., 1999. Mapping the Variegated Surface of Pluto. Astroph. J. 117, 1063Y.

Zhao, M., Monnier, J. D., Swain, M. R., Barman, T., Hinkley, S., 1012. Ground-based Detections of Thermal Emission from CoRoT-1b and WASP-12b. Astroph. J. 744, 122Z.

Supplementary Material for: Probing the extreme planetary atmosphere of WASP-12b

Introduction

The supplementary material provides background information to support analysis and conclusions described in the main paper. Section 1 describes the diagnostics we used for the instrument characterization and contains the full set of diagnostic figures. Section 2 deals with the dayside mapping techniques and the used methods for testing those results. No attempt is made to repeat information contained in the main paper.

1. Instrument Characterization

To characterize the WFC3 IR detector system and instrument systematics, we implemented a standard set of diagnostics designed to probe different aspects of the instrument stability. With the exception of one source, which was strongly saturated, the diagnostics were implemented in a standardized way to allow comparison of performance in different modes. A list of the sources and instrument configuration information for the 65 orbits we analyzed is given in the main paper in Table 1. In what follows, we present our findings for detector-system-related instrument "systematic errors", which can also be considered as changes in the instrument transfer function or the mapping between photons into digital numbers (DN).

1.1 WFC3 Detector Background

The detector for the WFC3 instrument is an Teledyne HgCdTe H1RG type detector (e.g., Beletic et al. 2010) and we refer the reader to the WFC3 instrument handbook for full details of the system. Here, we provide an elementary description of the device operation, highlighting those aspects that directly connect with our analysis of WFC3 data.

The WFC3 detector operates by accumulating photoelectrons produced when photons are absorbed in the photoconductor lattice. The accumulation of photoelectrons occurs in a capacitor associated with each pixel, or unit cell, in the focal plane array; measuring the voltage on the pixel capacitor is thus a measurement of the accumulated number of photoelectrons. The measurement of voltage is accompanied by an uncertainty, termed read noise, that can be reduced by averaging multiple nondestructive reads. Due to the finite capacity to store photoelectrons, the pixel capacitor is periodically discharged through a reset process. The reset process does not leave the capacitor at a precise reference value and so the state of charge on the capacitor, termed the pedestal, must be measured after a reset to properly interpret subsequent reads before the next reset.

For a given device implementation, that is the detector assembly and its associated readout electronics, there is a minimum time required for these operations. This translates into a maximum rate at which an individual pixel can be readout. For a large format array, reading every pixel on the array can take a sufficiently long time that pixels illuminated by a bright source will saturate, that is exceed the charge storage limit of the pixel capacitor. Saturation is highly undesirable because it compromises the photon flux measurement, and it can generate additional measurement artifacts. An approach used to

enable the measurement of bright sources is to define an operational subarray; this reduces the number of pixels that must be readout and thus enables individual pixels to be readout at a higher cadence.

A typical operational approach, which applies to all the data analyzed in this study, is the following sequence: reset, read, read, read… read, reset. The first read is typically termed the "zero read" and is used to establish the pedestal; all subsequent reads prior to the next reset are compared with the zero read. The last read in the sequence is termed the "destructive read" to indicate that it is followed by a reset. The remainder of the reads are termed "nondestructive reads". The spacing between reads may be tailored, with uniform and logarithmic spacing being two common approaches. Increasing the number of nondestructive reads reduces the read noise (up to a limit). Decreasing the number of reads increases the readout speed and allows measurement of brighter sources. The method of using multiple nondestructive reads to sample the accumulation of photoelectrons in a detector unit cell is termed "sample up the ramp" (SUTR; Fixen et al 2000; Offenberg et al. 2001) and these measurements must be combined to estimate flux.

In the case of WFC3, the key operational parameters for the detector system that are under the control of the user are the integration time, the number of nondestructive reads, how the reads are spaced, and the subarray size and location. In the WFC3 nomenclature, Nsamp=0 is the zero read, and Nsamp=1 is the first nondestructive read used for estimating astrophysical flux. The most compact read sequence supported by WFC3 is a [reset, Nsamp=0, Nsamp=1, Nsamp=2, reset] sequence. The data generated by WFC3 are represented in the MAST archive as several data products, each associated with a certain level of processing, as follows:

- _raw – integer format data with no corrections. We used this data for analog-to-digital conversion (ADC) performance testing and characterization.
- _ima – 16 bit float format data that has standard bias and flat field corrections applied. Individual Nsamp measurements are preserved.
- _flt – pipeline-corrected data where the Nsamp measurements have been combined and replaced with a single flux measurement with the cadence of the integration time. A linearity correction has also been performed. These data are in 16 bit float format.
- _drz – an additional level of processing designed for two dimensional imaging; this data product is not needed for spectral analysis.

During observations, the data from individual reads is stored in memory on the WFC3 instrument computer. When the instrument memory buffer is full, the data must be moved to the spacecraft computer memory. The process of moving the data from the instrument to spacecraft memory takes several minutes and is termed the "buffer dump". During this interval, the spacecraft is still pointed at the target and the detector system is still accumulating charge. To prevent saturation, the detector is automatically switched into a charge flush mode where every pixel is readout and reset and, in so doing, automatically defines the integration time as 3.2 seconds. This change in the detector operational state during the buffer dump has very important consequences for exoplanet spectroscopy, which, from the point of view of WFC3, is the measurement of bright point sources.

A typical sequence of WFC3 IR-grism exoplanet observations, as processed by the standard pipeline (_flt data), is dominated by three immediately visible characteristic

patterns – large gaps, small gaps, and a slope for each group of data (see Figure 1.1-1). The large gaps are caused by Earth occultations, while the small gaps are due to the buffer dump. The slope, sometimes termed "ramp", are a systematic change in the measured flux, from lower to higher, that occurs with subsequent reads in between buffer dump intervals. It is typical for the first flux measurement at the intra-buffer-dump interval to be much lower than subsequent measurements. The corresponding Nsamp data also show characteristic patterns, but the situation is slightly more complex; the long gaps and short gaps are still present, but the flux ramp effect is mixed with the intrinsic detector sample up the ramp sequence. Any departures of the detector from linear operation adds additional patterning in an Nsamp time series.

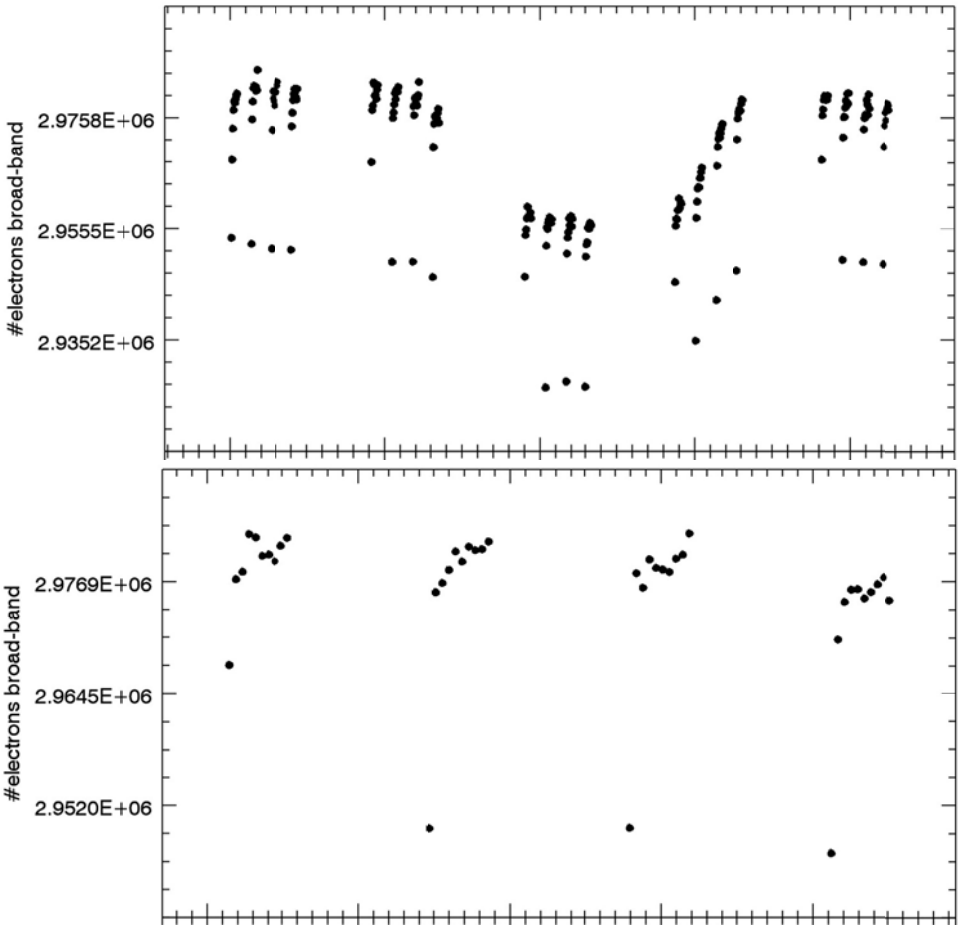

Figure 1.1-1: *The HAT-P-13 light curve serving as an illustration of the characteristic patterns present in some of the WFC3 IR-grism observations, including gaps and the flux "ramp" effect. Top – broadband flux measurements for five consecutive orbits; the large gaps are caused by earth occultations. Middle – a detail of the broadband flux measured during orbit 2; here the large gaps are due to moving data from the instrument to the spacecraft memory. Bottom – detail of the individual Nsamp measurements during orbit 2.*

1.2 Detector System Effects - Time Domain

For measuring changes in the detector system functionality with time, we constructed time series for the following diagnostics. The orbit-to-orbit gaps in the time series are marked with dashed vertical lines (see Figures 1.2-1 to 1.2-14).

1. **Broadband flux:** The broadband flux derived from the standard WFC3 data pipeline using the _flt files in the archive. The extraction of the spectrum is described in the main paper and references therein. The extracted spectrum was integrated in wavelength to determine the broadband flux. This provides a flux data point at the integration time cadence, or every destructive read. These results are shown in the top panel in the Figure 1.2-1 to 1.2-14 series.
2. **Nsamp broadband flux:** The broadband flux derived from Nsamp data using the _ima files in the archive. The methods for extracting the spectrum and determining the broadband flux are identical to above (1). This diagnostic produces a flux data point for every detector non-destructive read. Charge accumulates during the integration process, but the efficiency of conversion of photons to DN decreases with time. This causes consecutive non-destructive reads to show progressively smaller values as the detector is sampled up the ramp. These results are shown in the middle panel in the Figure 1.2-1 to 1.2-14 series.
3. **Nsamp relative flux:** The same as (2) except that the flux value for each Nsamp is normalized by the flux from the last Nsamp value before the reset. This normalization is useful for seeing details of how the detector functionality changes with time. These results are shown in the bottom panel in the Figure 1.2-1 to 1.2-14 series.

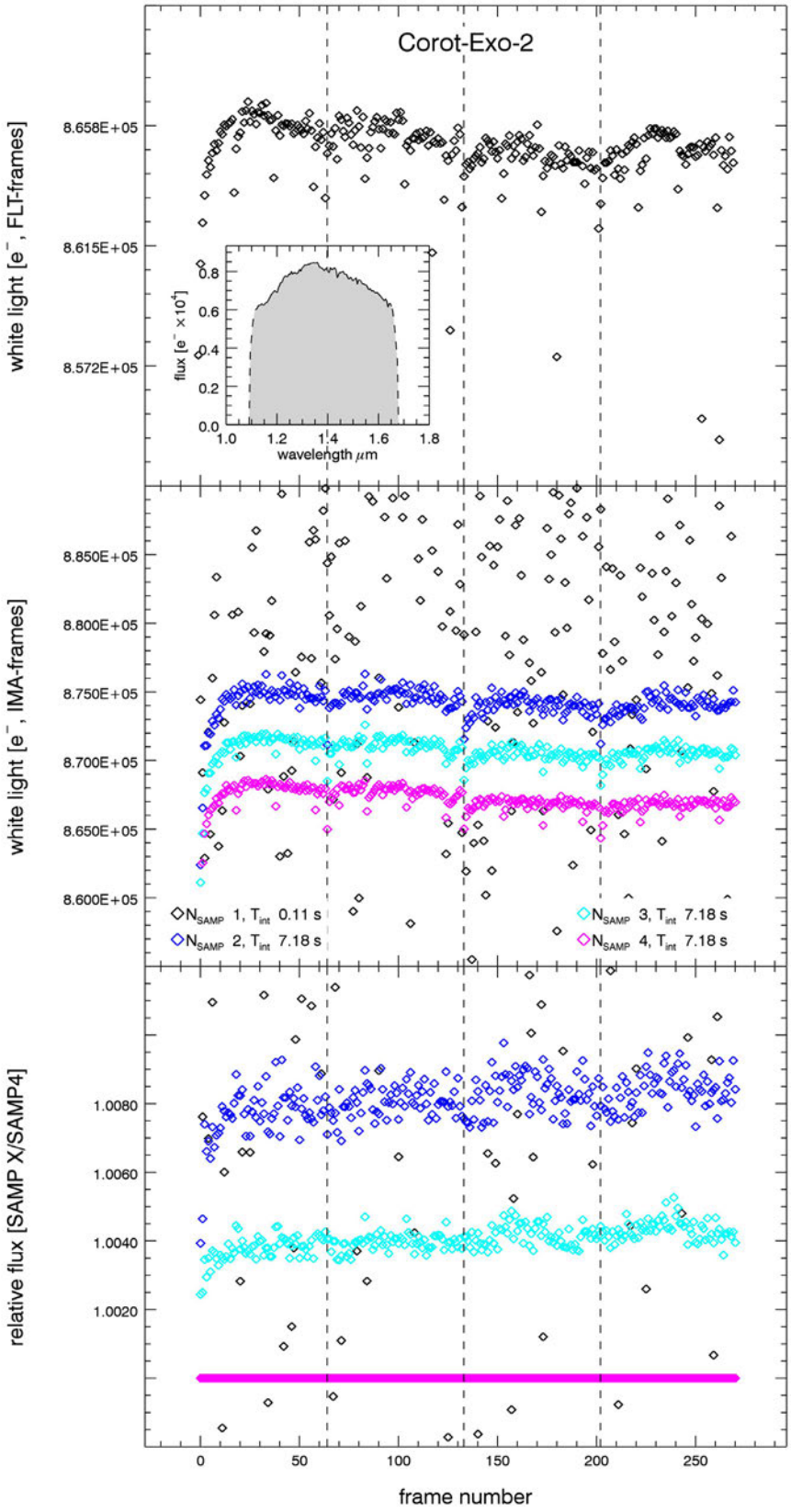
Corot-Exo-2
white light [e⁻ , FLT-frames]
8.658E+05
8.615E+05
8.572E+05
flux [e⁻ ×10⁴]
wavelength μm
white light [e⁻ , IMA-frames]
8.850E+05
8.800E+05
8.750E+05
8.700E+05
8.650E+05
8.600E+05
N_SAMP 1, T_int 0.11 s
N_SAMP 2, T_int 7.18 s
N_SAMP 3, T_int 7.18 s
N_SAMP 4, T_int 7.18 s
relative flux [SAMP X/SAMP4]
1.0080
1.0060
1.0040
1.0020
frame number

Figure 1.2-1.

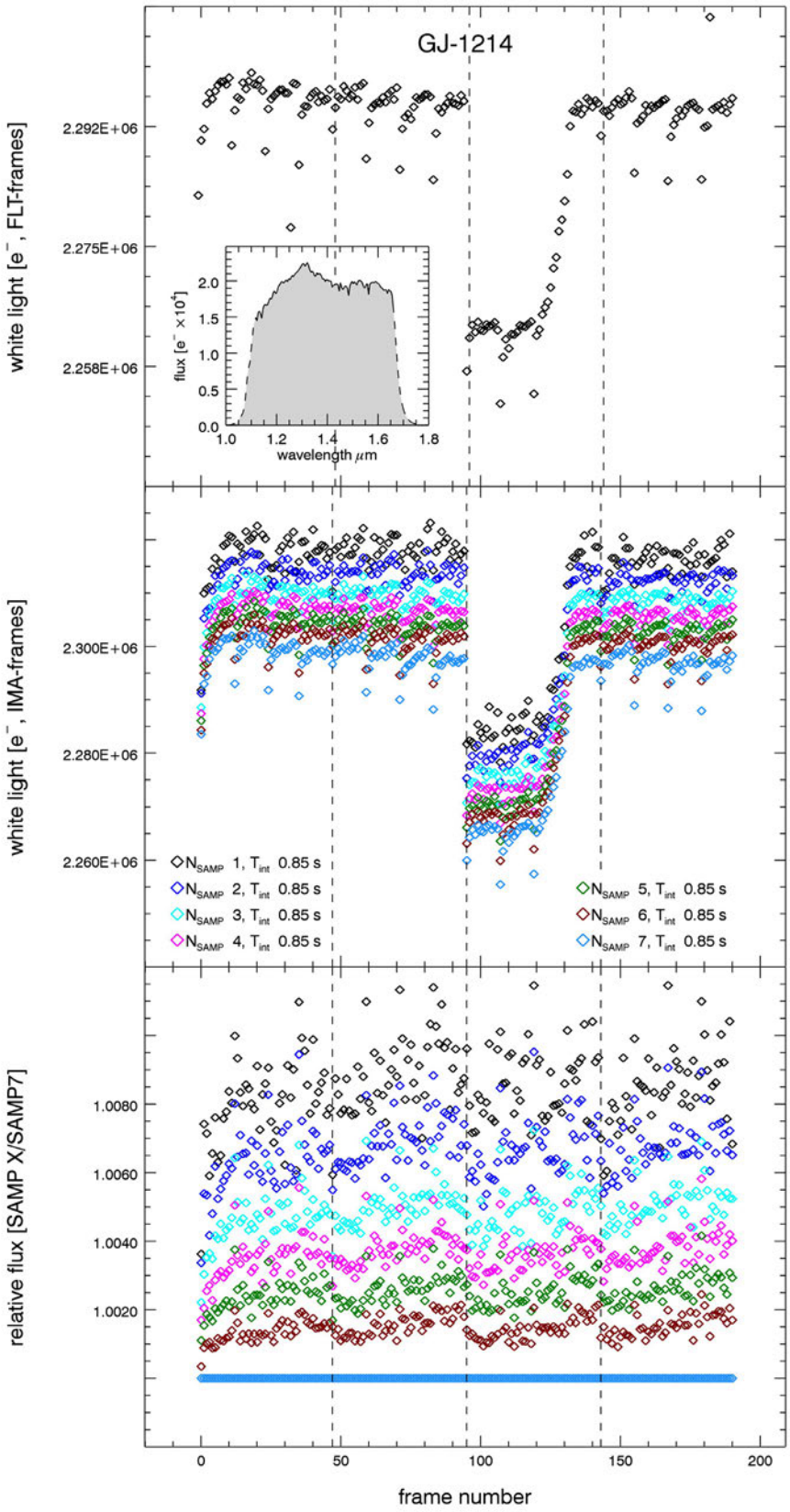
GJ-1214
white light [e⁻, FLT-frames]
2.292E+06
2.275E+06
2.258E+06
flux [e⁻ ×10⁴]
wavelength μm
white light [e⁻, IMA-frames]
2.300E+06
2.280E+06
2.260E+06
N_SAMP 1, T_int 0.85 s
N_SAMP 2, T_int 0.85 s
N_SAMP 3, T_int 0.85 s
N_SAMP 4, T_int 0.85 s
N_SAMP 5, T_int 0.85 s
N_SAMP 6, T_int 0.85 s
N_SAMP 7, T_int 0.85 s
relative flux [SAMP X/SAMP7]
1.0080
1.0060
1.0040
1.0020
frame number

Figure 1.2-2.

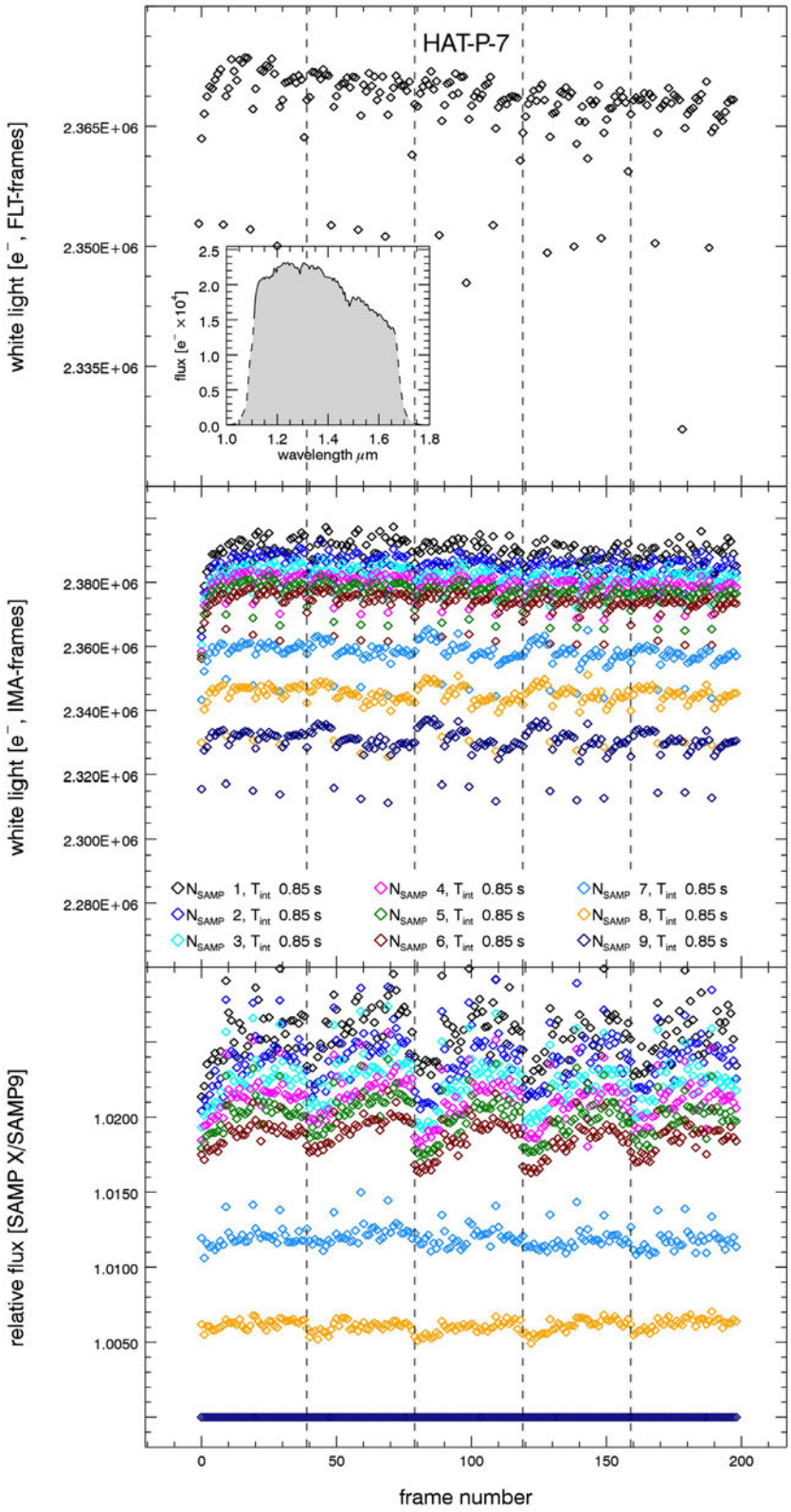
HAT-P-7
white light [e⁻, FLT-frames]
2.365E+06
2.350E+06
2.335E+06
flux [e⁻ ×10⁴]
wavelength μm
white light [e⁻, IMA-frames]
2.380E+06
2.360E+06
2.340E+06
2.320E+06
2.300E+06
2.280E+06
N_SAMP 1, T_int 0.85 s
N_SAMP 2, T_int 0.85 s
N_SAMP 3, T_int 0.85 s
N_SAMP 4, T_int 0.85 s
N_SAMP 5, T_int 0.85 s
N_SAMP 6, T_int 0.85 s
N_SAMP 7, T_int 0.85 s
N_SAMP 8, T_int 0.85 s
N_SAMP 9, T_int 0.85 s
relative flux [SAMP X/SAMP9]
1.0200
1.0150
1.0100
1.0050
frame number

Figure 1.2-3.

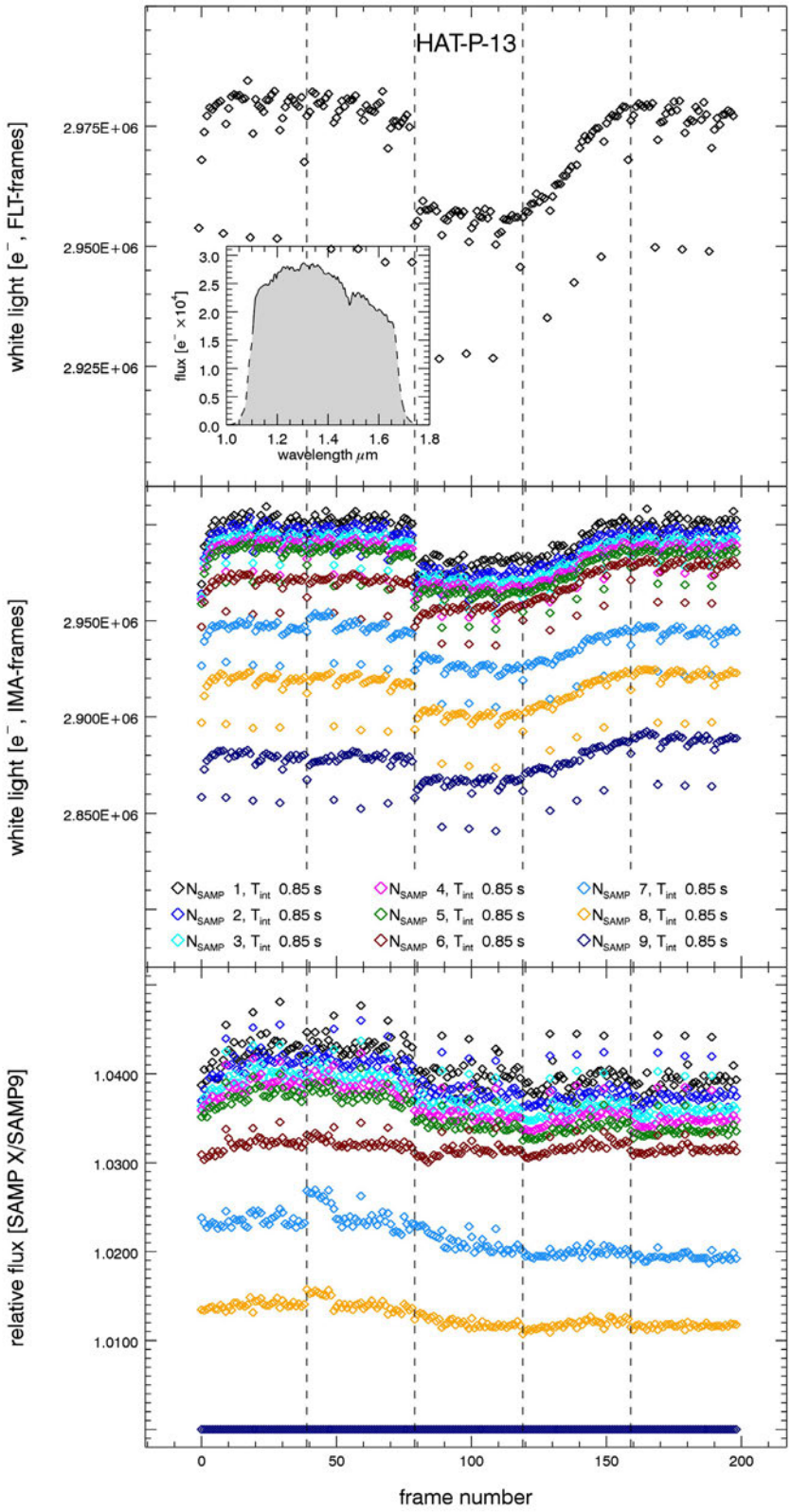
HAT-P-13
white light [e⁻, FLT-frames]
2.975E+06
2.950E+06
2.925E+06
flux [e⁻ ×10⁴]
wavelength μm
white light [e⁻, IMA-frames]
2.950E+06
2.900E+06
2.850E+06
N_SAMP 1, T_int 0.85 s
N_SAMP 2, T_int 0.85 s
N_SAMP 3, T_int 0.85 s
N_SAMP 4, T_int 0.85 s
N_SAMP 5, T_int 0.85 s
N_SAMP 6, T_int 0.85 s
N_SAMP 7, T_int 0.85 s
N_SAMP 8, T_int 0.85 s
N_SAMP 9, T_int 0.85 s
relative flux [SAMP X/SAMP9]
1.0400
1.0300
1.0200
1.0100
frame number

Figure 1.2-4.

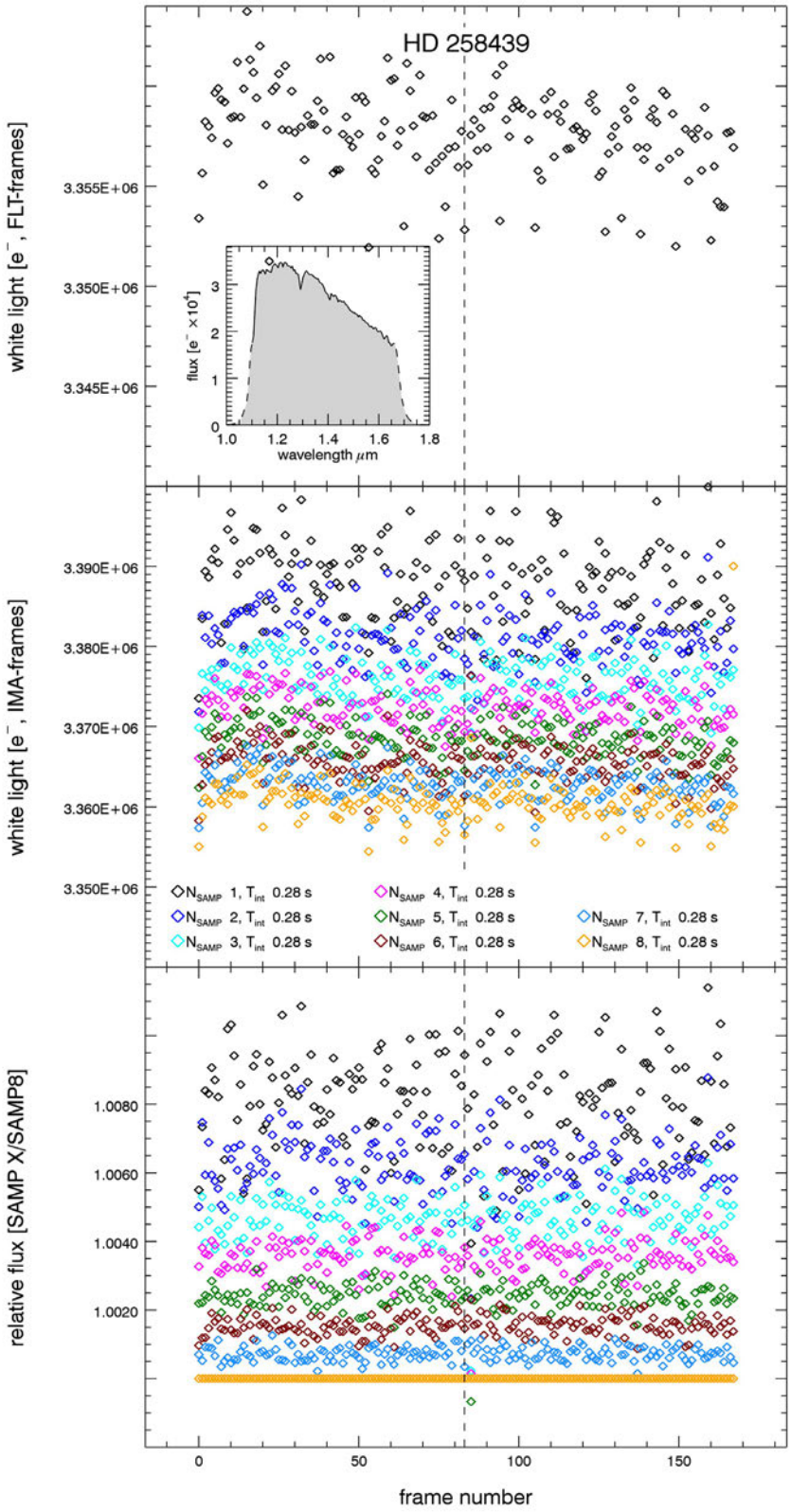
HD 258439
white light [e⁻, FLT-frames]
3.355E+06
3.350E+06
3.345E+06
flux [e⁻ ×10⁴]
wavelength μm
white light [e⁻, IMA-frames]
3.390E+06
3.380E+06
3.370E+06
3.360E+06
3.350E+06
N_SAMP 1, T_int 0.28 s
N_SAMP 2, T_int 0.28 s
N_SAMP 3, T_int 0.28 s
N_SAMP 4, T_int 0.28 s
N_SAMP 5, T_int 0.28 s
N_SAMP 6, T_int 0.28 s
N_SAMP 7, T_int 0.28 s
N_SAMP 8, T_int 0.28 s
relative flux [SAMP X/SAMP8]
1.0080
1.0060
1.0040
1.0020
0
50
100
150
frame number

Figure 1.2-5.

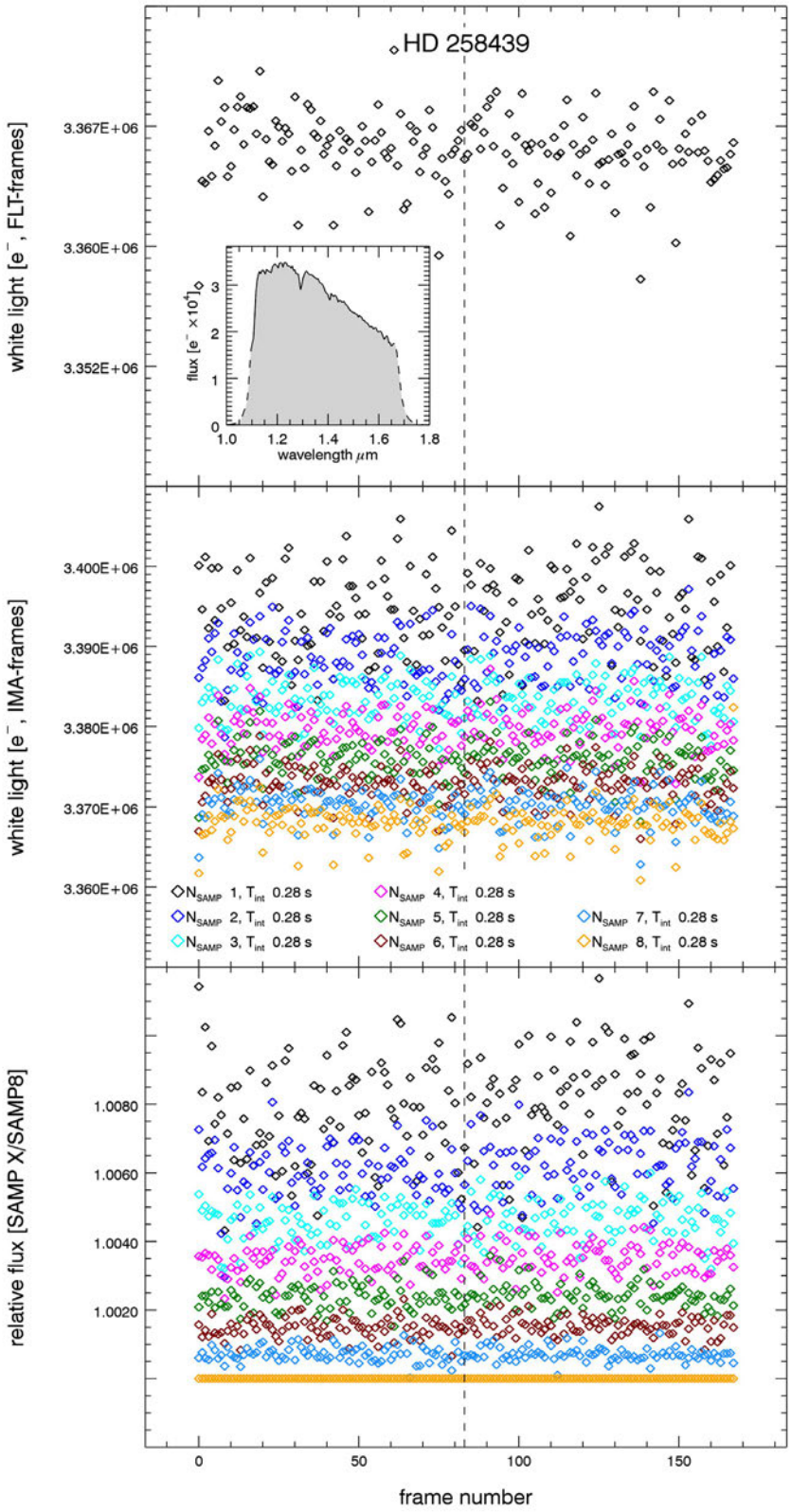
HD 258439
white light [e⁻, FLT-frames]
3.367E+06
3.360E+06
3.352E+06
flux [e⁻ ×10⁴]
wavelength μm
white light [e⁻, IMA-frames]
3.400E+06
3.390E+06
3.380E+06
3.370E+06
3.360E+06
N_SAMP 1, T_int 0.28 s
N_SAMP 2, T_int 0.28 s
N_SAMP 3, T_int 0.28 s
N_SAMP 4, T_int 0.28 s
N_SAMP 5, T_int 0.28 s
N_SAMP 6, T_int 0.28 s
N_SAMP 7, T_int 0.28 s
N_SAMP 8, T_int 0.28 s
relative flux [SAMP X/SAMP8]
1.0080
1.0060
1.0040
1.0020
0
50
100
150
frame number

Figure 1.2-6.

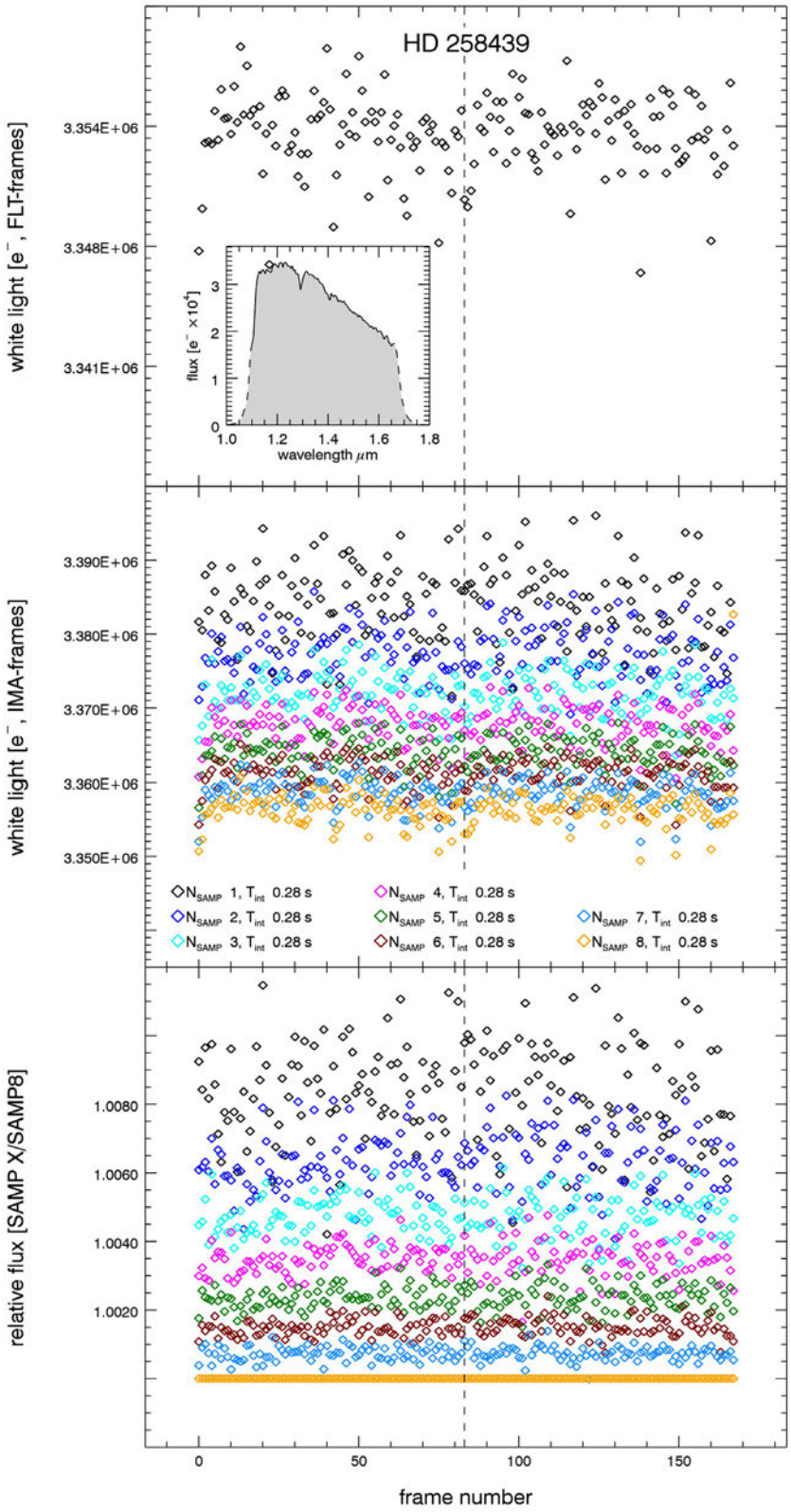
HD 258439
white light [e⁻, FLT-frames]
3.354E+06
3.348E+06
3.341E+06
flux [e⁻ ×10⁴]
wavelength μm
white light [e⁻, IMA-frames]
3.390E+06
3.380E+06
3.370E+06
3.360E+06
3.350E+06
N_SAMP 1, T_int 0.28 s
N_SAMP 2, T_int 0.28 s
N_SAMP 3, T_int 0.28 s
N_SAMP 4, T_int 0.28 s
N_SAMP 5, T_int 0.28 s
N_SAMP 6, T_int 0.28 s
N_SAMP 7, T_int 0.28 s
N_SAMP 8, T_int 0.28 s
relative flux [SAMP X/SAMP8]
1.0080
1.0060
1.0040
1.0020
0
50
100
150
frame number

Figure 1.2-7.

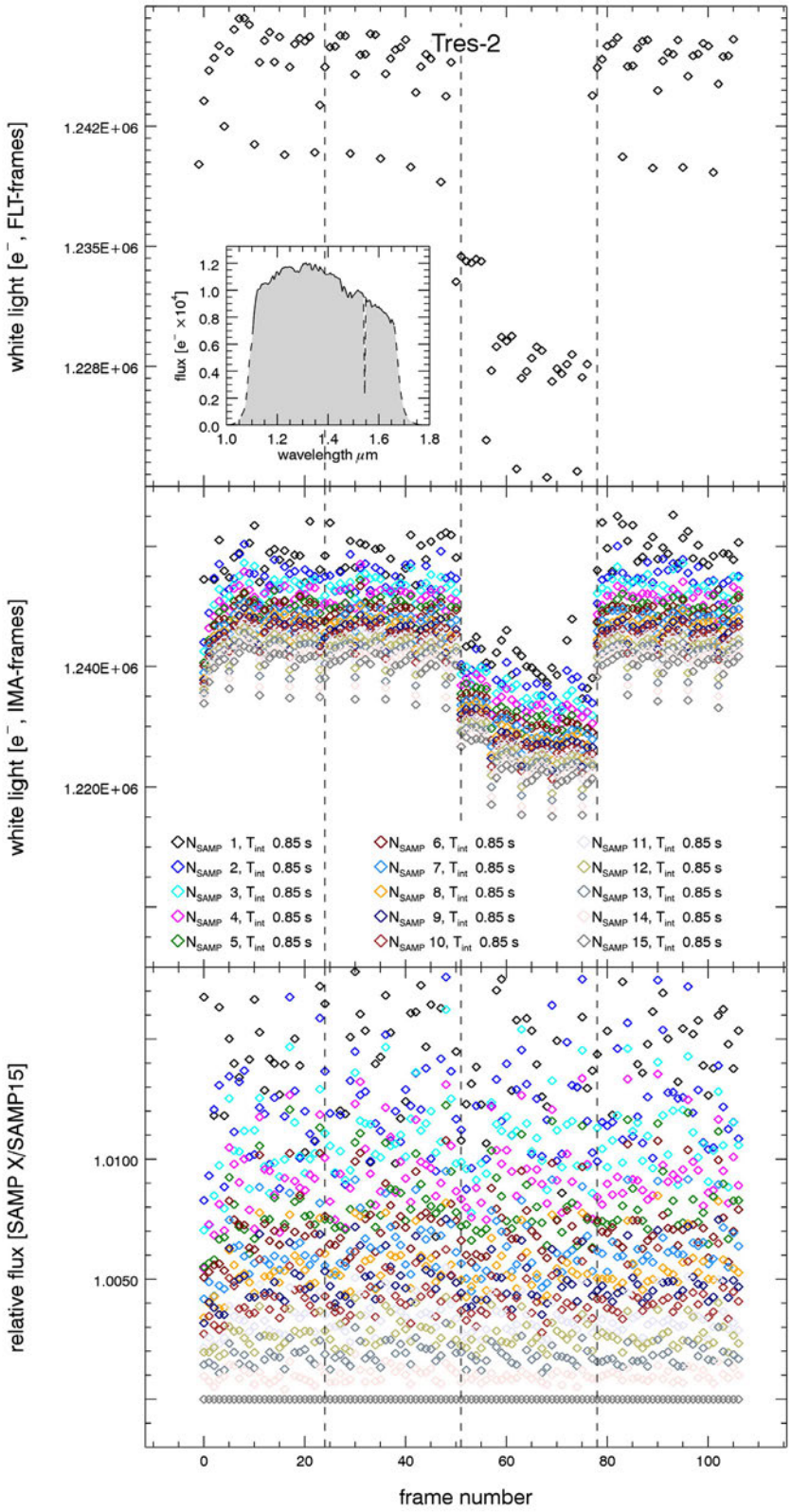
Tres-2
white light [e⁻, FLT-frames]
1.242E+06
1.235E+06
1.228E+06
flux [e⁻ ×10⁴]
wavelength μm
white light [e⁻, IMA-frames]
1.240E+06
1.220E+06
N_SAMP 1, T_int 0.85 s
N_SAMP 2, T_int 0.85 s
N_SAMP 3, T_int 0.85 s
N_SAMP 4, T_int 0.85 s
N_SAMP 5, T_int 0.85 s
N_SAMP 6, T_int 0.85 s
N_SAMP 7, T_int 0.85 s
N_SAMP 8, T_int 0.85 s
N_SAMP 9, T_int 0.85 s
N_SAMP 10, T_int 0.85 s
N_SAMP 11, T_int 0.85 s
N_SAMP 12, T_int 0.85 s
N_SAMP 13, T_int 0.85 s
N_SAMP 14, T_int 0.85 s
N_SAMP 15, T_int 0.85 s
relative flux [SAMP X/SAMP15]
1.0100
1.0050
frame number

Figure 1.2-8.

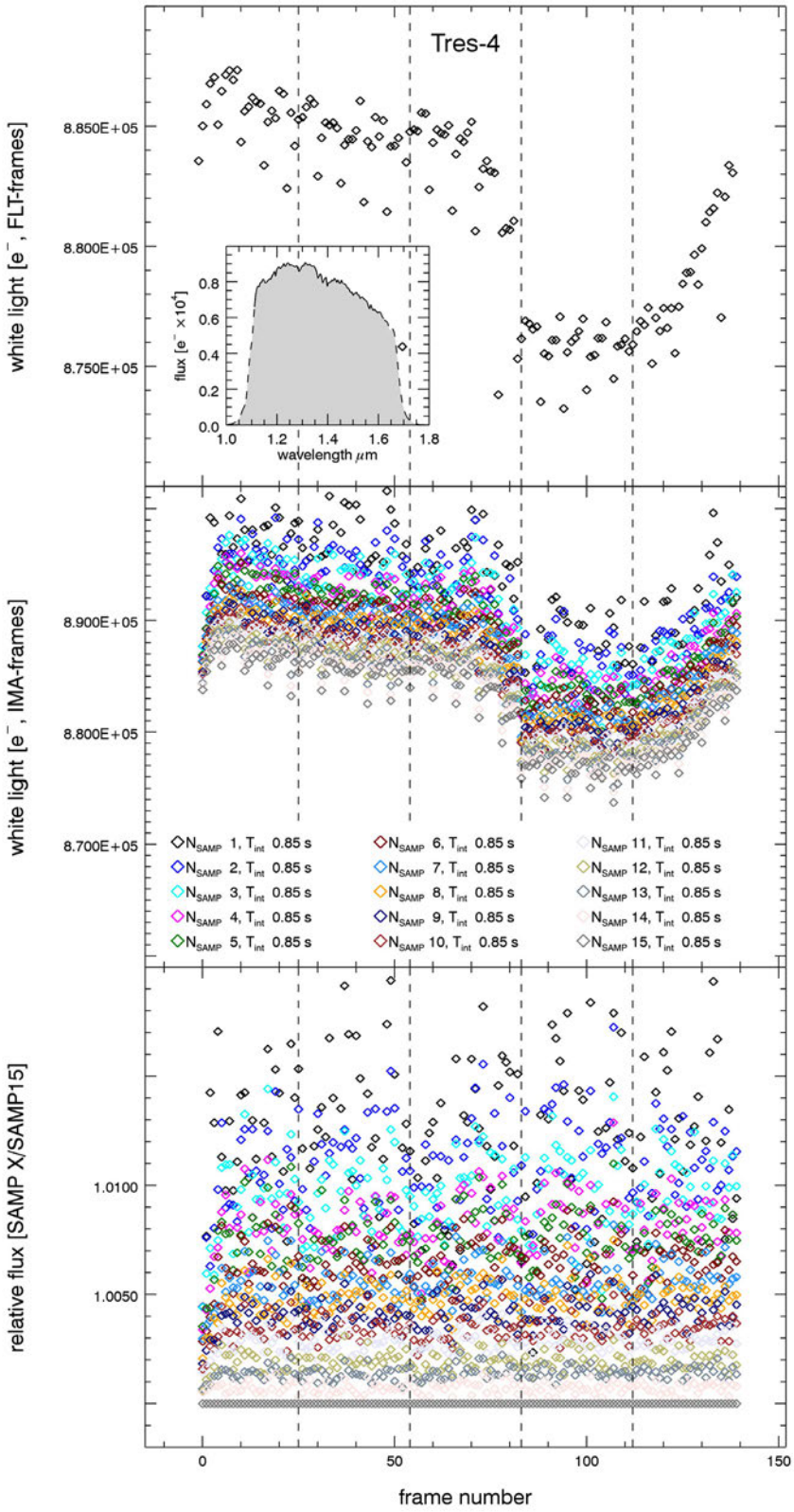
Tres-4
white light [e⁻, FLT-frames]
8.850E+05
8.800E+05
8.750E+05
flux [e⁻ ×10⁴]
wavelength μm
white light [e⁻, IMA-frames]
8.900E+05
8.800E+05
8.700E+05
N_SAMP 1, T_int 0.85 s
N_SAMP 2, T_int 0.85 s
N_SAMP 3, T_int 0.85 s
N_SAMP 4, T_int 0.85 s
N_SAMP 5, T_int 0.85 s
N_SAMP 6, T_int 0.85 s
N_SAMP 7, T_int 0.85 s
N_SAMP 8, T_int 0.85 s
N_SAMP 9, T_int 0.85 s
N_SAMP 10, T_int 0.85 s
N_SAMP 11, T_int 0.85 s
N_SAMP 12, T_int 0.85 s
N_SAMP 13, T_int 0.85 s
N_SAMP 14, T_int 0.85 s
N_SAMP 15, T_int 0.85 s
relative flux [SAMP X/SAMP15]
1.0100
1.0050
frame number

Figure 1.2-9.

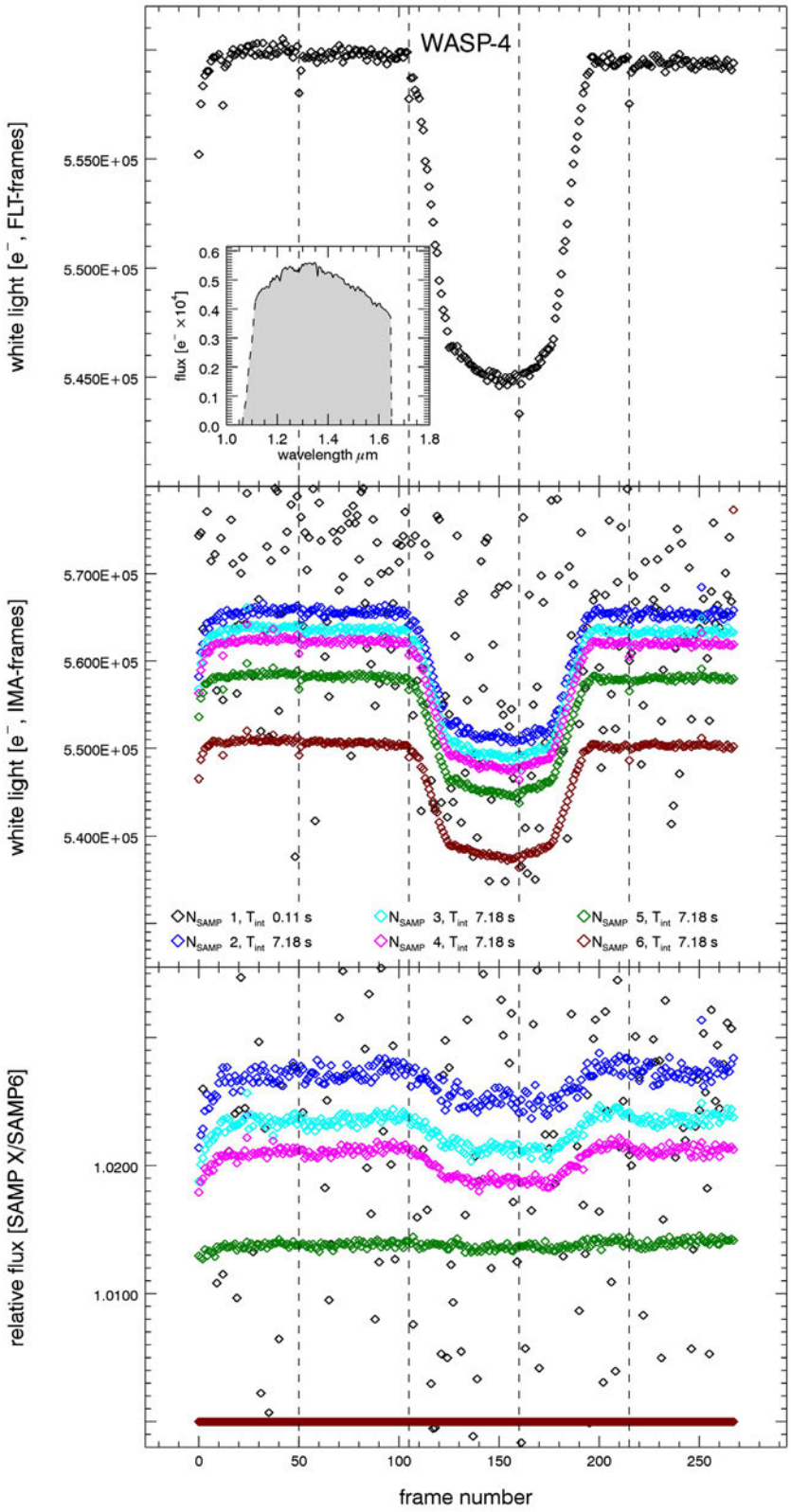
WASP-4
white light [e⁻, FLT-frames]
5.550E+05
5.500E+05
5.450E+05
flux [e⁻ ×10⁴]
wavelength μm
white light [e⁻, IMA-frames]
5.700E+05
5.600E+05
5.500E+05
5.400E+05
N_SAMP 1, T_int 0.11 s
N_SAMP 2, T_int 7.18 s
N_SAMP 3, T_int 7.18 s
N_SAMP 4, T_int 7.18 s
N_SAMP 5, T_int 7.18 s
N_SAMP 6, T_int 7.18 s
relative flux [SAMP X/SAMP6]
1.0200
1.0100
frame number

Figure 1.2-10.

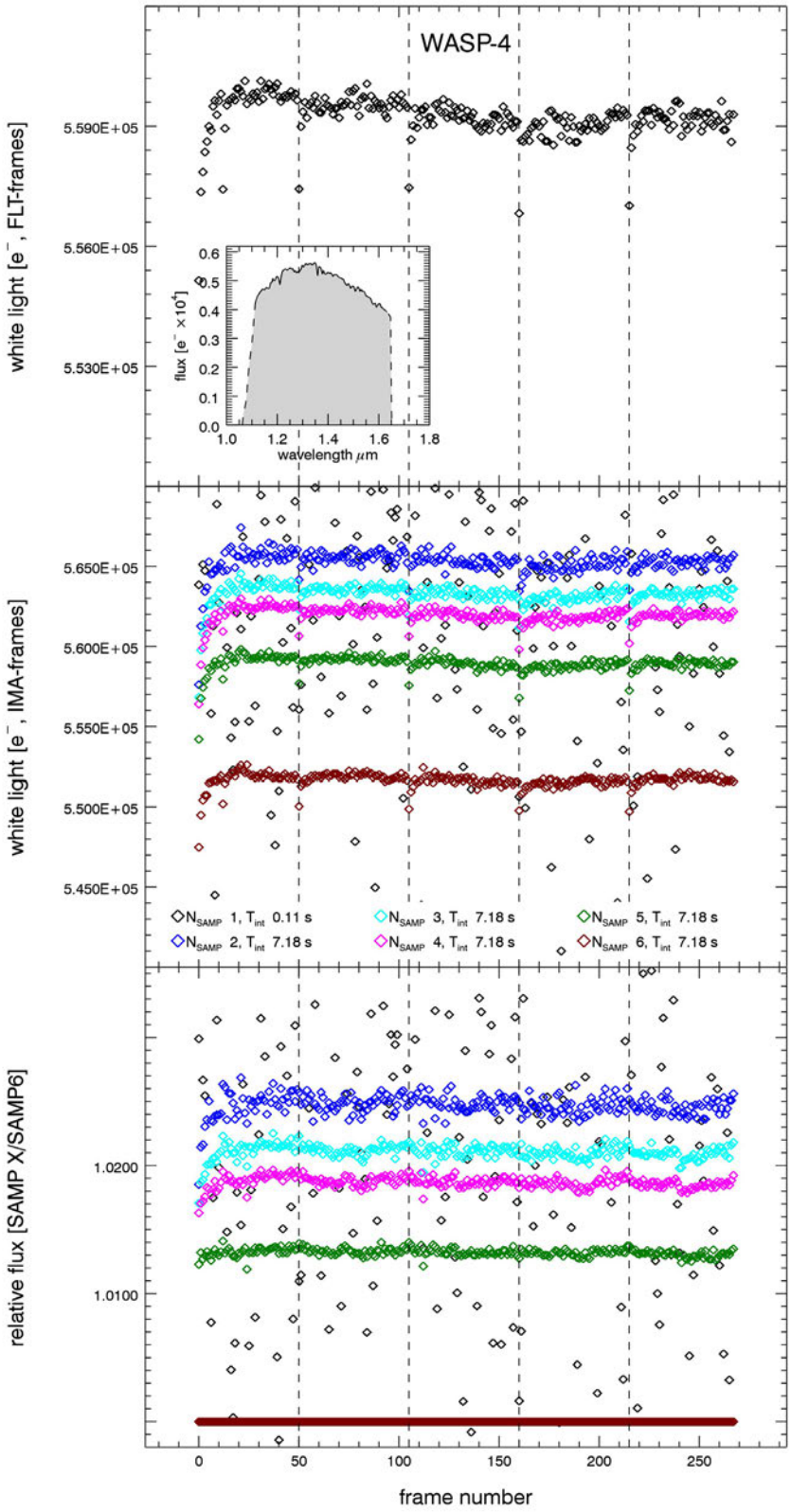
WASP-4
white light [e⁻, FLT-frames]
5.590E+05
5.560E+05
5.530E+05
flux [e⁻ ×10⁴]
wavelength μm
white light [e⁻, IMA-frames]
5.650E+05
5.600E+05
5.550E+05
5.500E+05
5.450E+05
N_SAMP 1, T_int 0.11 s
N_SAMP 2, T_int 7.18 s
N_SAMP 3, T_int 7.18 s
N_SAMP 4, T_int 7.18 s
N_SAMP 5, T_int 7.18 s
N_SAMP 6, T_int 7.18 s
relative flux [SAMP X/SAMP6]
1.0200
1.0100
frame number

Figure 1.2-11.

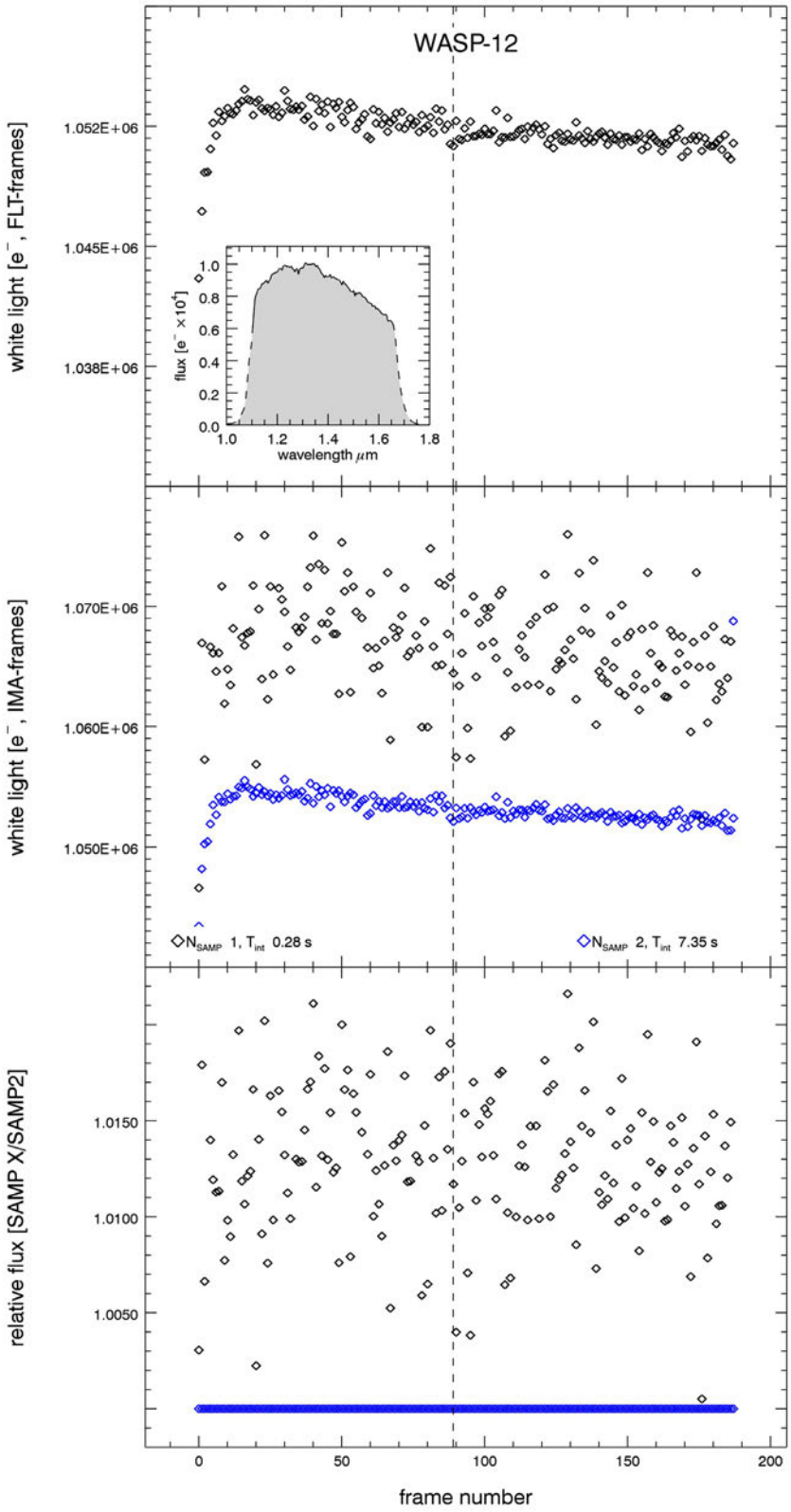
WASP-12
white light [e⁻, FLT-frames]
1.052E+06
1.045E+06
1.038E+06
flux [e⁻ ×10⁴]
wavelength μm
white light [e⁻, IMA-frames]
1.070E+06
1.060E+06
1.050E+06
N_SAMP 1, T_int 0.28 s
N_SAMP 2, T_int 7.35 s
relative flux [SAMP X/SAMP2]
1.0150
1.0100
1.0050
frame number

Figure 1.2-12.

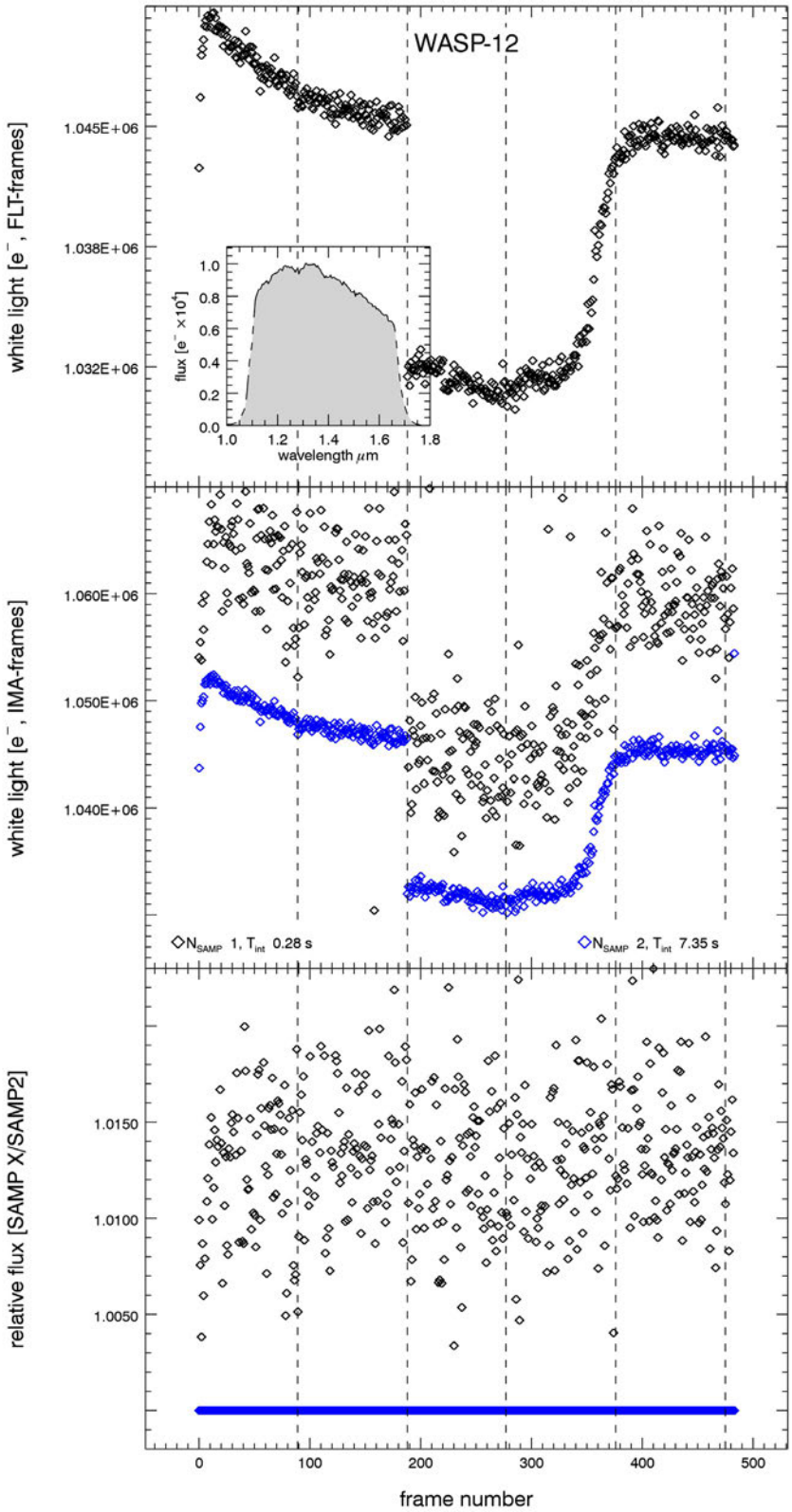
WASP-12
white light [e⁻, FLT-frames]
1.045E+06
1.038E+06
1.032E+06
flux [e⁻ ×10⁴]
wavelength μm
white light [e⁻, IMA-frames]
1.060E+06
1.050E+06
1.040E+06
N_SAMP 1, T_int 0.28 s
N_SAMP 2, T_int 7.35 s
relative flux [SAMP X/SAMP2]
1.0150
1.0100
1.0050
frame number

Figure 1.2-13.

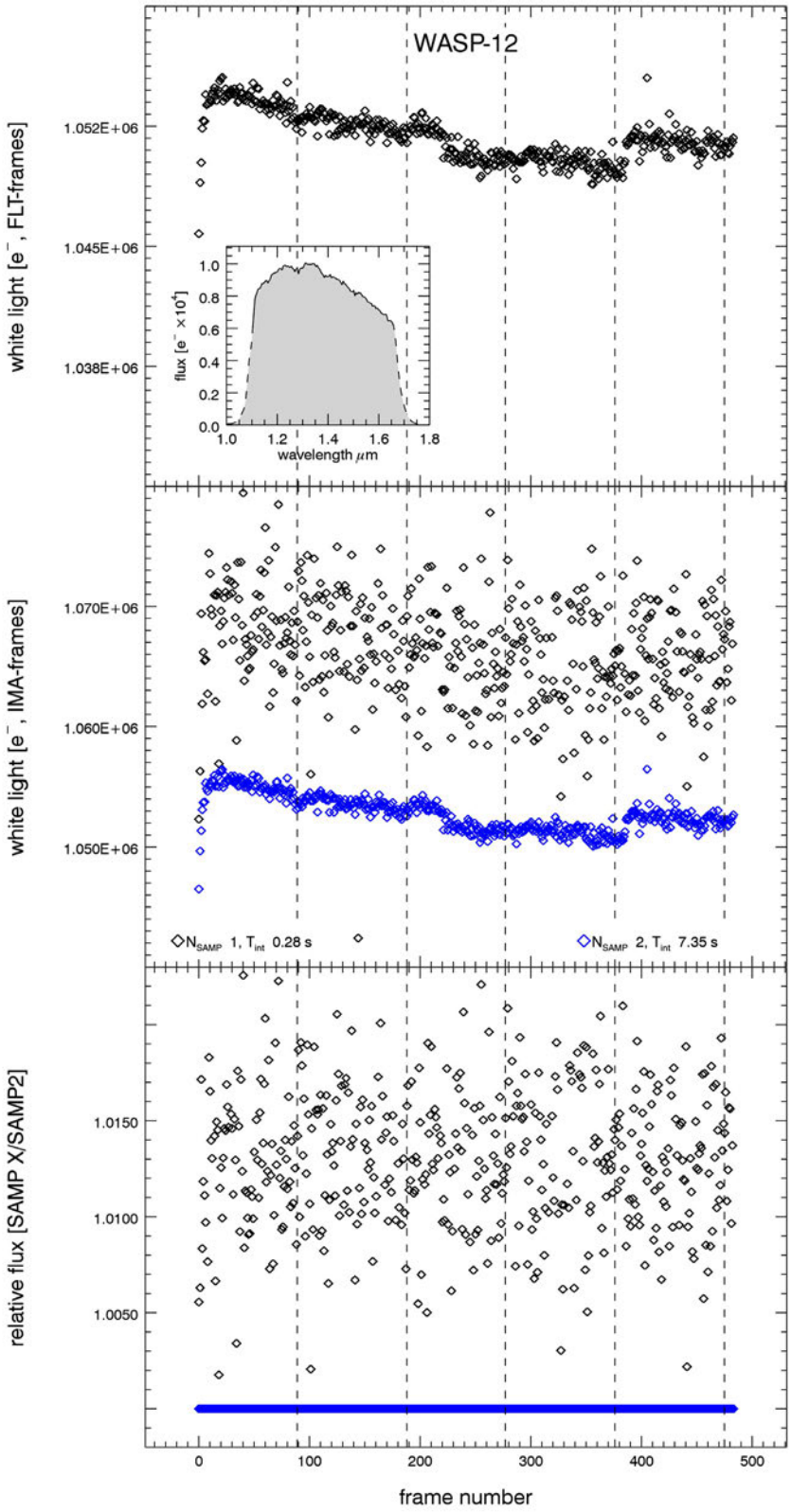
WASP-12
white light [e⁻, FLT-frames]
1.052E+06
1.045E+06
1.038E+06
flux [e⁻ ×10⁴]
wavelength μm
white light [e⁻, IMA-frames]
1.070E+06
1.060E+06
1.050E+06
N_SAMP 1, T_int 0.28 s
N_SAMP 2, T_int 7.35 s
relative flux [SAMP X/SAMP2]
1.0150
1.0100
1.0050
frame number

Figure 1.2-14.

1.3 Detector System Effects – Charge Domain

For measuring changes in the detector system functionality as a function of charge collected, or what fraction of the detector well is used during an integration, we used two diagnostics (see Figures 1.3-1 to 1.3-14). Both of these diagnostics use _ima (Nsamp) data to probe how detector functionality changes as the well is filled. We have chosen to implement these diagnostics by averaging the flux together for many pixels to assess the collective performance of the detector system.

1. **Detector Linearity Relation:** This diagnostic is created by taking a region around the spectrum, making the cumulative histogram of the flux values in DN, and selecting those pixels with 98th percentile value, or higher. These represent the bright pixels that contain most of the flux in the spectrum and are good choices to probe how the measurement is affected as the detector well is filled during the integration time. The detector linearity relation, which is never truly linear, is a standard diagnostic for infrared detectors. The WFC3 pipeline implements a linearity correction. Our results for the detector linearity relation for each observation are shown in the top panel in the Figure 1.3-1 to 1.3-14 series.
2. **Derivative of the Detector Linearity Relation:** The derivative of the detector linearity relation is an excellent tool for identifying departures from linearity. A linear slope type pattern for this diagnostic implies a constant departure from linearity; the WFC3 detector shows this effect, which explains why the Nsamp broadband flux values decrease with the Nsamp index. A pair of linear slope-type patterns intersecting at a "knee" indicate change in the non-linearity relation. This occurs in the WFC3 detector when Nsamp values exceed ~40,000 DN. When this effect occurs, it is seen in the significantly reduced Nsamp broadband flux values (see Hat-P-13b for example). In these cases, the linearity correction applied by the standard WFC3 pipeline could be problematic. Our results for the derivative of the detector linearity relation for each observation are shown in the lower panel in the Figure 1.3-1 to 1.3-14 series.

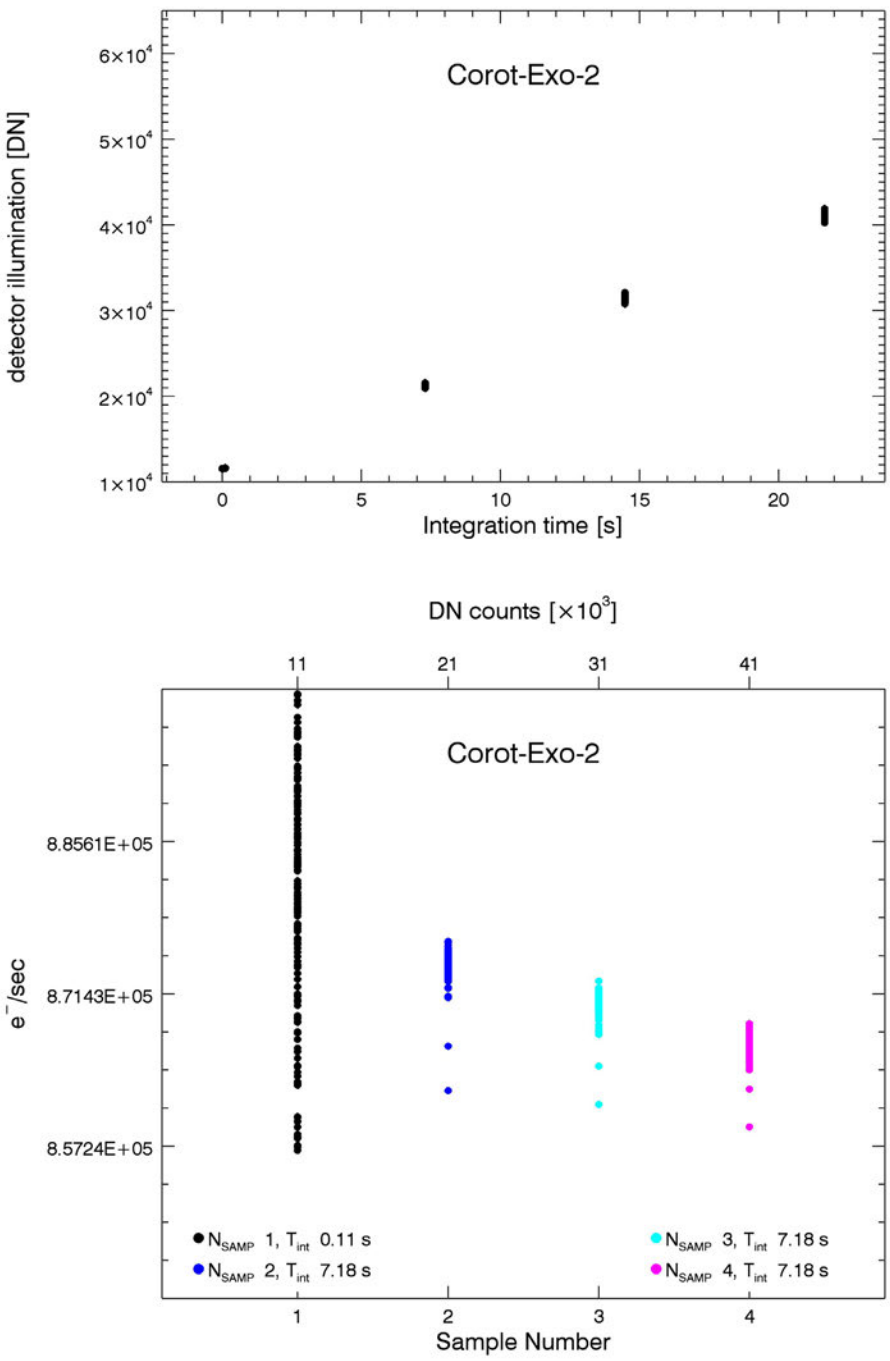
Corot-Exo-2
detector illumination [DN]
6×10^4
5×10^4
4×10^4
3×10^4
2×10^4
1×10^4
0
5
10
15
20
Integration time [s]
DN counts [×10^3]
11
21
31
41
Corot-Exo-2
8.8561E+05
8.7143E+05
8.5724E+05
e^-/sec
N_SAMP 1, T_int 0.11 s
N_SAMP 2, T_int 7.18 s
N_SAMP 3, T_int 7.18 s
N_SAMP 4, T_int 7.18 s
1
2
3
4
Sample Number

Figure 13.1-1.

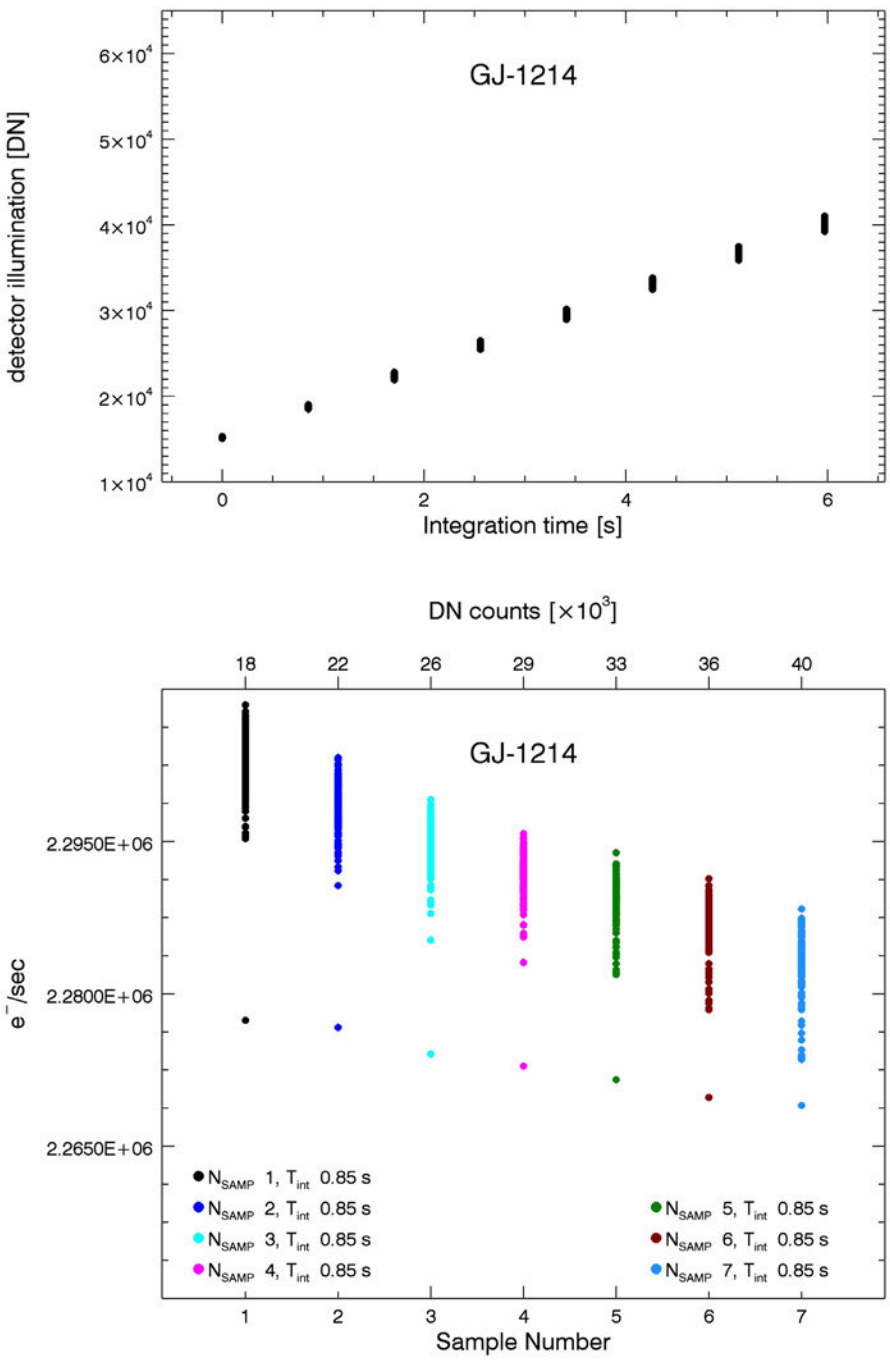
GJ-1214
detector illumination [DN]
6×10^4
5×10^4
4×10^4
3×10^4
2×10^4
1×10^4
0
2
4
6
Integration time [s]
DN counts [×10^3]
18
22
26
29
33
36
40
GJ-1214
e^-/sec
2.2950E+06
2.2800E+06
2.2650E+06
N_SAMP 1, T_int 0.85 s
N_SAMP 2, T_int 0.85 s
N_SAMP 3, T_int 0.85 s
N_SAMP 4, T_int 0.85 s
N_SAMP 5, T_int 0.85 s
N_SAMP 6, T_int 0.85 s
N_SAMP 7, T_int 0.85 s
1
2
3
4
5
6
7
Sample Number

Figure 13.1-2.

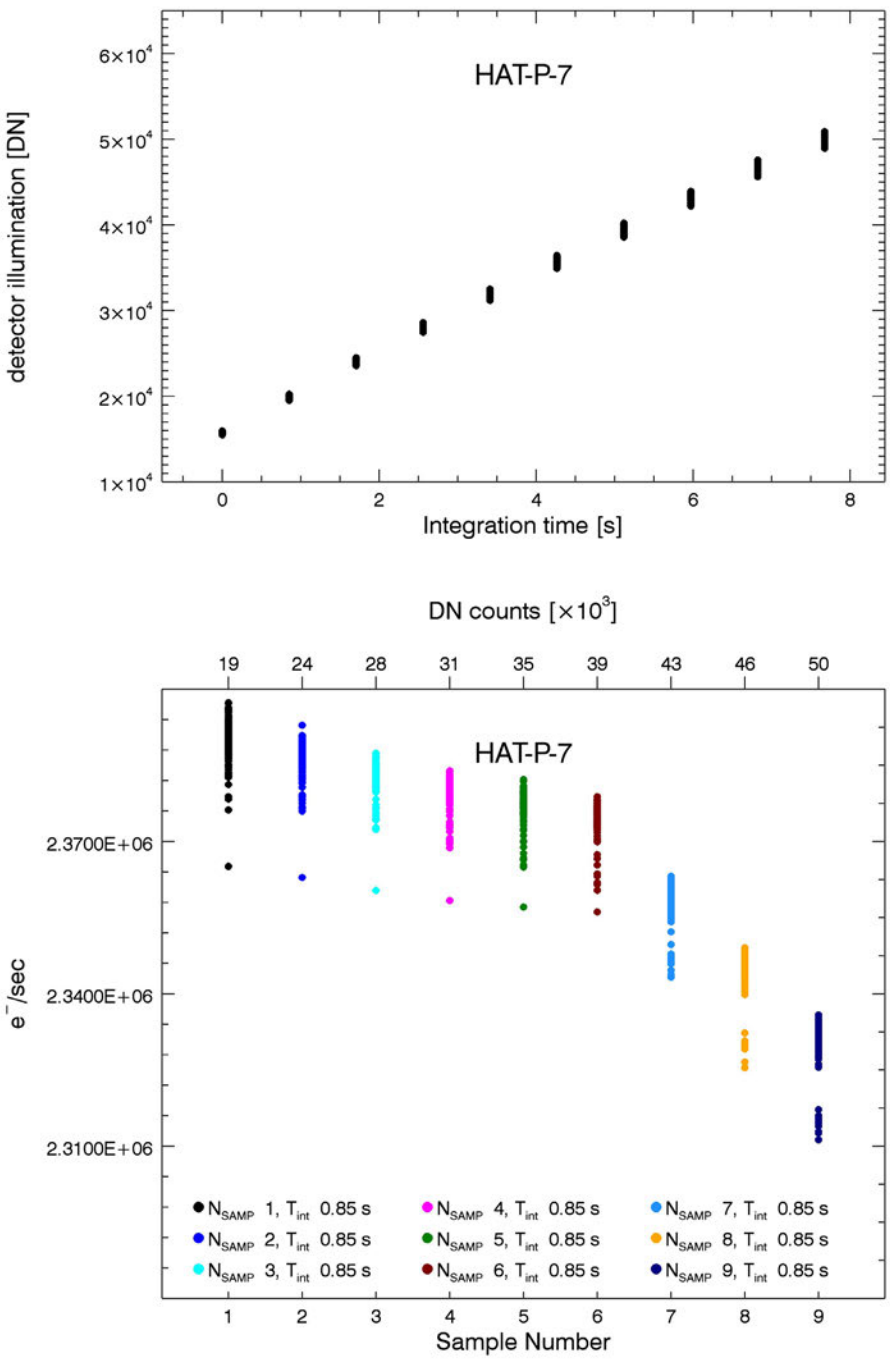
HAT-P-7
detector illumination [DN]
Integration time [s]
DN counts [×10^3]
HAT-P-7
e⁻/sec
Sample Number
N_SAMP 1, T_int 0.85 s
N_SAMP 2, T_int 0.85 s
N_SAMP 3, T_int 0.85 s
N_SAMP 4, T_int 0.85 s
N_SAMP 5, T_int 0.85 s
N_SAMP 6, T_int 0.85 s
N_SAMP 7, T_int 0.85 s
N_SAMP 8, T_int 0.85 s
N_SAMP 9, T_int 0.85 s

Figure 13.1-3.

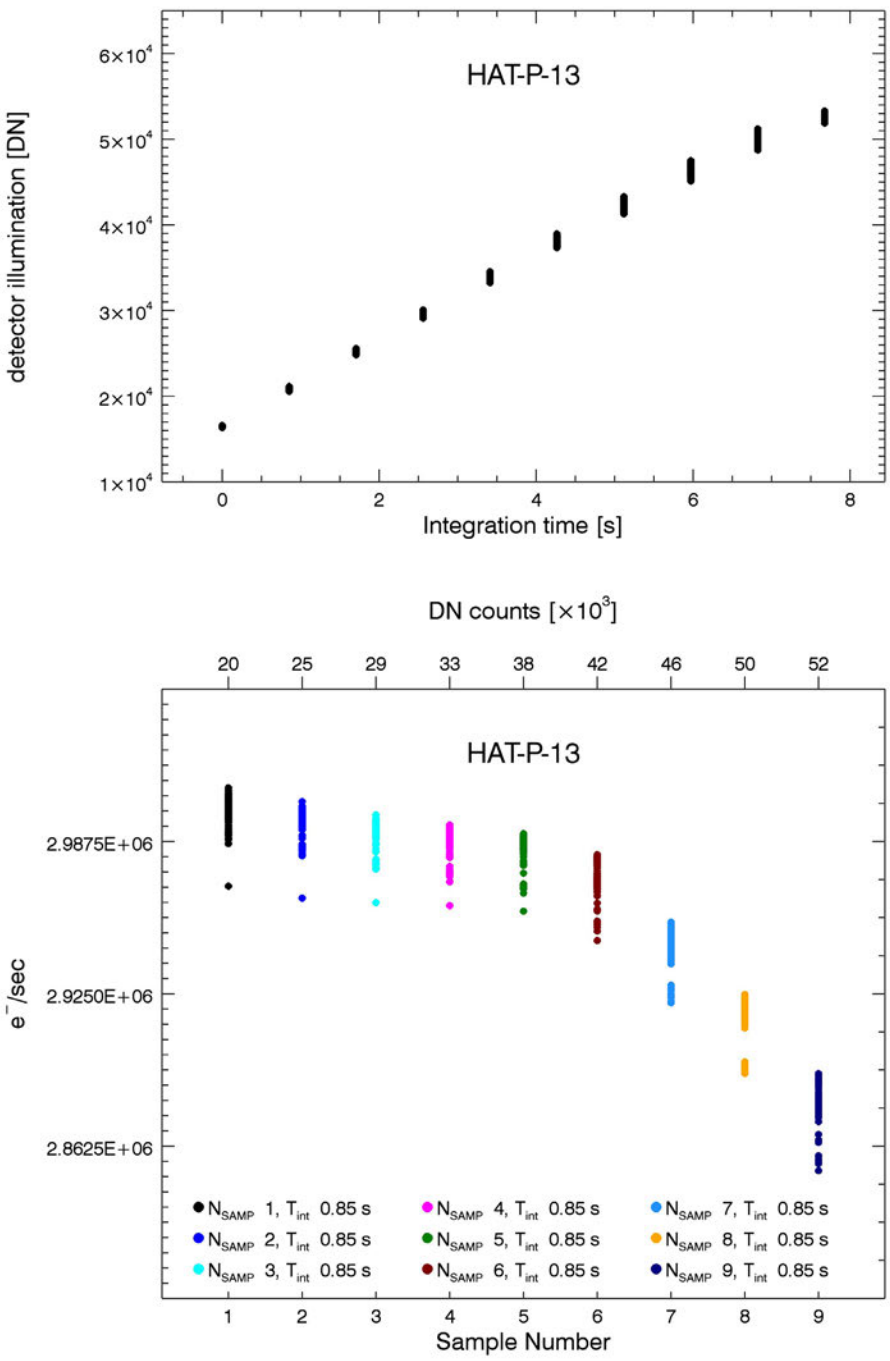
HAT-P-13
detector illumination [DN]
Integration time [s]
DN counts [×10^3]
HAT-P-13
e⁻/sec
Sample Number
N_SAMP 1, T_int 0.85 s
N_SAMP 2, T_int 0.85 s
N_SAMP 3, T_int 0.85 s
N_SAMP 4, T_int 0.85 s
N_SAMP 5, T_int 0.85 s
N_SAMP 6, T_int 0.85 s
N_SAMP 7, T_int 0.85 s
N_SAMP 8, T_int 0.85 s
N_SAMP 9, T_int 0.85 s

Figure 13.1-4.

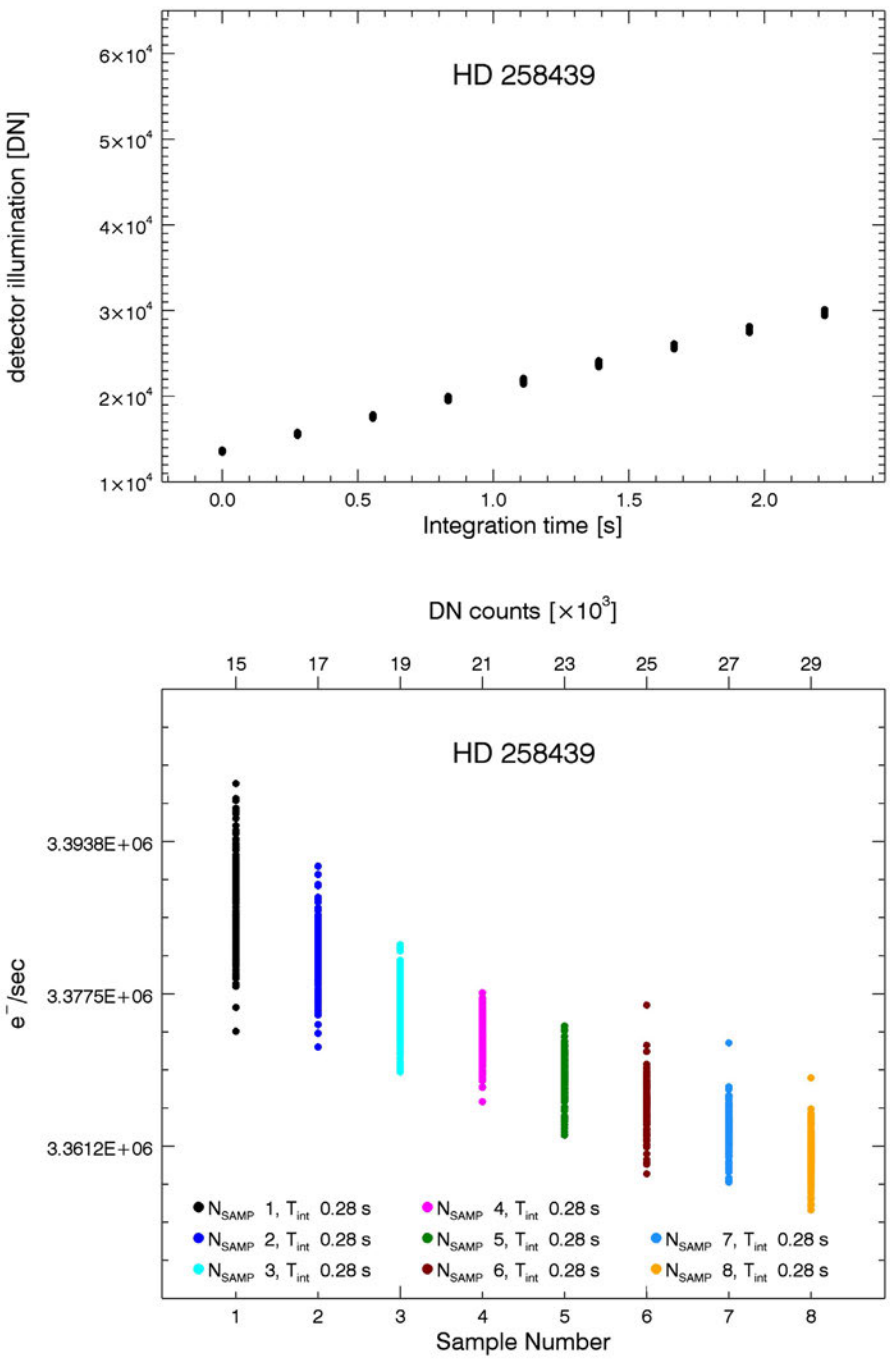
HD 258439
detector illumination [DN]
6×10^4
5×10^4
4×10^4
3×10^4
2×10^4
1×10^4
0.0
0.5
1.0
1.5
2.0
Integration time [s]
DN counts [×10^3]
15
17
19
21
23
25
27
29
HD 258439
e⁻/sec
3.3938E+06
3.3775E+06
3.3612E+06
N_SAMP 1, T_int 0.28 s
N_SAMP 2, T_int 0.28 s
N_SAMP 3, T_int 0.28 s
N_SAMP 4, T_int 0.28 s
N_SAMP 5, T_int 0.28 s
N_SAMP 6, T_int 0.28 s
N_SAMP 7, T_int 0.28 s
N_SAMP 8, T_int 0.28 s
1
2
3
4
5
6
7
8
Sample Number

Figure 13.1-5.

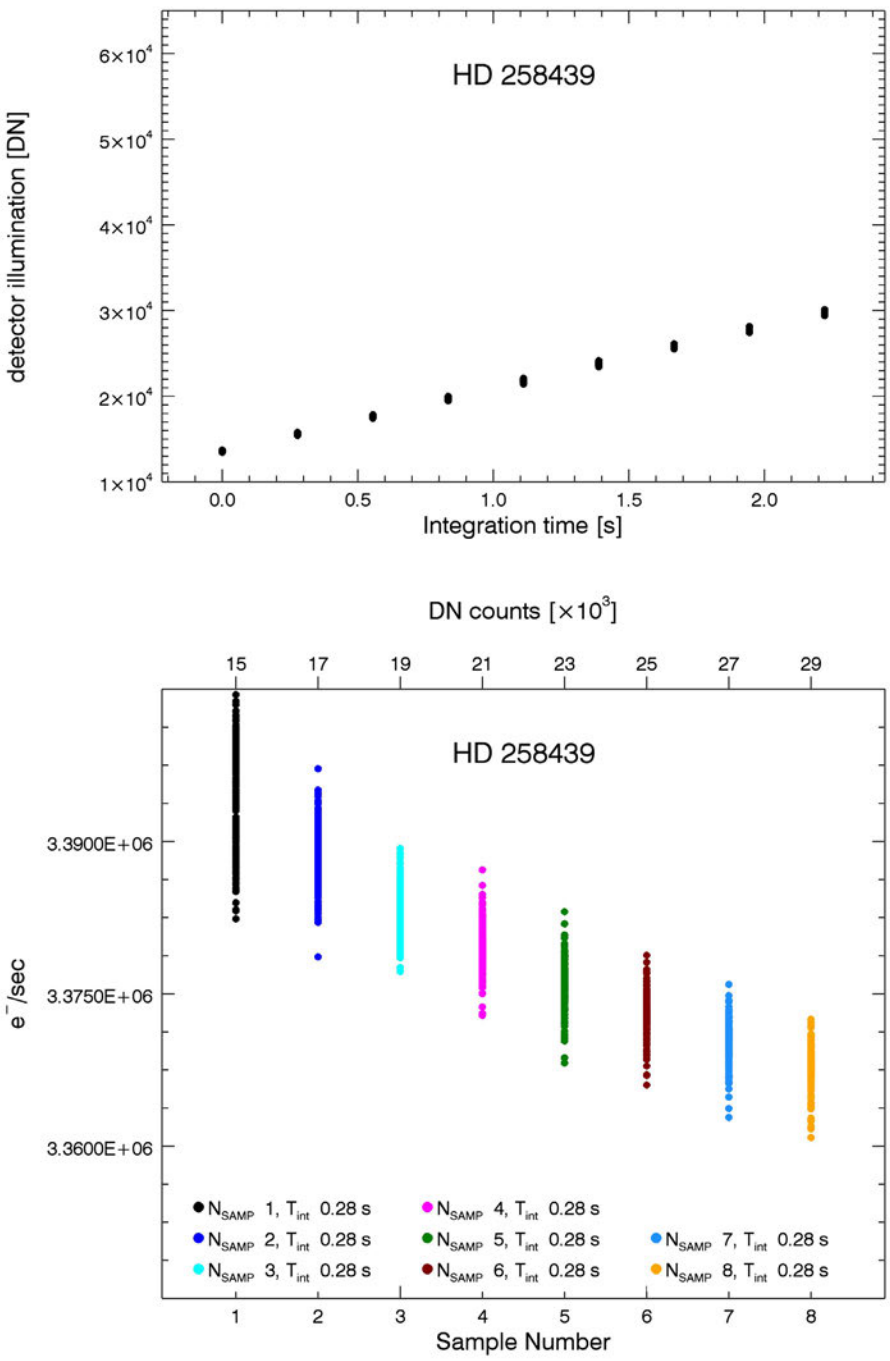
HD 258439
detector illumination [DN]
6×10^4
5×10^4
4×10^4
3×10^4
2×10^4
1×10^4
0.0
0.5
1.0
1.5
2.0
Integration time [s]
DN counts [×10^3]
15
17
19
21
23
25
27
29
HD 258439
e⁻/sec
3.3900E+06
3.3750E+06
3.3600E+06
N_SAMP 1, T_int 0.28 s
N_SAMP 2, T_int 0.28 s
N_SAMP 3, T_int 0.28 s
N_SAMP 4, T_int 0.28 s
N_SAMP 5, T_int 0.28 s
N_SAMP 6, T_int 0.28 s
N_SAMP 7, T_int 0.28 s
N_SAMP 8, T_int 0.28 s
1
2
3
4
5
6
7
8
Sample Number

Figure 13.1-6.

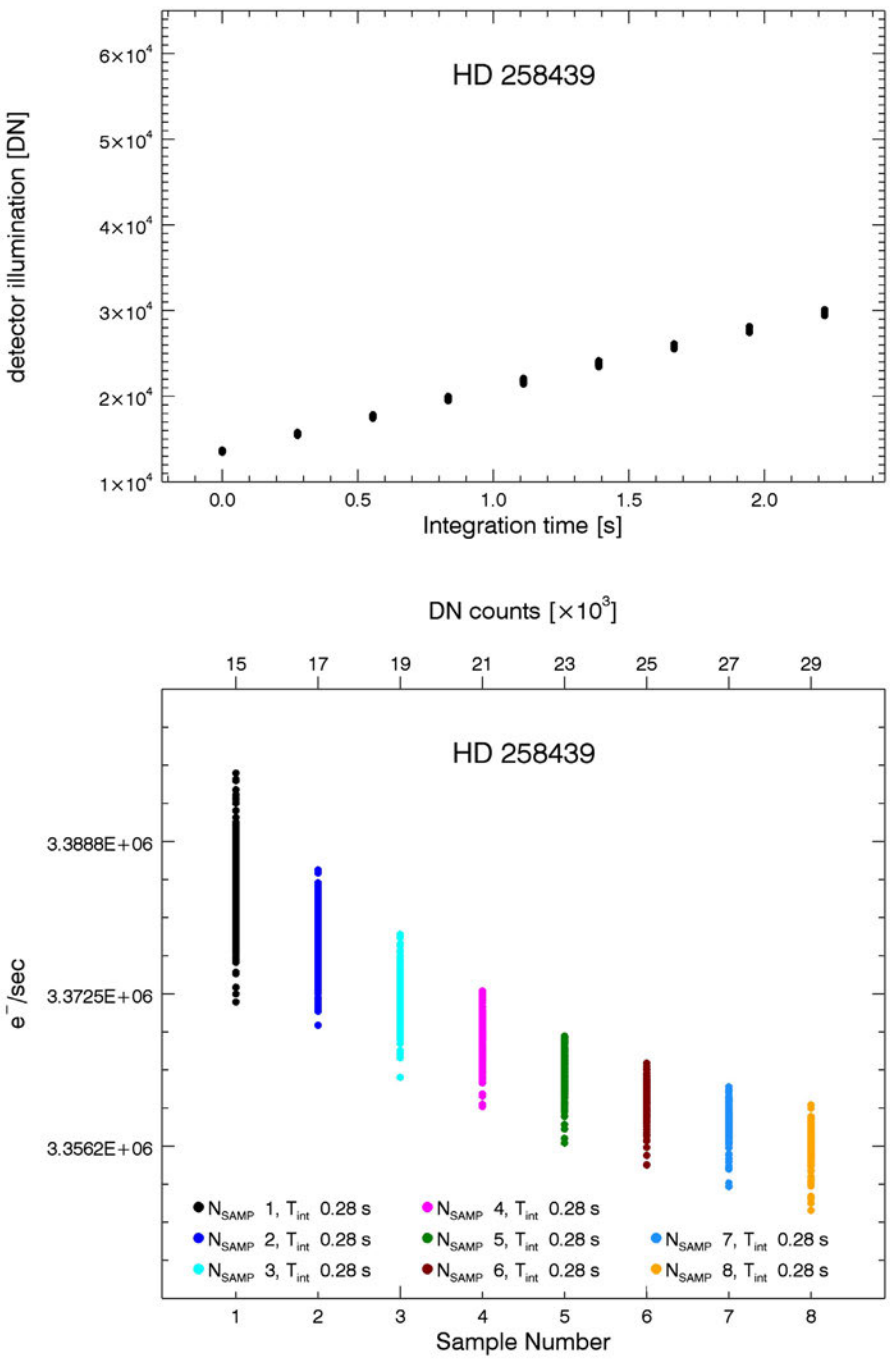
HD 258439
detector illumination [DN]
6×10^4
5×10^4
4×10^4
3×10^4
2×10^4
1×10^4
0.0
0.5
1.0
1.5
2.0
Integration time [s]
DN counts [×10^3]
15
17
19
21
23
25
27
29
HD 258439
e⁻/sec
3.3888E+06
3.3725E+06
3.3562E+06
N_SAMP 1, T_int 0.28 s
N_SAMP 2, T_int 0.28 s
N_SAMP 3, T_int 0.28 s
N_SAMP 4, T_int 0.28 s
N_SAMP 5, T_int 0.28 s
N_SAMP 6, T_int 0.28 s
N_SAMP 7, T_int 0.28 s
N_SAMP 8, T_int 0.28 s
1
2
3
4
5
6
7
8
Sample Number

Figure 13.1-7.

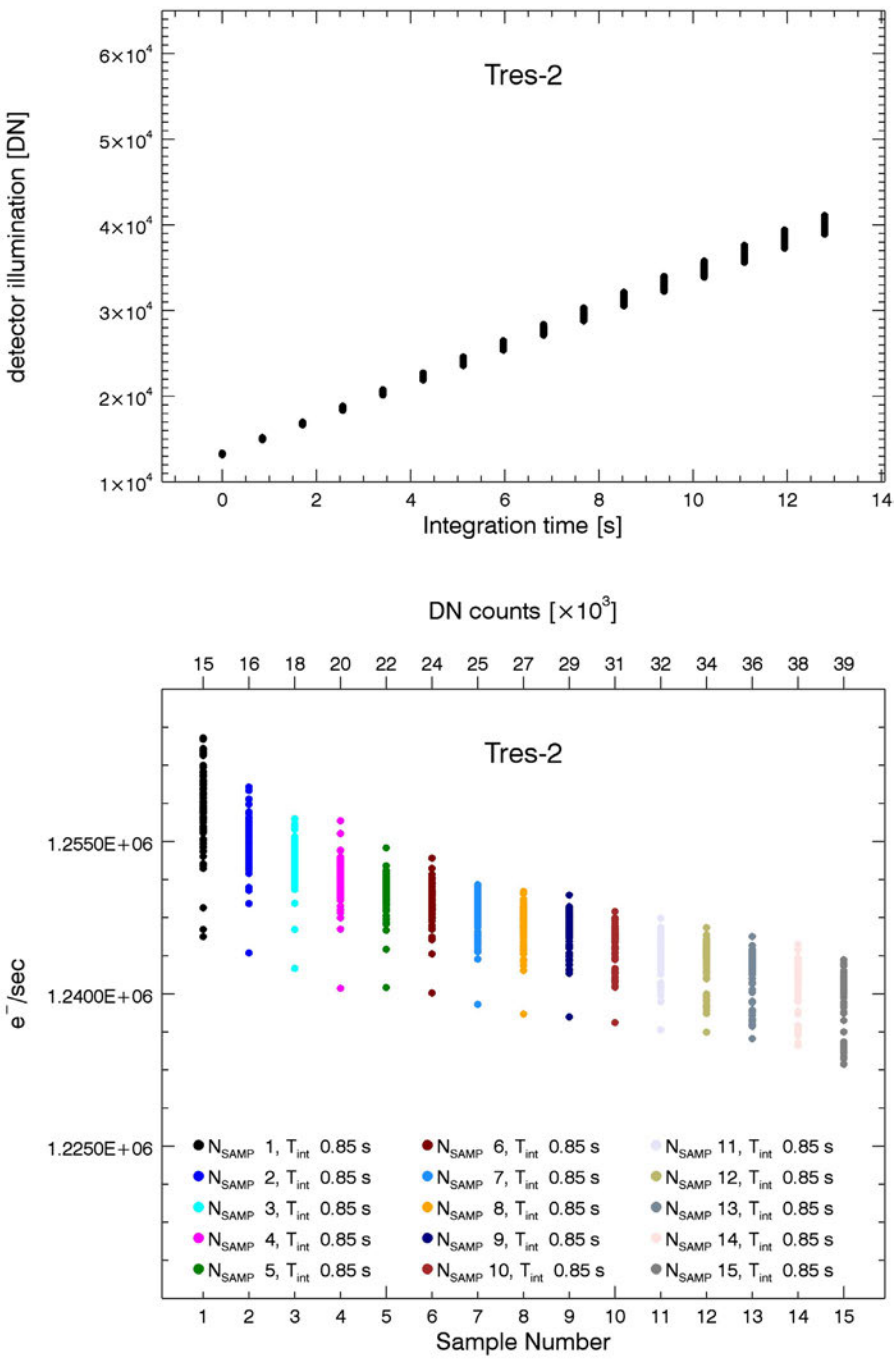
Tres-2
detector illumination [DN]
Integration time [s]
DN counts [×10^3]
Tres-2
e⁻/sec
Sample Number
N_SAMP 1, T_int 0.85 s
N_SAMP 2, T_int 0.85 s
N_SAMP 3, T_int 0.85 s
N_SAMP 4, T_int 0.85 s
N_SAMP 5, T_int 0.85 s
N_SAMP 6, T_int 0.85 s
N_SAMP 7, T_int 0.85 s
N_SAMP 8, T_int 0.85 s
N_SAMP 9, T_int 0.85 s
N_SAMP 10, T_int 0.85 s
N_SAMP 11, T_int 0.85 s
N_SAMP 12, T_int 0.85 s
N_SAMP 13, T_int 0.85 s
N_SAMP 14, T_int 0.85 s
N_SAMP 15, T_int 0.85 s

Figure 13.1-8.

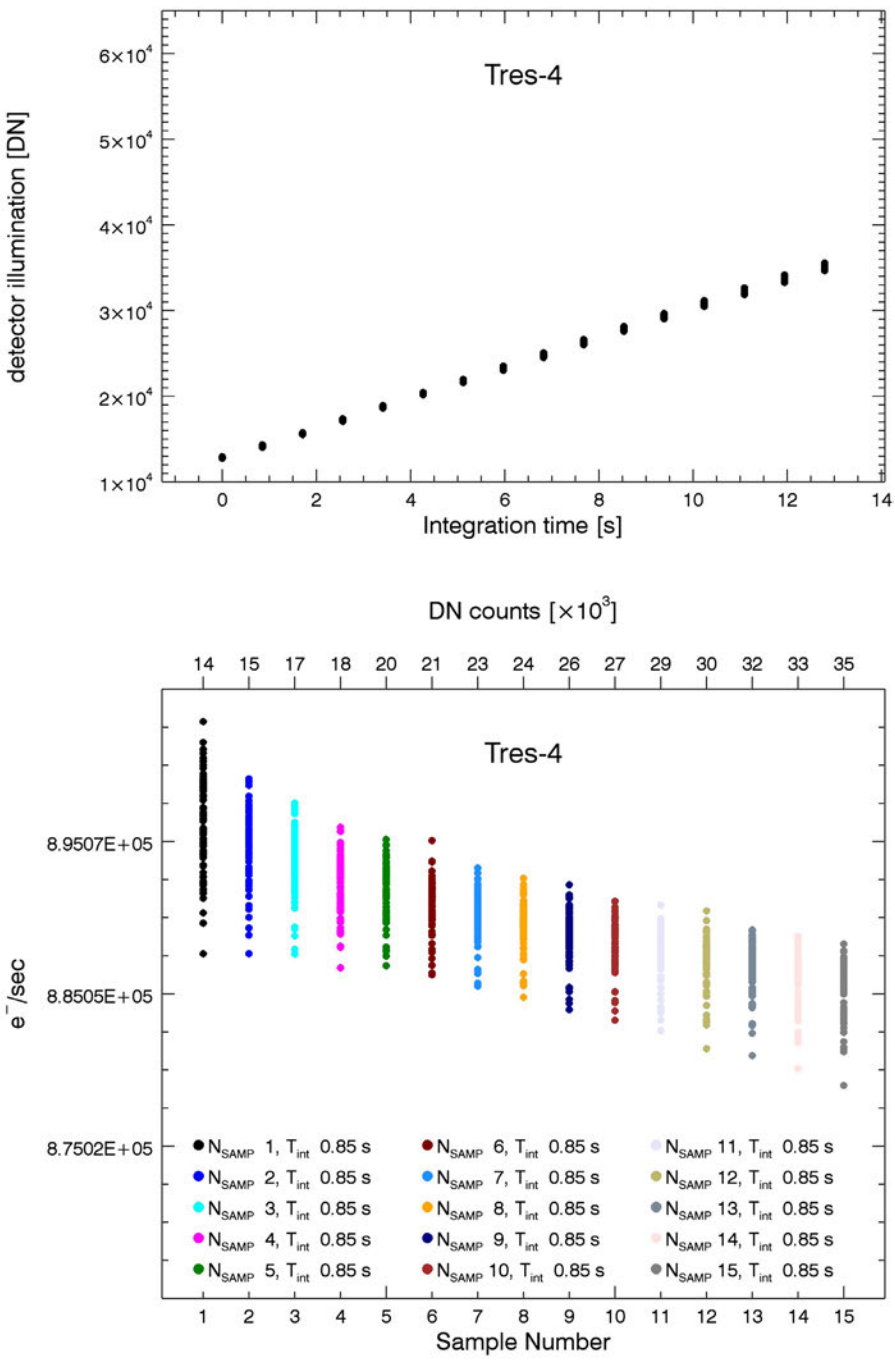
Tres-4
detector illumination [DN]
Integration time [s]
DN counts [×10^3]
Tres-4
e⁻/sec
Sample Number
N_SAMP 1, T_int 0.85 s
N_SAMP 2, T_int 0.85 s
N_SAMP 3, T_int 0.85 s
N_SAMP 4, T_int 0.85 s
N_SAMP 5, T_int 0.85 s
N_SAMP 6, T_int 0.85 s
N_SAMP 7, T_int 0.85 s
N_SAMP 8, T_int 0.85 s
N_SAMP 9, T_int 0.85 s
N_SAMP 10, T_int 0.85 s
N_SAMP 11, T_int 0.85 s
N_SAMP 12, T_int 0.85 s
N_SAMP 13, T_int 0.85 s
N_SAMP 14, T_int 0.85 s
N_SAMP 15, T_int 0.85 s

Figure 13.1-9.

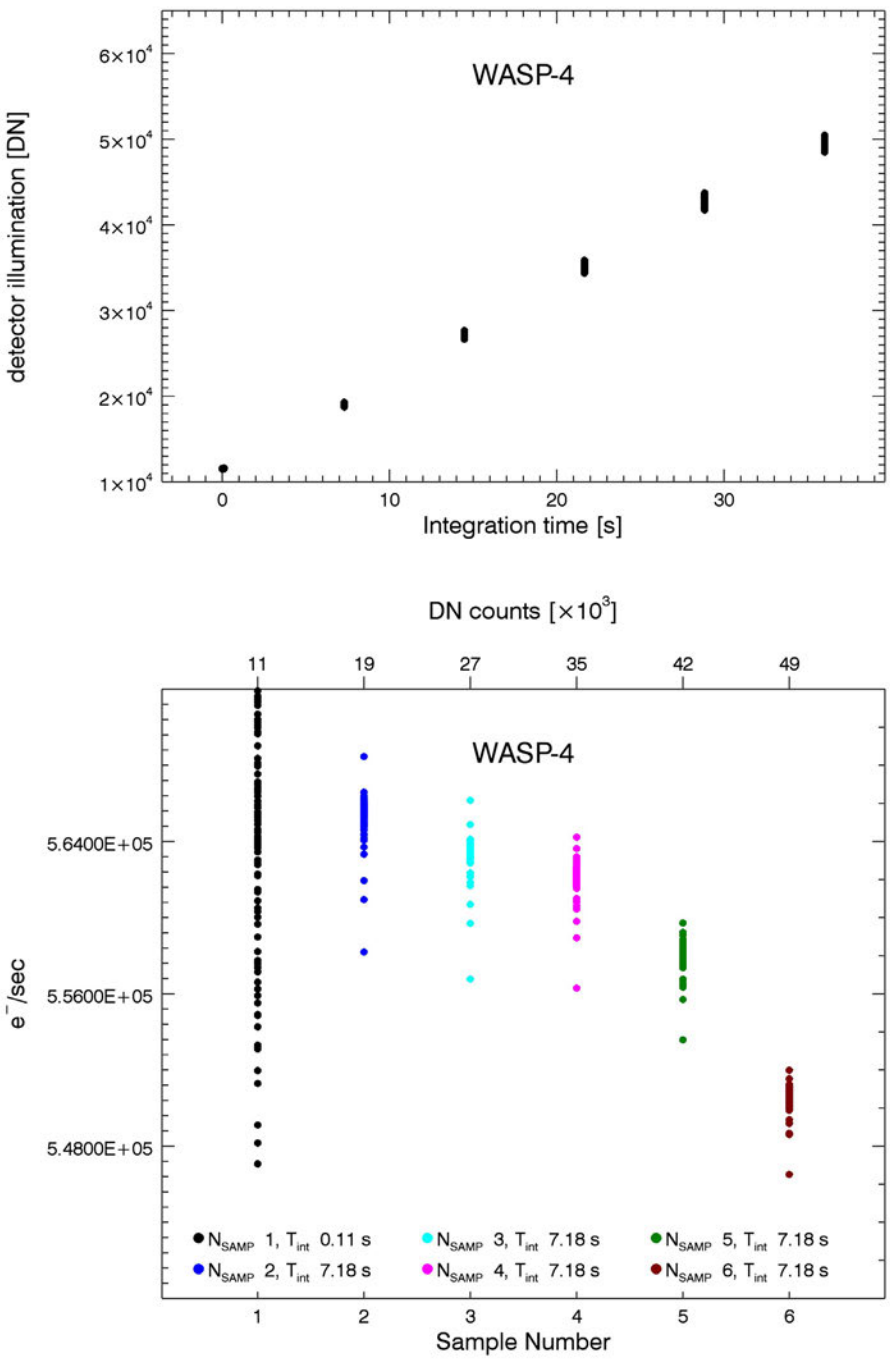

Figure 13.1-10.

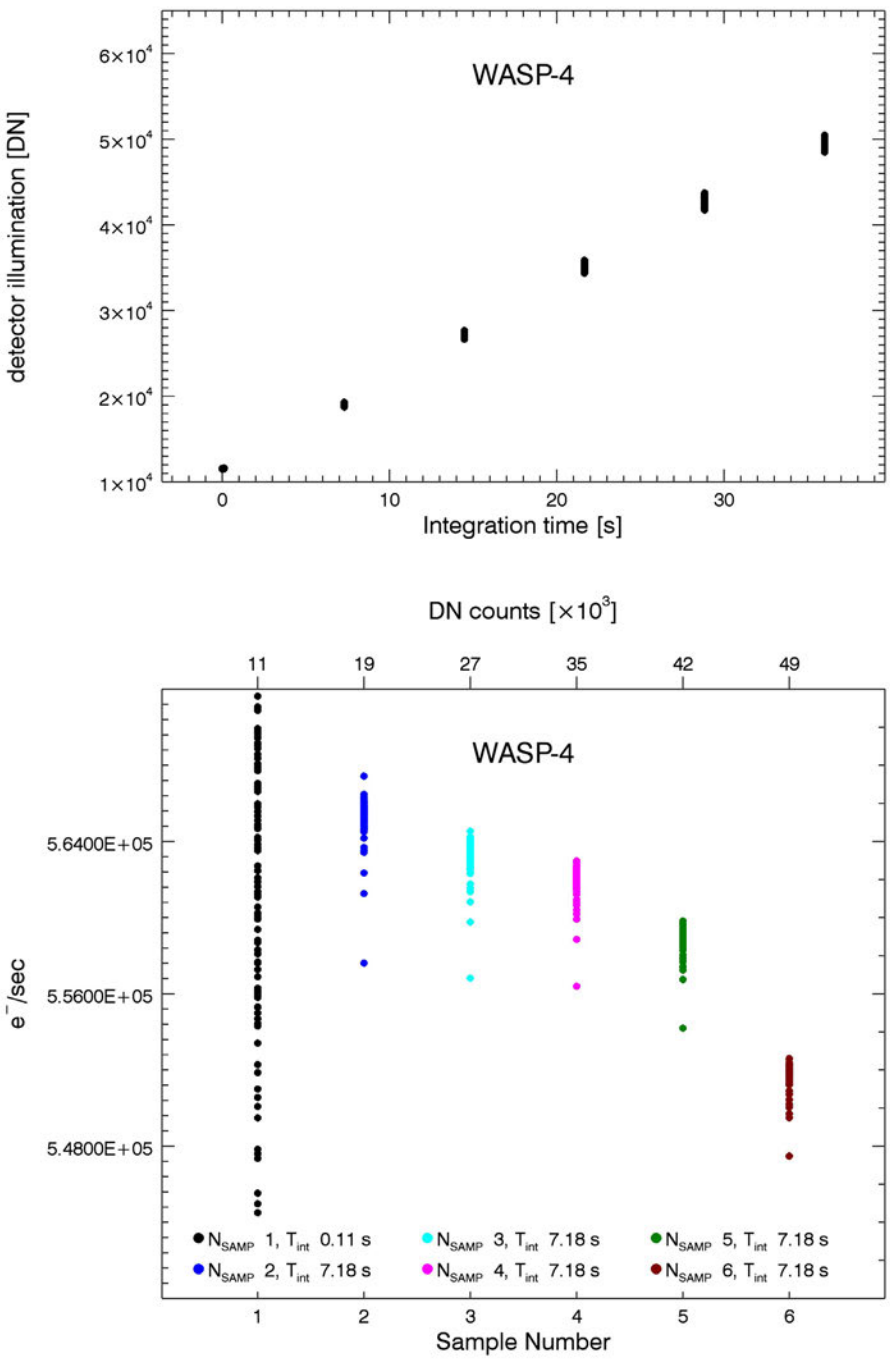

Figure 13.1-11.

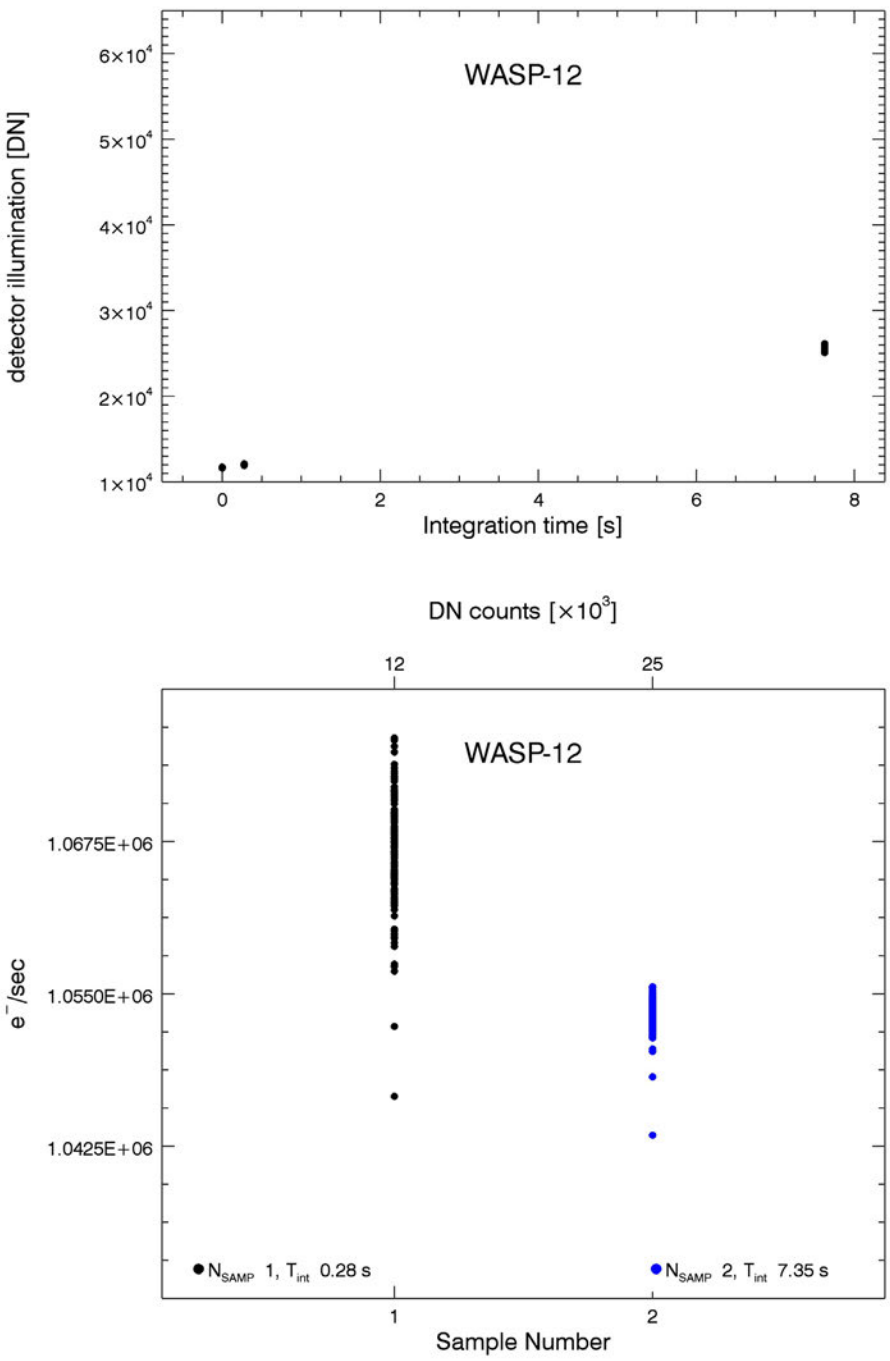

Figure 13.1-12.

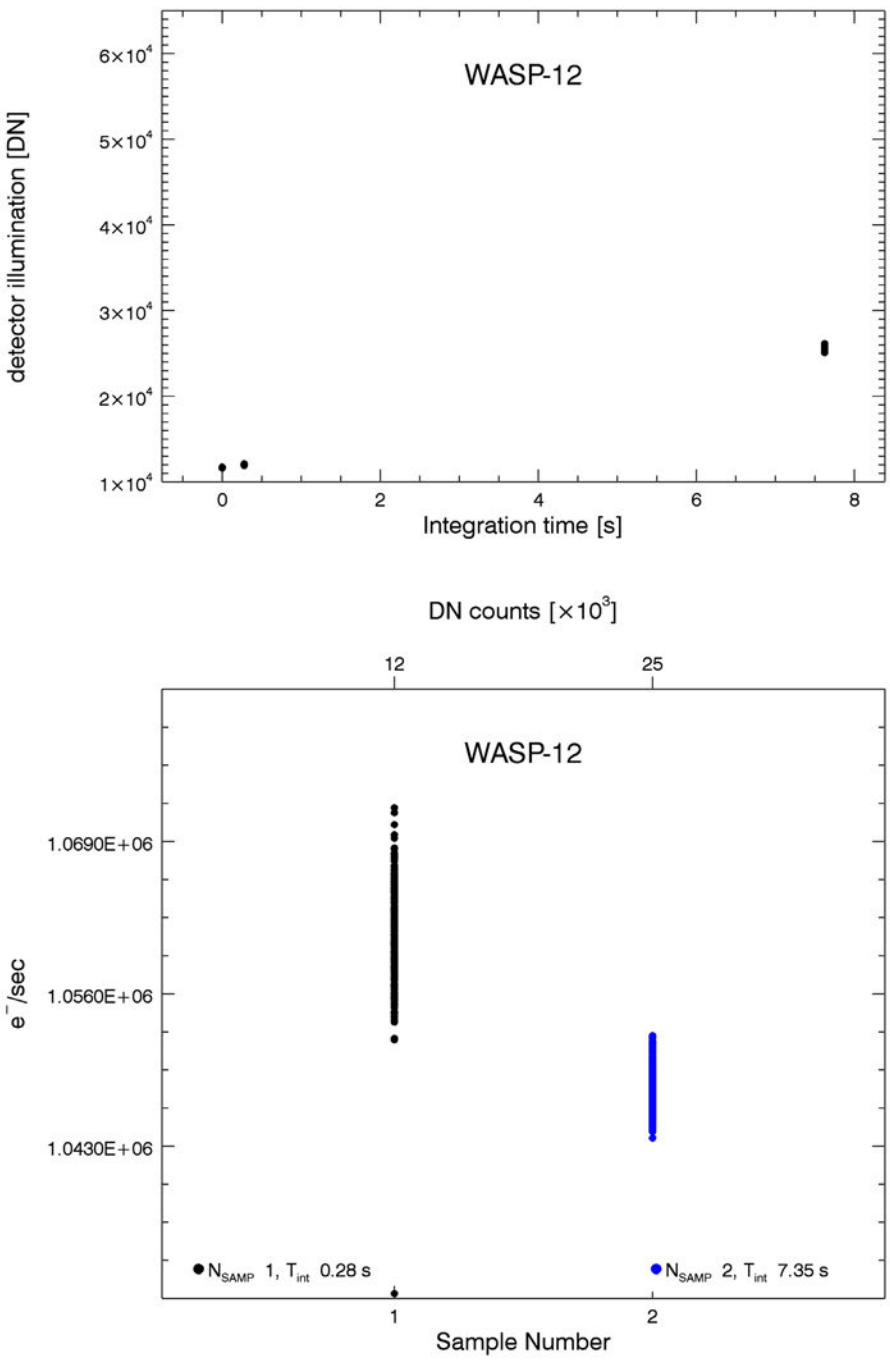

Figure 13.1-13.

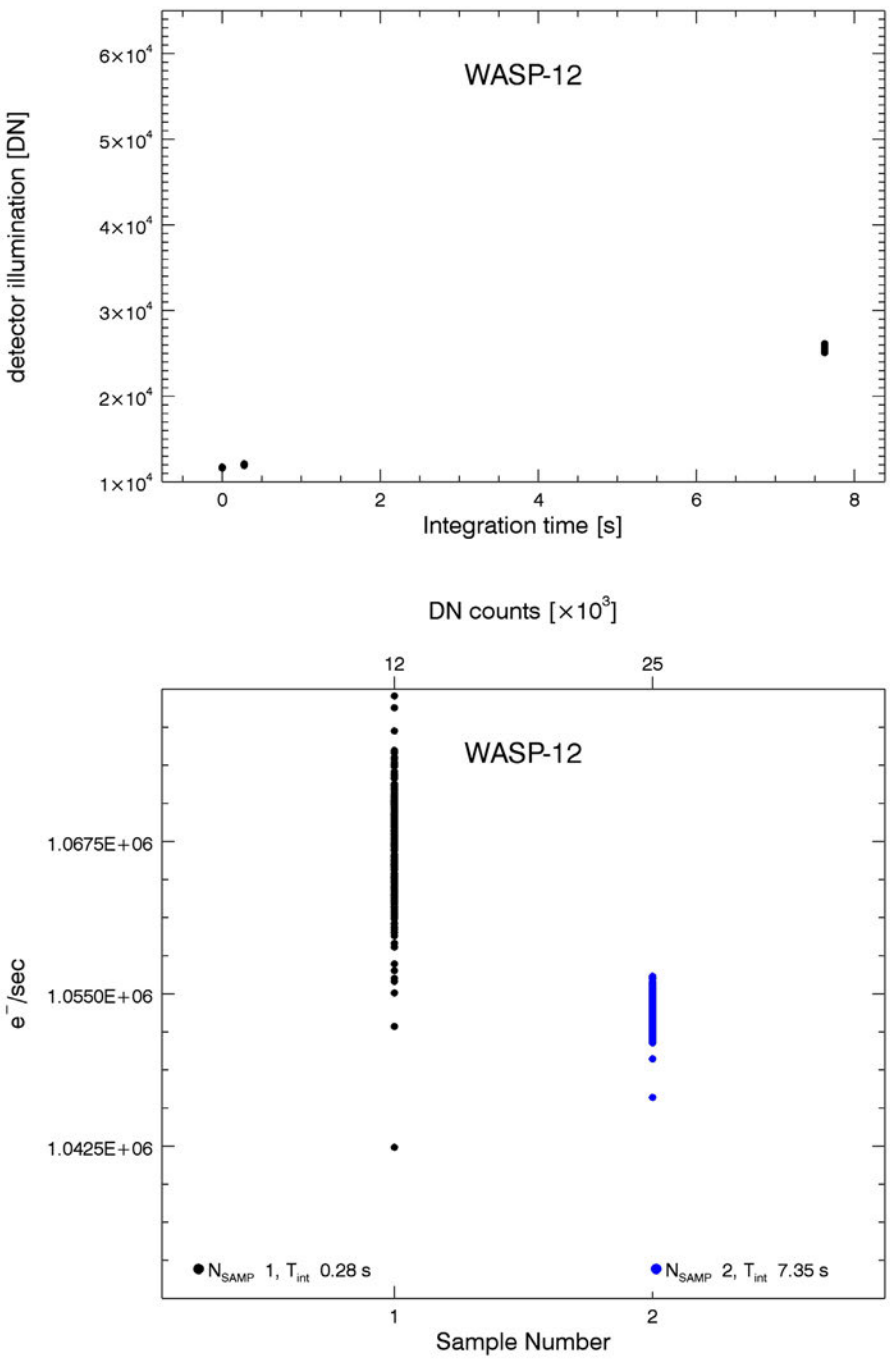

Figure 13.1-14.

1.4 Optical State Effects – Time Domain

For measuring the impact of the changes in the instrument optical state on the measurement, we compared optical state parameters to the measured flux (see Figures 1.4-1 to 1.4-14). These diagnostics were all based on _flt data and are implemented as described in the main paper and references therein. We found that at the ~150 ppm level, corresponding to the WASP-12b spectral measurements reported in the main paper,

decorrelation based on these parameters does not materially improve the stability of the time series. For the WASP-12b broadband light curve, which has a theoretical sensitivity limit of ~56 ppm, changes in the instrument start to have an influence on the measurements.

1. **Broadband flux:** This diagnostic is identical to that used in 1.1 and it is shown in the top panel of the Figure 1.4-1 to 1.4-14 series.
2. **Translation changes:** This observable is defined as the average of the cross-axis position of the spectrum on the detector measured at every pixel. The uncertainty is the uncertainty in the fit parameter and corresponds to the standard deviation of the individual pixel measurements with respect to the mean. The results for this observable for each observation are shown in the second (from the top) panel in the Figure 1.4-1 to 1.4-14 series.
3. **Rotation changes:** The diagnostic for rotation changes is defined as slope change to a linear fit to the trace of the spectrum. Uncertainties are determined as in (2). The results for this diagnostic for each observation are shown in the third (from the top) panel in the Figure 1.4-1 to 1.4-14 series.
4. **Focus changes:** The diagnostic for focus is estimated from the average of the full width half max of a Gaussian fit to the spectrum in the cross axis direction for each pixel-based spectral channel. The uncertainties are determined as in (2). Results for this diagnostic for each observation are shown in the bottom panel in the Figure 1.4-1 to 1.4-14 series.

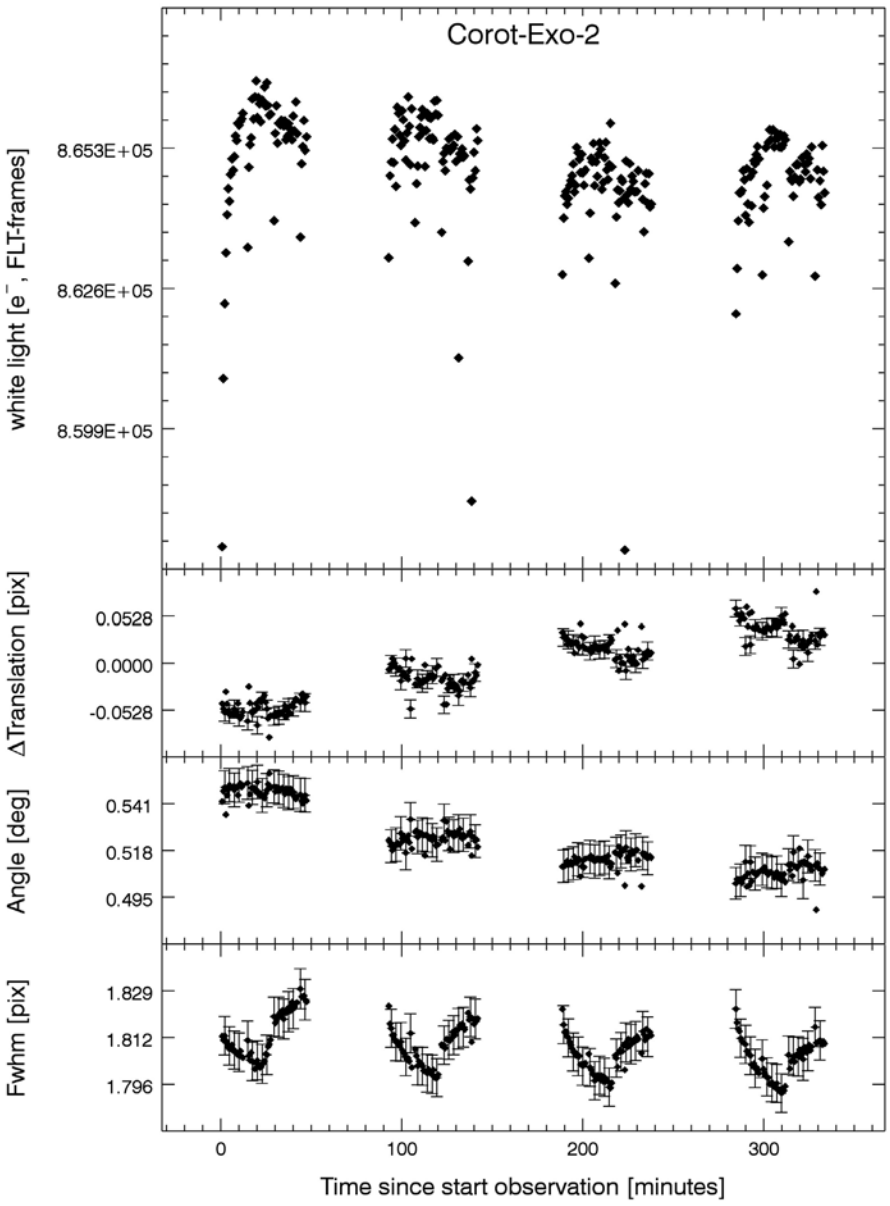
Corot-Exo-2
white light [e⁻, FLT-frames]
8.653E+05
8.626E+05
8.599E+05
ΔTranslation [pix]
0.0528
0.0000
-0.0528
Angle [deg]
0.541
0.518
0.495
Fwhm [pix]
1.829
1.812
1.796
0
100
200
300
Time since start observation [minutes]

Figure 14.1-1.

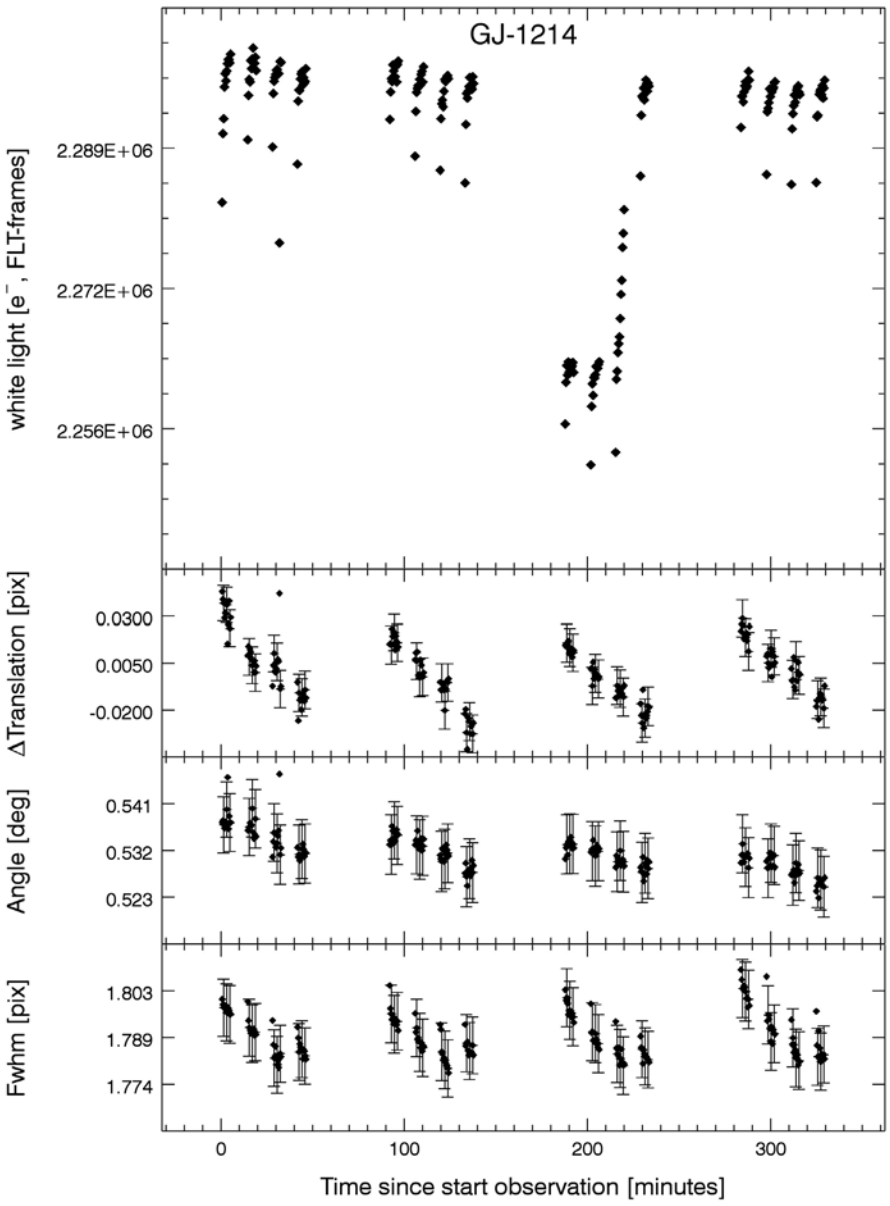
GJ-1214
white light [e⁻, FLT-frames]
2.289E+06
2.272E+06
2.256E+06
ΔTranslation [pix]
0.0300
0.0050
-0.0200
Angle [deg]
0.541
0.532
0.523
Fwhm [pix]
1.803
1.789
1.774
0
100
200
300
Time since start observation [minutes]

Figure 14.1-2.

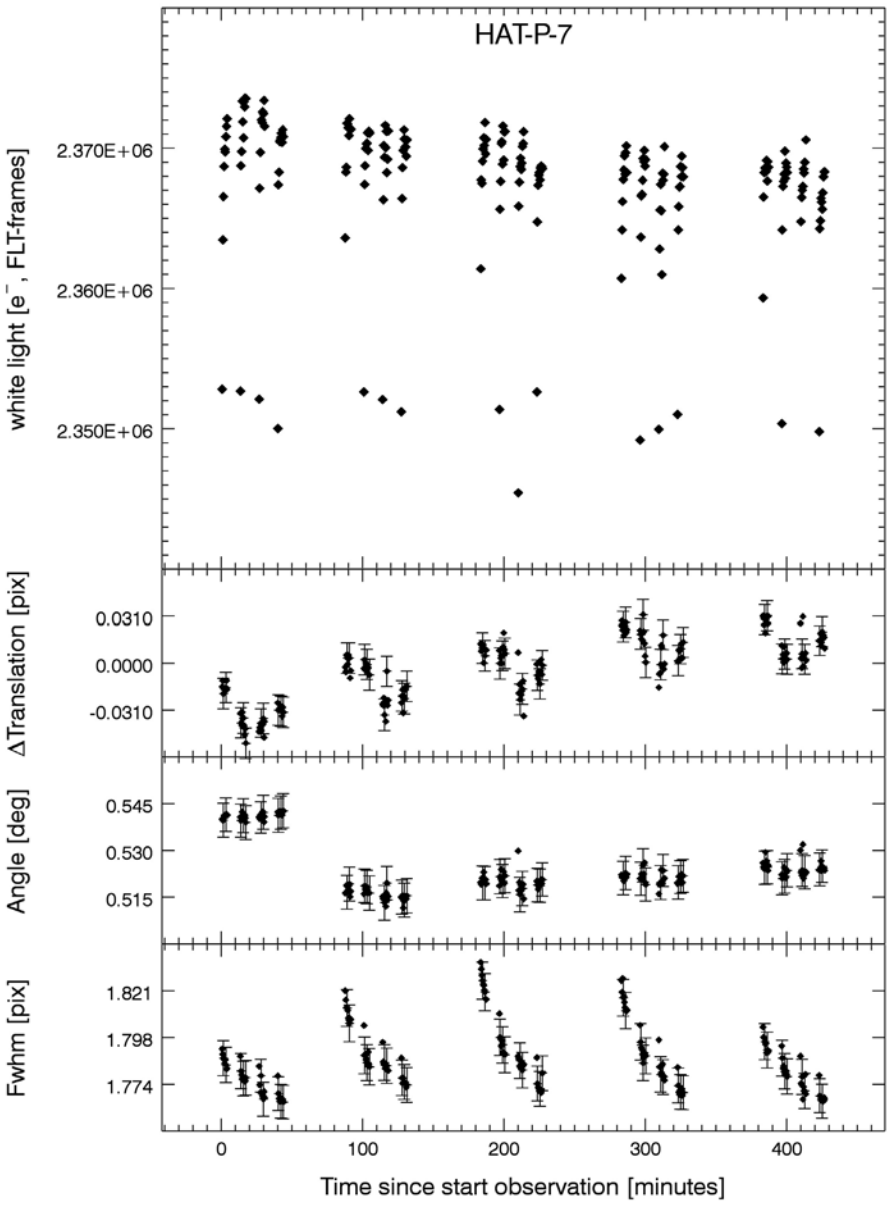
HAT-P-7
white light [e⁻, FLT-frames]
2.370E+06
2.360E+06
2.350E+06
ΔTranslation [pix]
0.0310
0.0000
-0.0310
Angle [deg]
0.545
0.530
0.515
Fwhm [pix]
1.821
1.798
1.774
0
100
200
300
400
Time since start observation [minutes]

Figure 14.1-3.

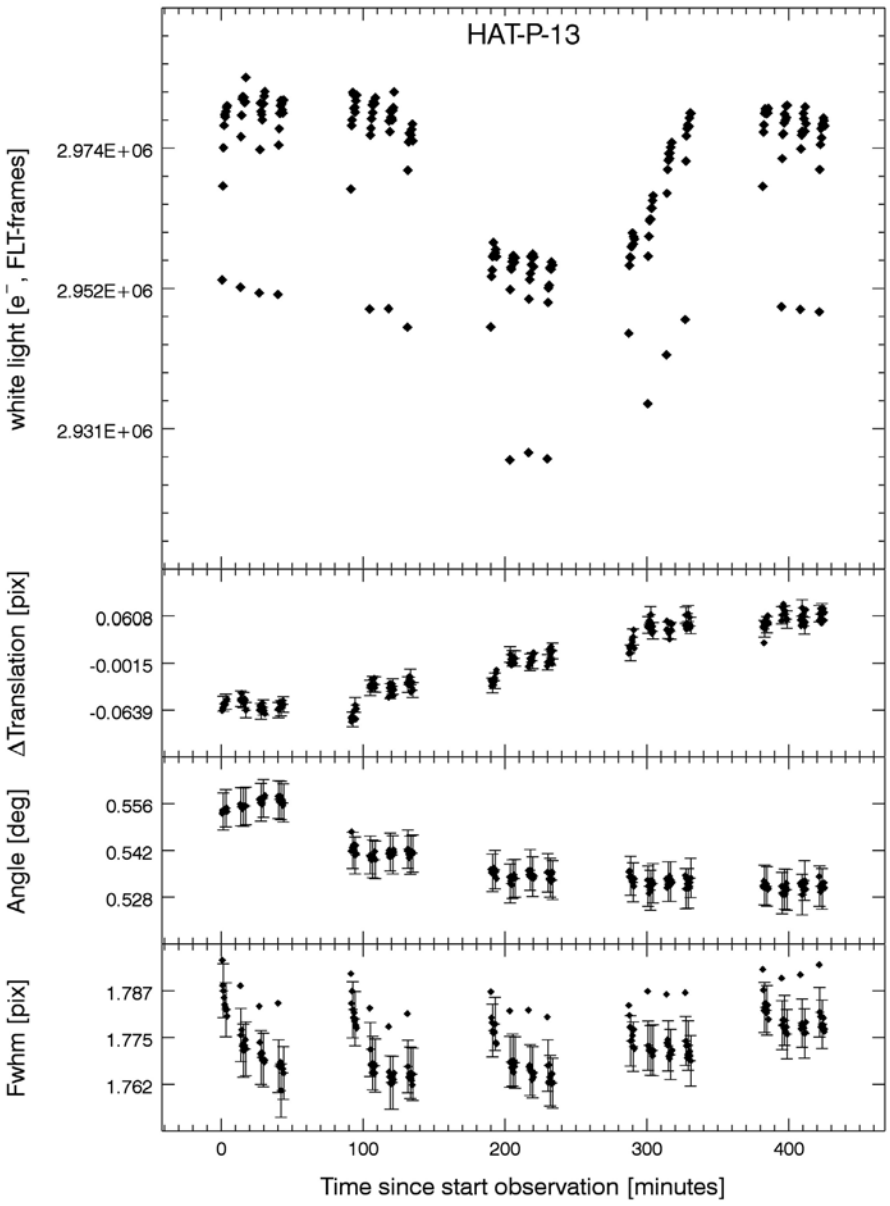
HAT-P-13
white light [e⁻, FLT-frames]
2.974E+06
2.952E+06
2.931E+06
ΔTranslation [pix]
0.0608
-0.0015
-0.0639
Angle [deg]
0.556
0.542
0.528
Fwhm [pix]
1.787
1.775
1.762
0
100
200
300
400
Time since start observation [minutes]

Figure 14.1-4.

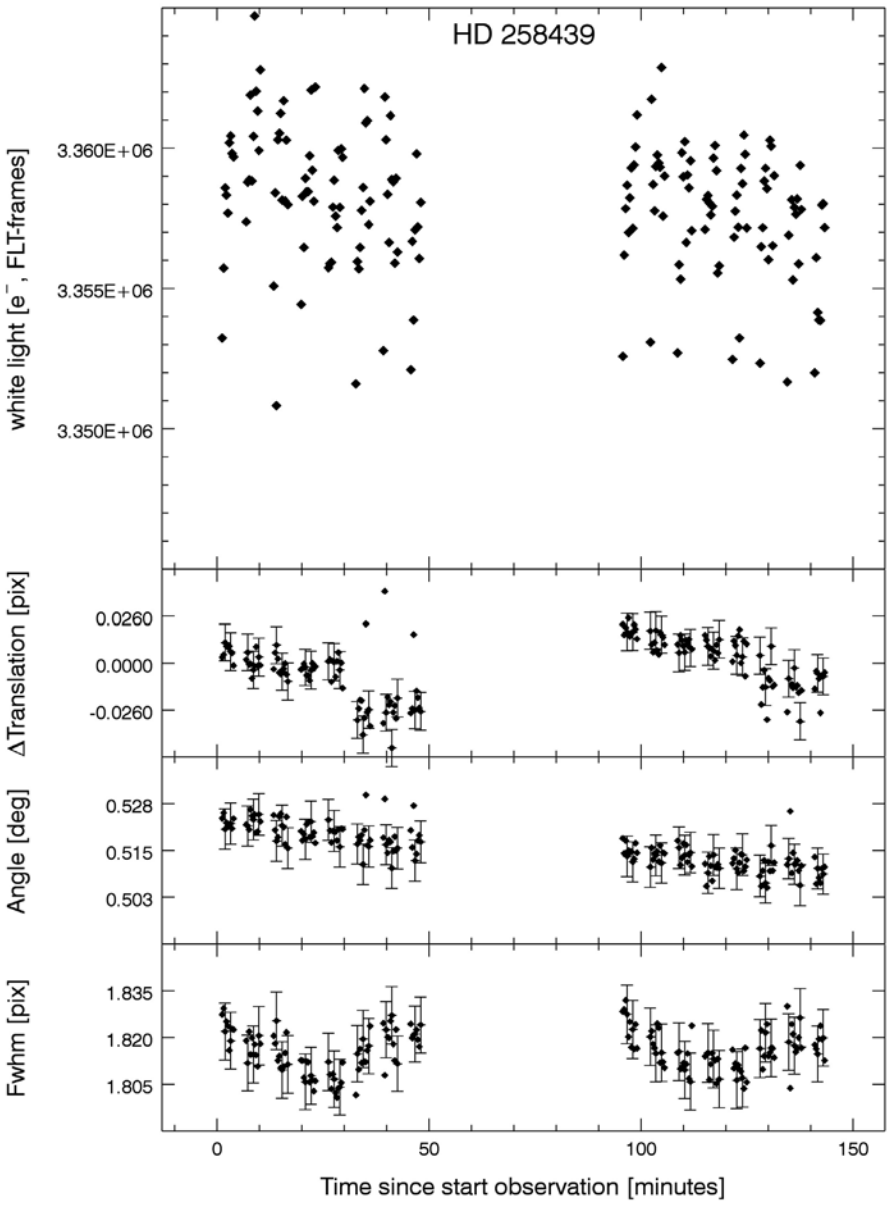
HD 258439
white light [e⁻, FLT-frames]
3.360E+06
3.355E+06
3.350E+06
ΔTranslation [pix]
0.0260
0.0000
-0.0260
Angle [deg]
0.528
0.515
0.503
Fwhm [pix]
1.835
1.820
1.805
0
50
100
150
Time since start observation [minutes]

Figure 14.1-5.

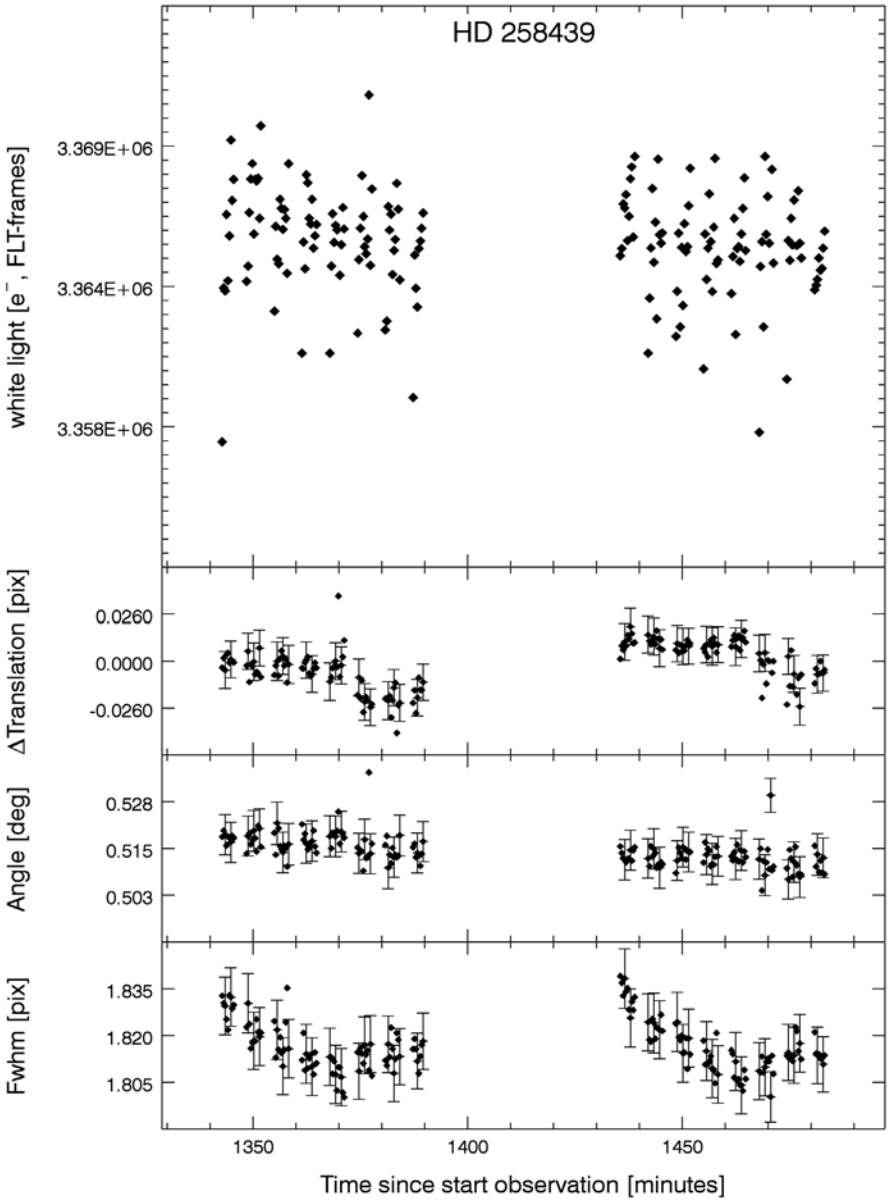
HD 258439
white light [e⁻, FLT-frames]
3.369E+06
3.364E+06
3.358E+06
ΔTranslation [pix]
0.0260
0.0000
-0.0260
Angle [deg]
0.528
0.515
0.503
Fwhm [pix]
1.835
1.820
1.805
1350
1400
1450
Time since start observation [minutes]

Figure 14.1-6.

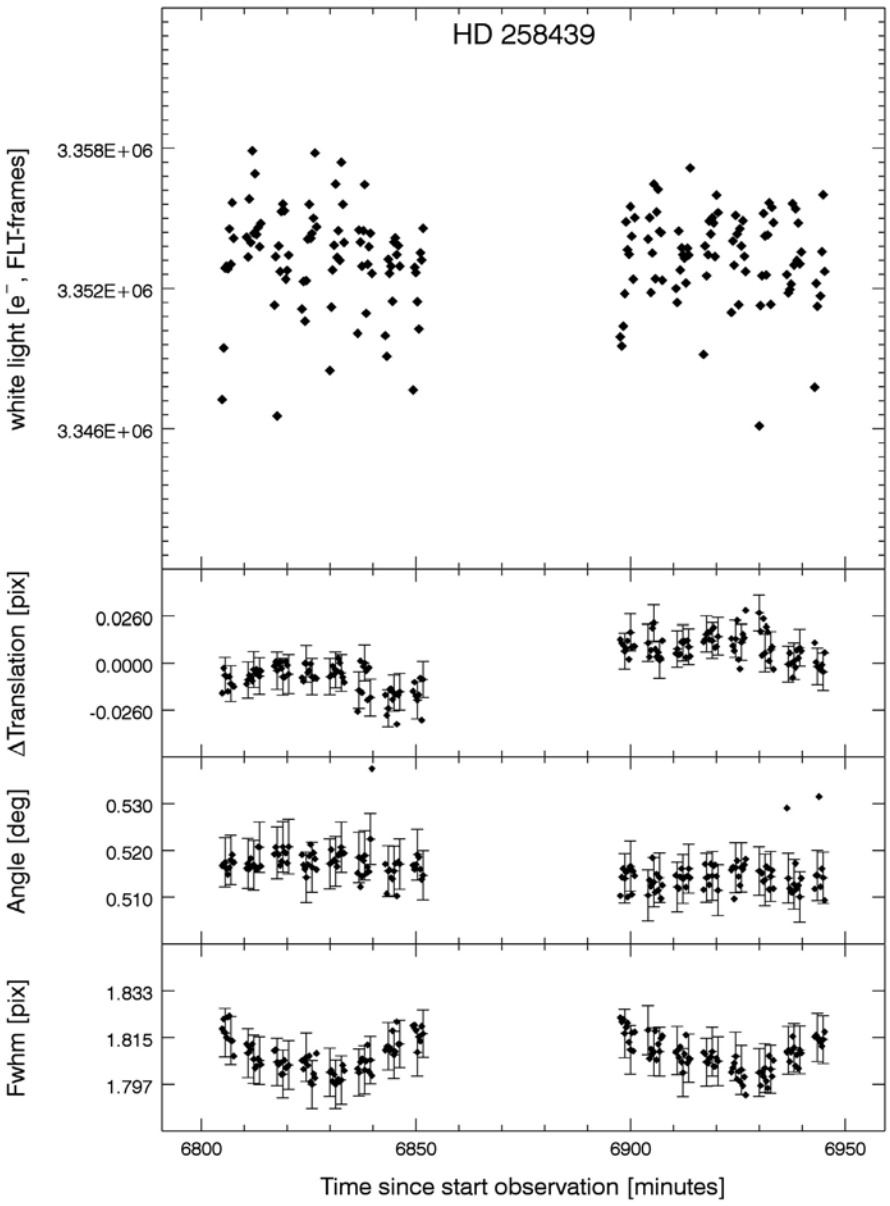
HD 258439
white light [e⁻, FLT-frames]
3.358E+06
3.352E+06
3.346E+06
ΔTranslation [pix]
0.0260
0.0000
-0.0260
Angle [deg]
0.530
0.520
0.510
Fwhm [pix]
1.833
1.815
1.797
6800
6850
6900
6950
Time since start observation [minutes]

Figure 14.1-7.

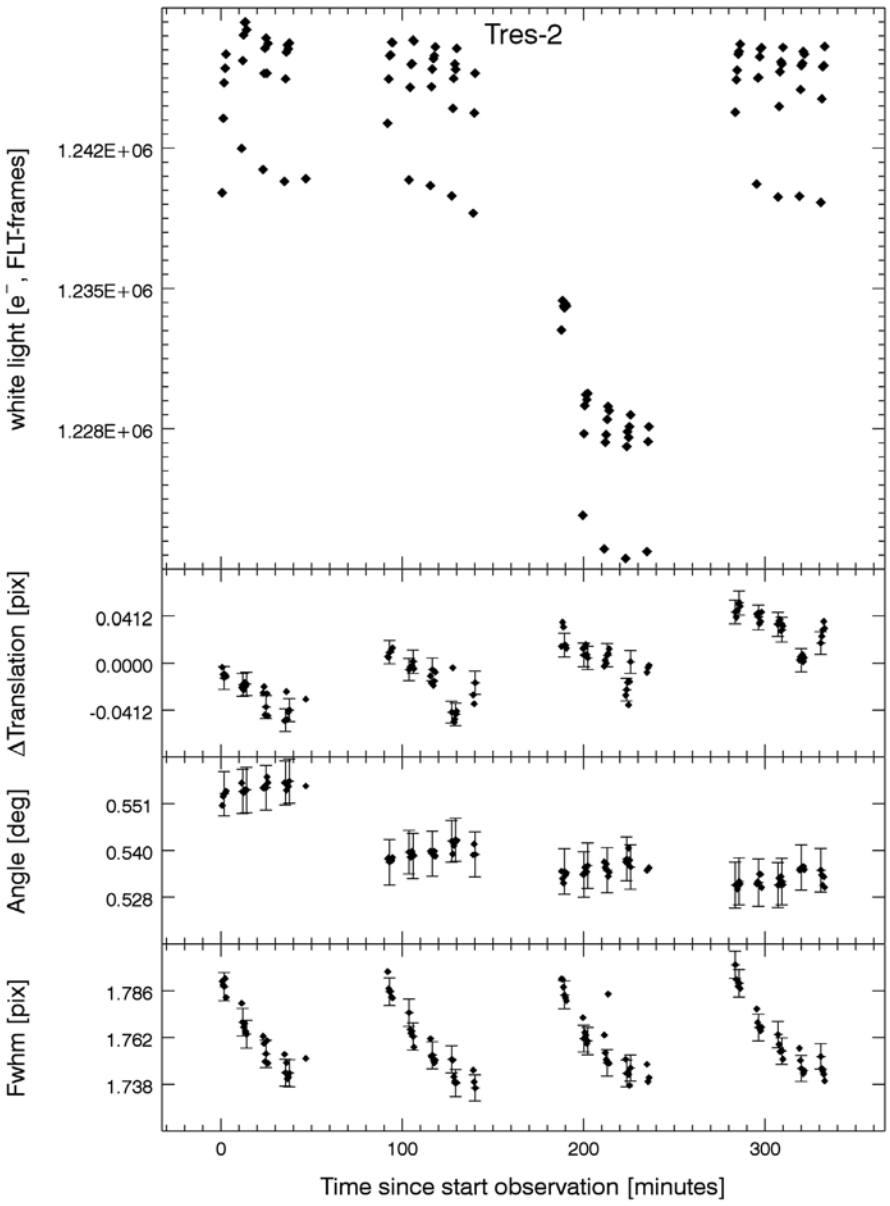
Tres-2
white light [e⁻, FLT-frames]
1.242E+06
1.235E+06
1.228E+06
ΔTranslation [pix]
0.0412
0.0000
-0.0412
Angle [deg]
0.551
0.540
0.528
Fwhm [pix]
1.786
1.762
1.738
0
100
200
300
Time since start observation [minutes]

Figure 14.1-8.

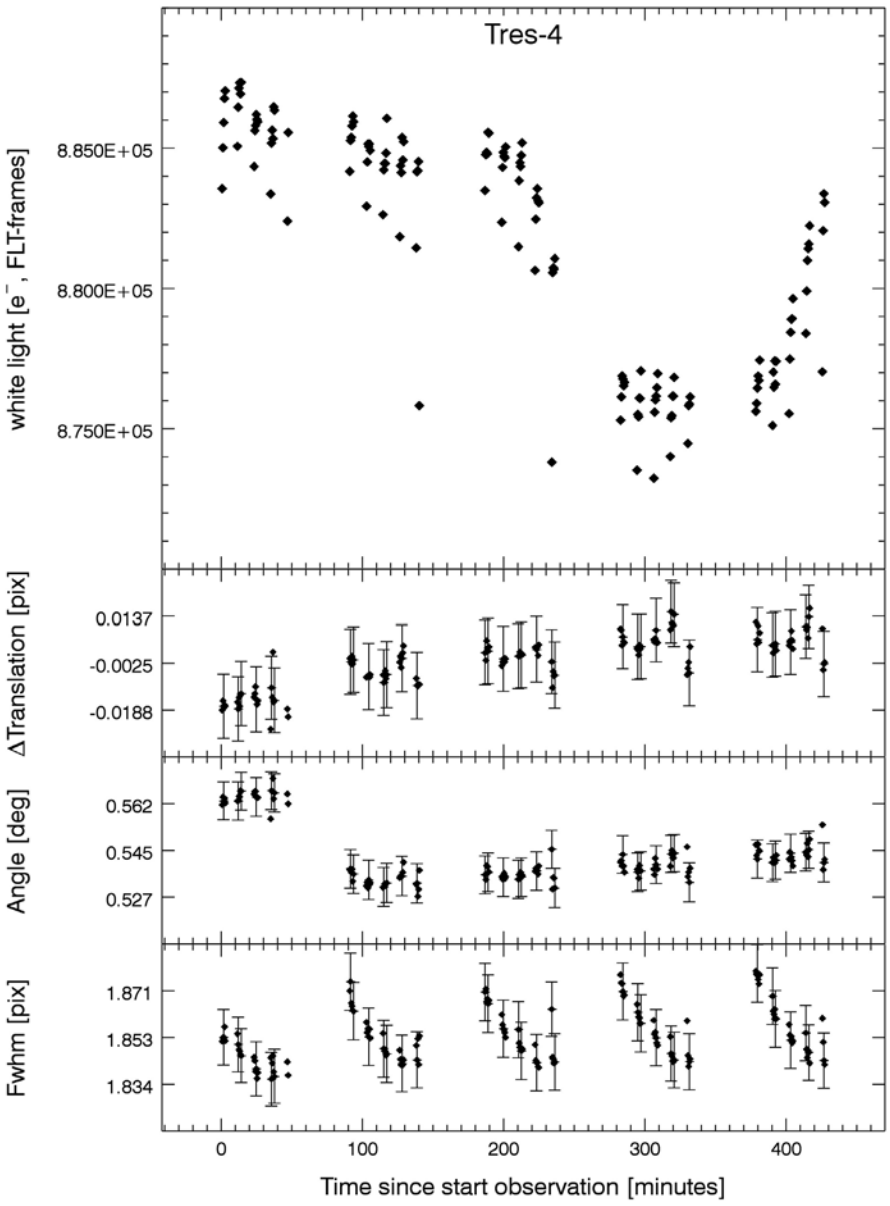
Tres-4
white light [e⁻, FLT-frames]
8.850E+05
8.800E+05
8.750E+05
ΔTranslation [pix]
0.0137
-0.0025
-0.0188
Angle [deg]
0.562
0.545
0.527
Fwhm [pix]
1.871
1.853
1.834
0
100
200
300
400
Time since start observation [minutes]

Figure 14.1-9.

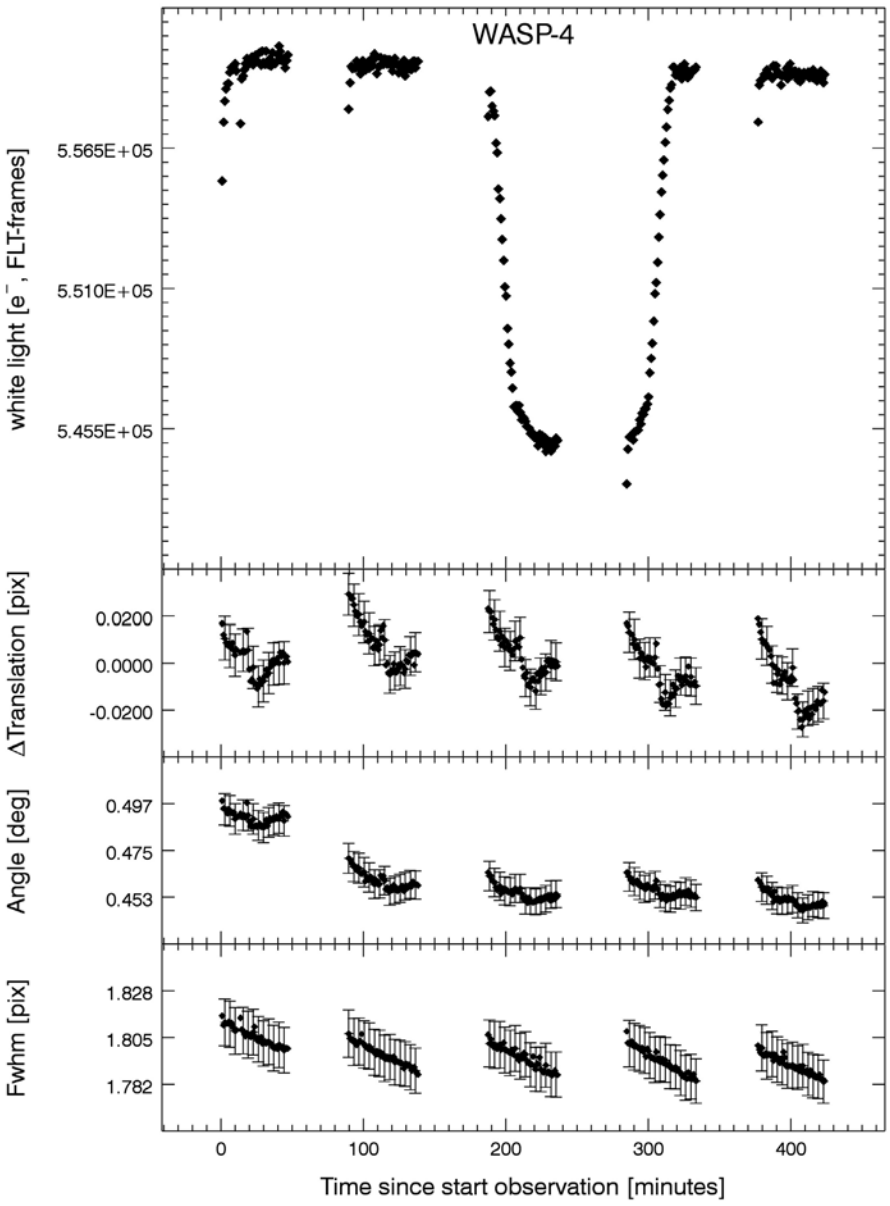

Figure 14.1-10.

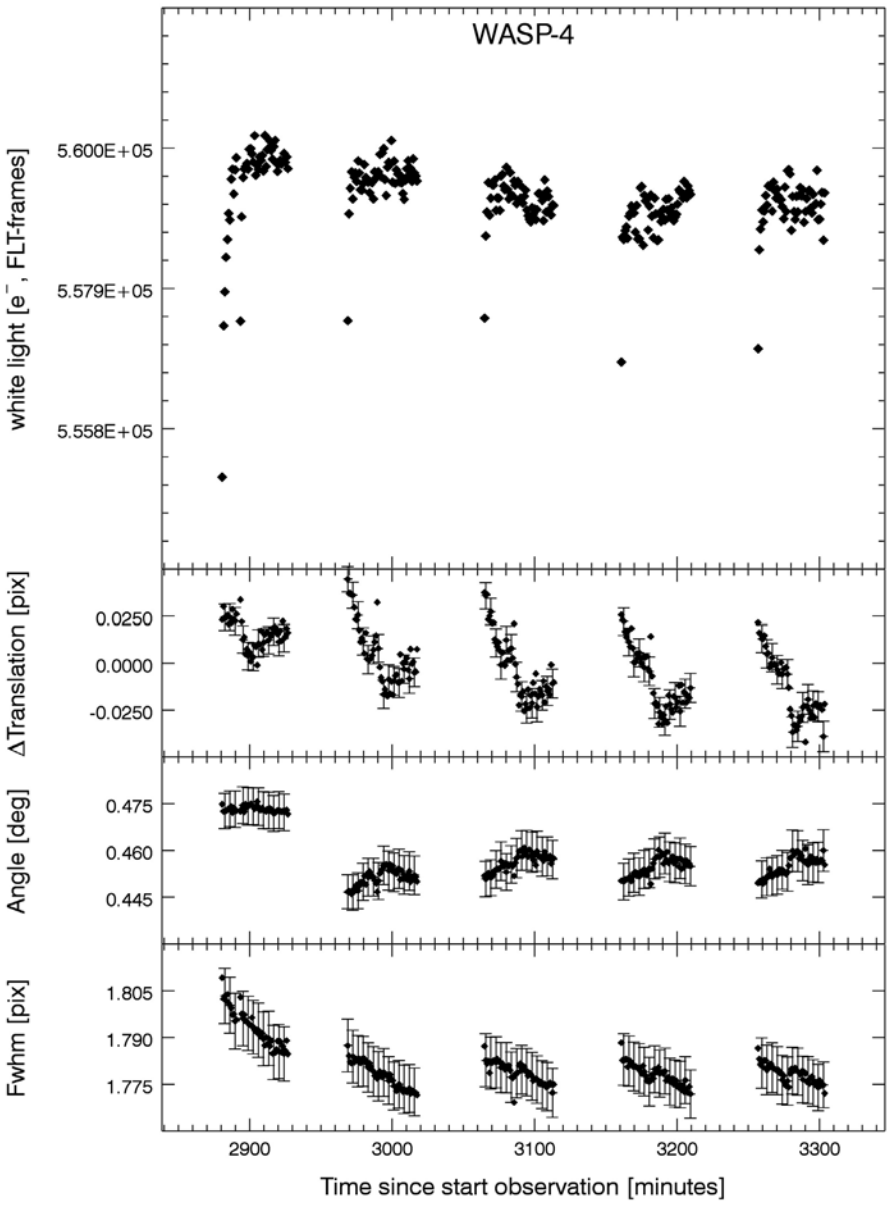

Figure 14.1-11.

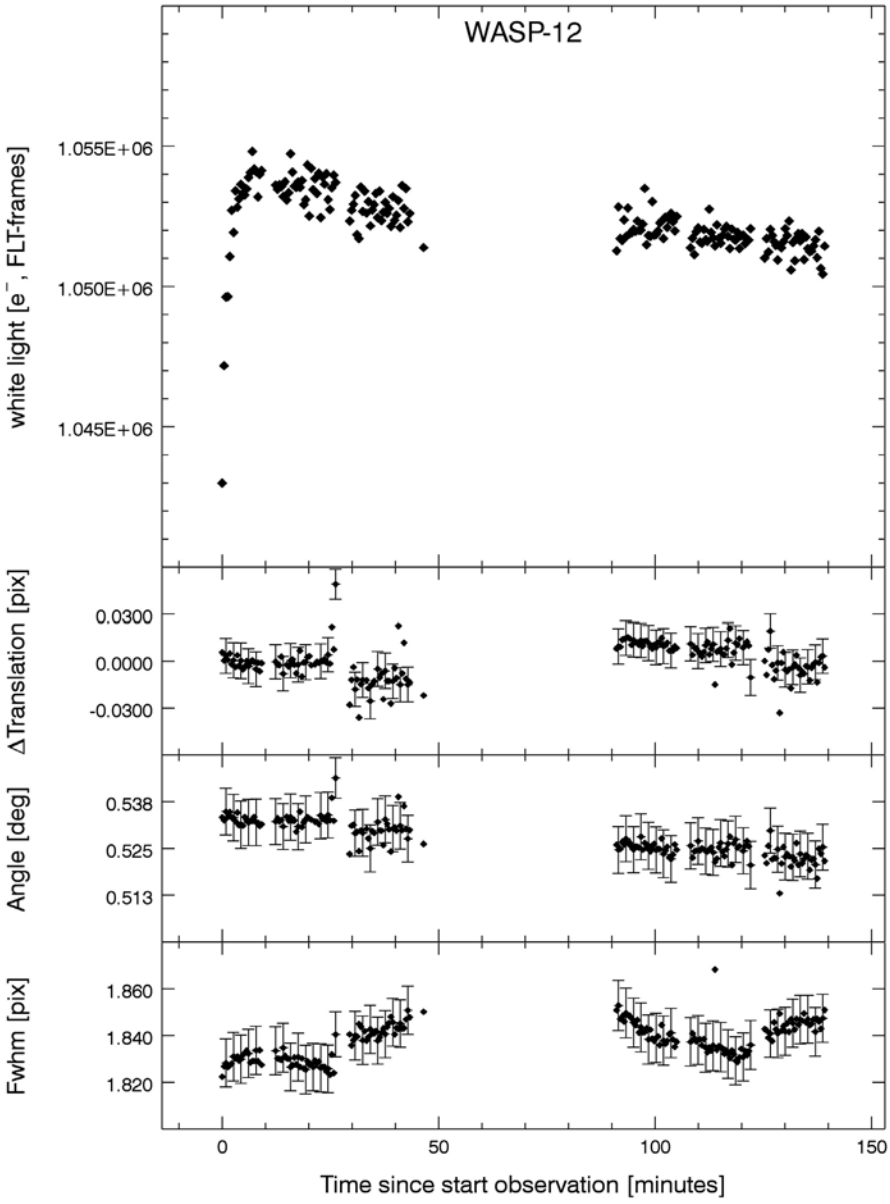

Figure 14.1-12.

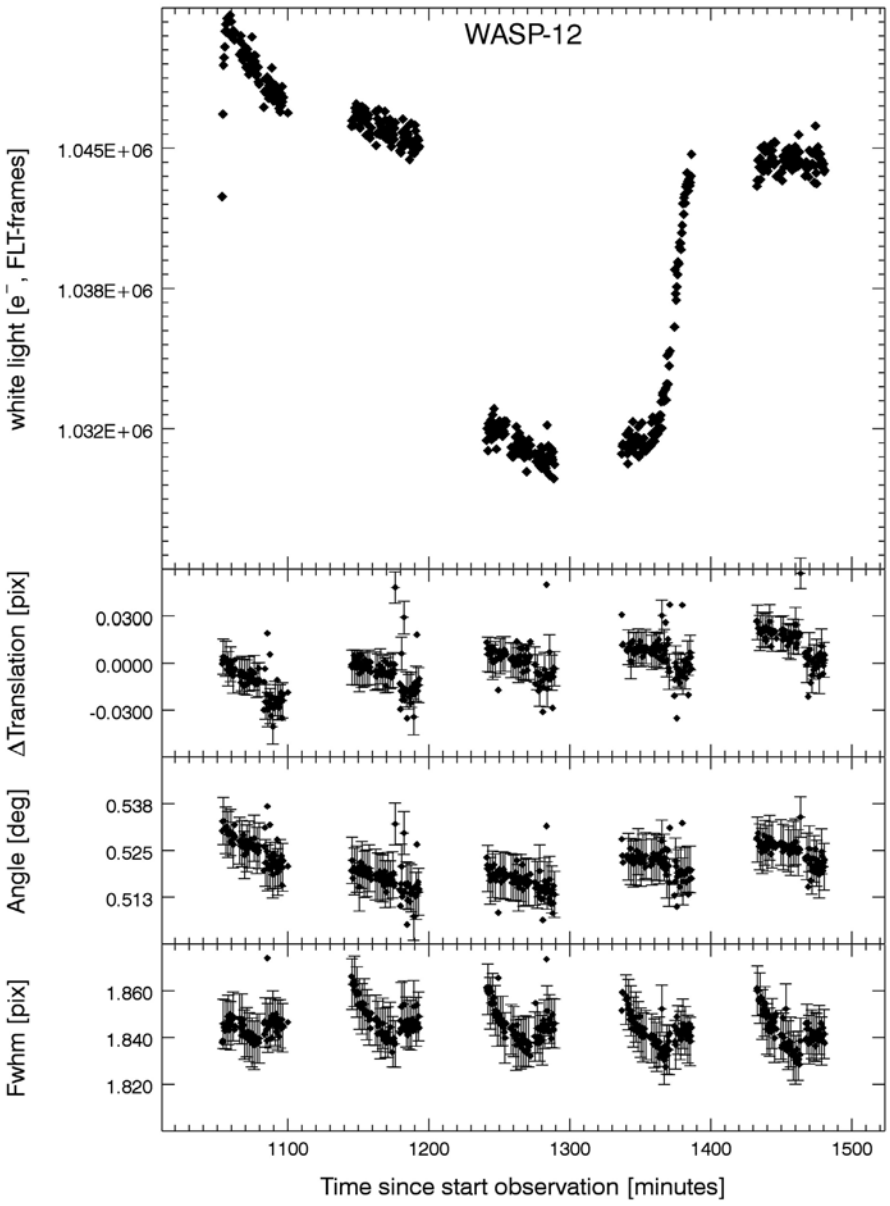

Figure 14.1-13.

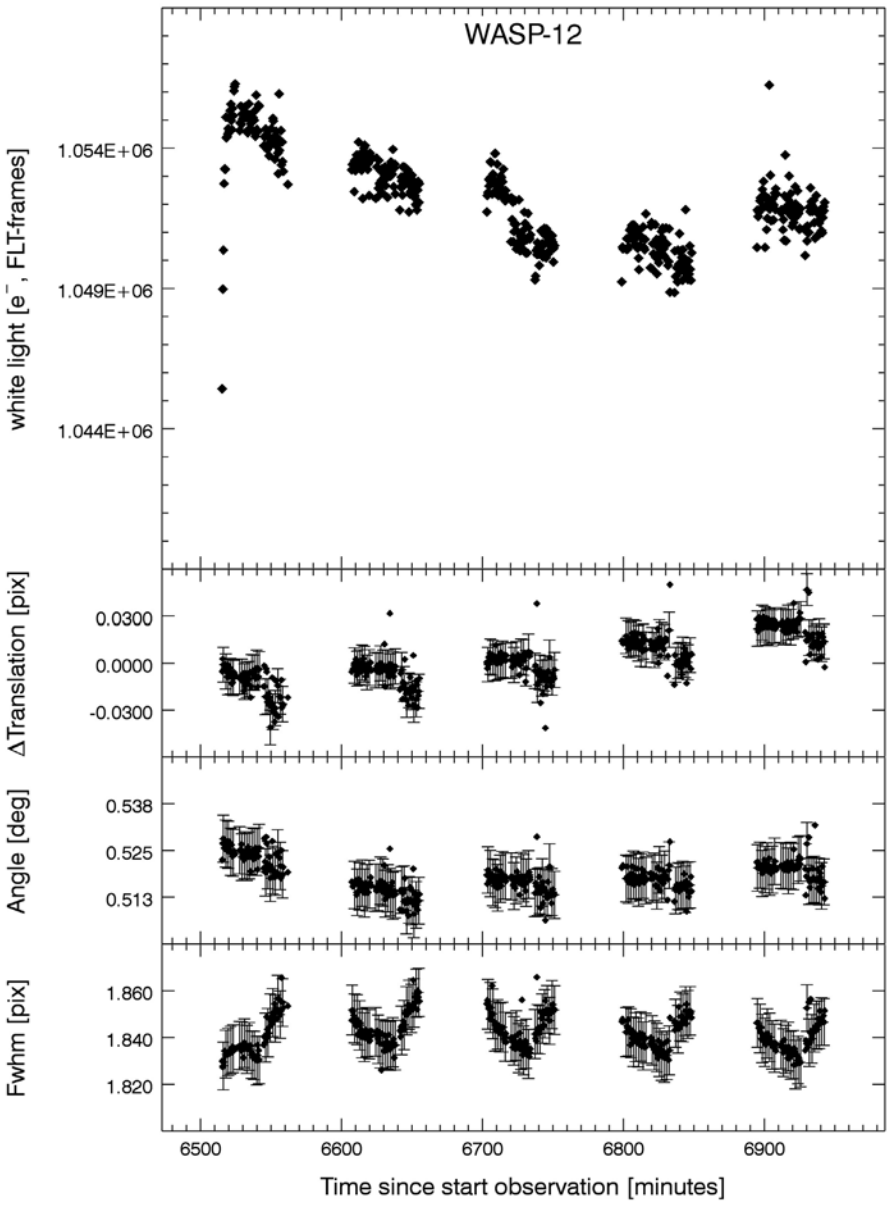

Figure 14.1-14.

2. Dayside Mapping

The planetary surface was divided into 47 pixels according to the movement of the main star's edge projected on the planet, as shown in Figure 7 in the main paper. Area of the j-th pixel, S_j, is given by

$$A_j = I_{c1,c2}(\tau_j) - I_{c1,c2}(\tau_{j-1})$$

$$I_{c1,c2}(\tau) = \theta_1(\tau) - \cos\theta_1(\tau)\sin\theta_1(\tau) + \theta_2(\tau) - \cos\theta_2(\tau)\sin\theta_2(\tau),$$

where τ specifies the distance from the center of the main star to the planetary center (for ingress $\tau<0$) as indicated in Figure 7 of the main paper, $\Sigma_{c1,c2}$ is the overlapped area of the main star and the planet, $\theta_1 = \angle paO$, $\theta_2 = \angle pOa$ where O is the center of the planet. Then, disk-averaged intensity $I(\tau)$ is expressed as

$$I(\tau_j) = \sum_{j=1,N_{pix}} W_{ij} m_j + \epsilon_i$$

$$W_{ij} = \begin{cases} 0 & for\ \tau_i \geq \tau_j \\ I_{c1,c2}(\tau_j) - I_{c1,c2}(\tau_{j-1}) & for\ \tau_i \leq \tau_j \\ I_{c1,c2}(\tau_i) - I_{c1,c2}(\tau_{j-1}) & else. \end{cases}$$

We solve the linear inverse problem using the Tikhonov regularization with the L-curve criterion (e.g. Hansen 2010, see also Kawahara and Fujii 2011, Fujii and Kawahara 2012). The misfit function of the Tikhonov regularization is expressed as

$$Q_\lambda = \sum_{i=1}^{N} \frac{|d(t_i) - \sum_j W_{ij} m_j|^2}{\sigma_i^2} + \lambda^2 \sum_j |m_j - m_{prior}|^2 \ ,$$

where $d(t_i)$ is the planetary flux and its error σ_i is estimated from variance of two sets during out-of-transit, which has the same HST orbital phase (see Figure 2-1) . We extracted one outlier seen in OT II, indicated by a red arrow (see Figure 2-1). We adopt the disk average brightness as prior: m_{prior} = (out-of-transit average – in-transit average)/disk area. The regularization parameter λ is chosen by the L-curve criterion (Hansen 2010), which balances between observational noise and spatial resolution of the planetary surface. The L-curve of the ingress mapping exhibits clear curvature maximum as shown in Figure 2-2. We used the corresponding value for the spatial resolution λ.

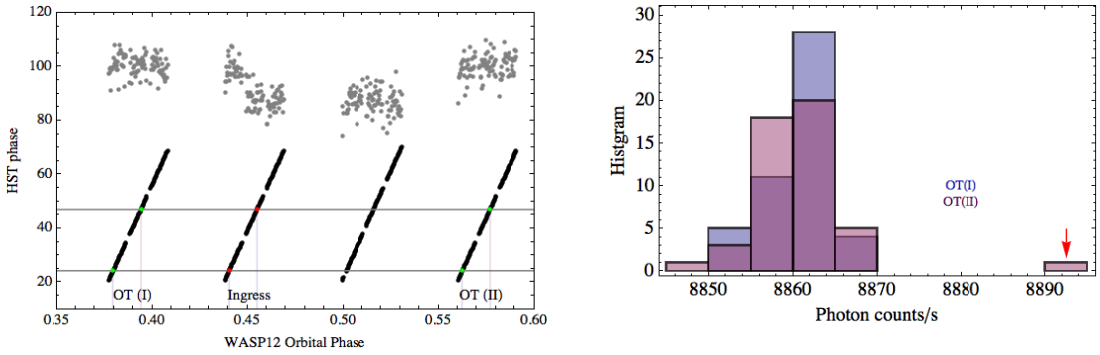

Figure 2-1: *(Left) HST orbital phase and the analysis regions between two green points for the systematic analysis during the out-of-transit (OT I and II) measurements. (Right) Histogram of OT I and OT II region for the 1.13-1.64 micron band. Red arrow indicates outlier we exclude for computing the variance.*

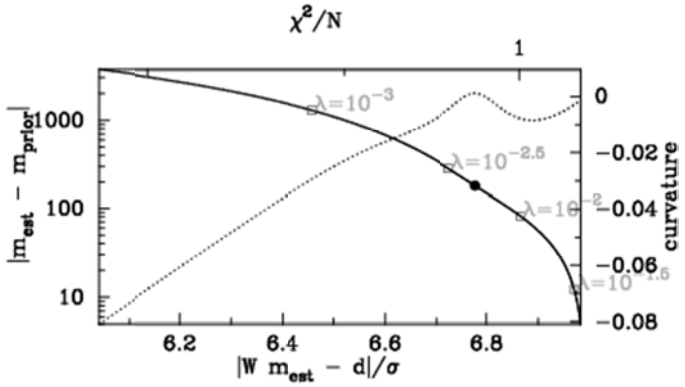

Figure 2-2: *The L-curve (solid) and its curvature (dashed) for the mapping. We adopt* λ *at the point of the curvature maximum of the curve of the prediction error (x-axis) versus the model variance (y-axis) as indicated by the black point.*

The sensitivity of the estimated surface brightness to observed data against prior is different for each slice. The sensitivity can be quantified by the integrated sensitivity vector ***S*** (Zhdanov 2002), which is defined as

$$S_j = \sqrt{\sum_{i=1}^{N} W_{ij}^2}$$

Figure 2-3 shows the slice-dependent sensitivity. Slices on the right-hand side are less sensitive to the data because they contribute only to the beginning part of ingress data. The insensitivity to the left-hand side is due to small area. The parts with less sensitivity are naturally suppressed to the prior by the second term of the misfit function Q_λ.

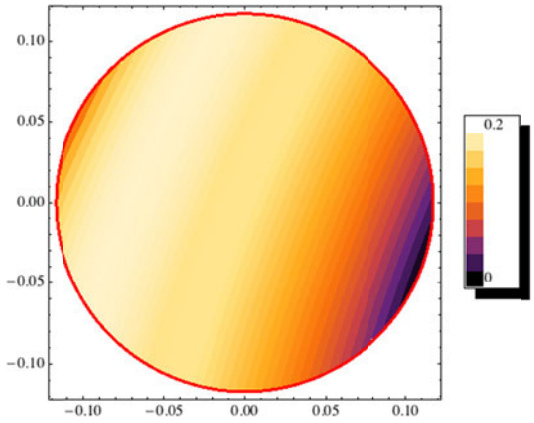

Figure 2-3: *The integrated sensitivity S. Brighter slices are more sensitive to data and dimmer ones tend to be suppressed to the prior.*

To test the systematic effect, we create the mock curves of the uniform disk with errors. Since the HST orbital phase may affect the pattern of the errors, we used the error series based on the out-of-transit observation at the same HST phase (see Figure 2.1). Figure 2-4 shows the mapping results from the mock light curves with the uniform disk model. To adopt the same effective resolution of the map, we used the same value of λ as used for the observed ingress data. Since the uniform disk + noise results in deviation from the noiseless light curve with uniform disk at marginally smaller level than the observed data, the inhomogeneity reconstructed from the observed ingress data is marginal.

We also computed the reduced chi-square of the observed ingress data with the uniform model and obtained 1.06. Hence, while the best-fit model shows an indication of non-uniform dayside emission localized in a central arc, the uniform disk model is not rejected yet.

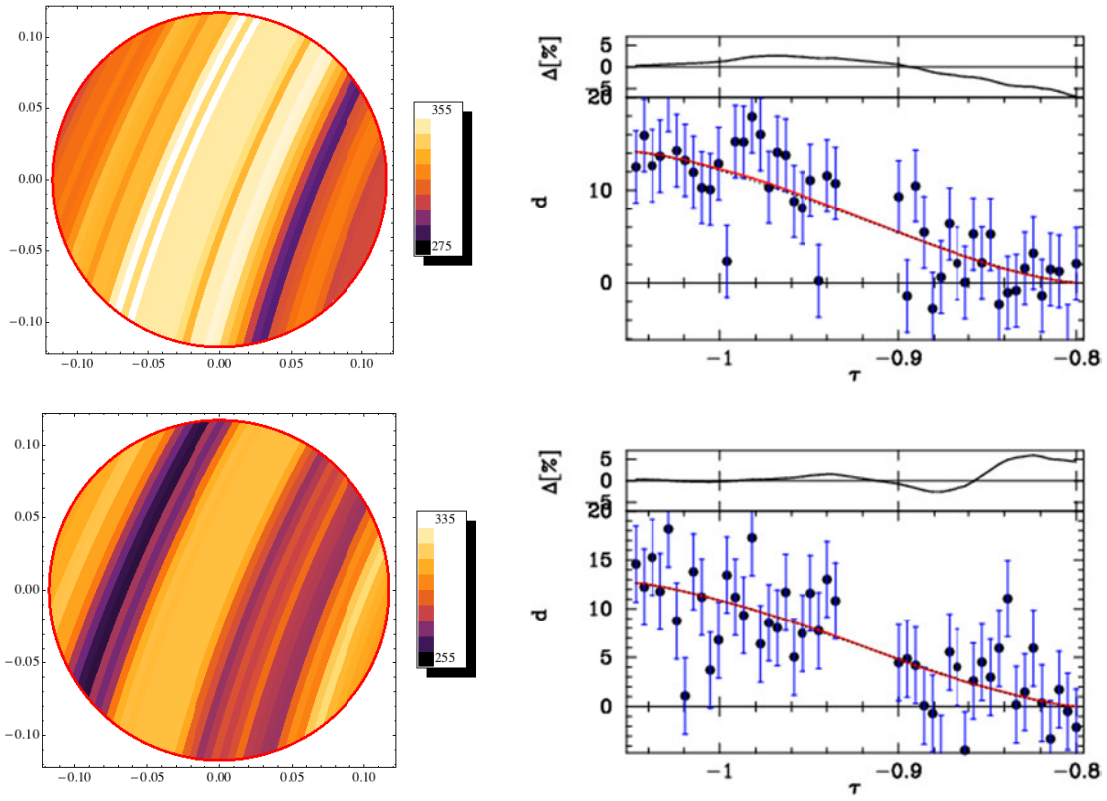

Figure 2-4: *Mapping results (left) and predicted curve (right) for the uniform disk + systematics computed from OT I (top) and OT II (bottom).*

References

Beletic et al. 2008, Teledyne Imaging Sensors: infrared imaging technologies for astronomy and civil space, proc. SPIE, Vol. 7021, 70210.

Fixsen et al. 2000, Cosmic-Ray Rejection and Readout Efficiency for Large-Area Arrays, PASP, 112, 1350.

Hansen, P. C. 2010, Discrete Inverse Problems: Insight and Algorithms (the Society for Industrial and Applied Mathematics).

Offenberg et al. 2001, Validation of Up-the-Ramp Sampling with Cosmic-Ray Rejection on Infrared Detectors, PASP, 113, 240.